2021

Impact Dynamics of Surfactant-Laden Droplets on Non-Wettable Coatings

Amir Esmaeili
Virginia Commonwealth University

Impact Dynamics of Surfactant-Laden Droplets on Non-Wettable Coatings

A dissertation submitted in partial fulfillment of the requirements for the degree of Doctor of Philosophy at Virginia Commonwealth University

By

Amir Reza Esmaeili

M.Sc. Mechanical Engineering, University of Tehran, Tehran, Iran, 2018

Director: Reza Mohammadi, Ph.D.

Assistant Professor, Department of Mechanical and Nuclear Engineering

Virginia Commonwealth University

Richmond, Virginia

August 2021

Dedication

I would like to dedicate my dissertation work to my family. A special thanks to my loving parents, Abbas and Maryam, who have always been my number one fan. Also, my dear siblings, Ali and Soheila, who have never left my side and are very special. I could not have come this far without their unconditional support.

Acknowledgment

I would like to thank Dr. Reza Mohammadi, my advisor, for his continuous support, valuable guidance and encouragement throughout my graduate program at Virginia Commonwealth University. Besides being an excellent mentor, he has always been a good friend and helped me adapt to my role as a graduate research assistant in his research group. I would not have been able to finish this work without his support and unfailing faith in me.

I would like to extend my gratitude to the other members of my Ph.D. committee, Drs. Carlos Castano, Dmitry Pestov, Christina Tang and Hong Zhao, for their insightful questions, valuable suggestions and comments, which have helped strengthen my work.

I am thankful to my friends, Roja, Ali, Mohammad, Ehsan, Sina, Tao and my labmates, Noushin and Ashton for supporting me in the last three years and making my life memorable in the USA.

I would like to express my gratitude to my family for their endless support. I am thankful to my parents for always supporting me and encouraging me to follow my dreams and pursue my goals. Without their unconditional support, I could not come this far and get my Ph.D. here at Virginia Commonwealth University.

Finally, I would like to express my appreciation to Virginia Commonwealth University for supporting my graduate education.

Table of Contents

List of Figures

time was 6 h and the solid coating was treated with ethanol. Blue and red arrows indicate the elongated patterns and nano spherical particles, respectively.

Figure 2.4. SEM images of AKD coating prepared from melts isothermally heated for 3 min at different temperatures, followed by post-solidification ethanol treatment: (a) 40, (b) 50, (c) 60, (d) 70 and (e) 80°C.

Figure 2.5. SEM images of AKD samples prepared from heated melt at 70°C with different isotherm times and post-solidification modification: (a) isotherm time was 3 min and the sample cured over 4 days without any post-modifications, (b) a similarly-prepared sample of part (a) was treated with ethanol prior to curing, (c) isotherm time was 6 h and then the solid coating was treated with ethanol and (d) the same sample in part (c) left at room temperature for 4 days.

Figure 2.6. Topography of AKD coating prepared from melts isothermally heated for 3 min at different temperatures with different post-synthesis modifications: (a) the melt was isothermally heated at 40°C without any post-solidification treatments, (b) the melt was isothermally heated at 40°C min and the solid coating was treated with ethanol, (c) the melt was isothermally heated at 70°C without any post-solidification treatments, (d) the melt was isothermally heated at 70°C min and the solid coating was treated with ethanol.

Figure 2.7. Advancing and receding contact angles of ethanol-treated solidified AKD from: (a) isothermally heated melt at 40 to 80°C for 3 min and 6 h and (b) isothermally heated melt at 70°C for 3 min, 3 h, 6 h and 9 h.

Figure 2.8. SEM images of an AKD coating obtained from an isothermally heated melt at 70°C for 3 h on a piece of standard paper: (a) as-solidified and (b) the solid coating was treated with

Figure 4.5. Retraction ratio of water droplets as well as the droplets of SDS, CTAB and MEGA-10 solutions of various concentrations at –10, –20 and –30 °C. The impact velocity was 1.08 m/s.

Figure 4.6. Relaxing diameter of water droplets as well as the droplets of SDS, CTAB and MEGA-10 solutions of various concentrations at –10, –20 and –30 °C. The impact velocity was 1.08 m/s.

Figure 4.7. Freezing time of water droplets as well as the droplets of SDS, CTAB and MEGA-10 solutions. T_s represents the temperature of the substrates which is equal to –20 and –30 °C.

Figure 4.8. Freezing stages of water droplets as well as the droplets of SDS, CTAB and MEGA-10 solutions with concentrations of 4, 0.45 and 2 mM, respectively, having an equilibrium surface tension of 44.73±0.51 mN/m. The temperature of the substrate is equal to –20 °C. The scale bar is the same for all the frames.

Figure 5.1. X-ray diffraction (XRD) patterns of co-sputtered Ni-W films on silicon wafer substrates with respect to the W at.% of the samples: (a) Pure Ni, (b-e) Ni-W films with 20, 39, 55 and 79 at.% W, respectively and (f) Pure W. It is to be noted that "NC" in (c) and (d) refers to nanocrystalline phase.

Figure 5.2. Scanning electron microscopy (SEM) images of the co-sputtered Ni-W thin films with respect to their W content: (a) pure Ni, (b-e) Ni-W coating with 20, 39, 55 and 79 at.% W, respectively and (f) pure W. The red and blue arrows in b and e, point to the two types of surface features observed in these samples. Insets: the cross-sectional SEM images of each sample. The full-size versions of the insets are given in Figure A6 of Appendix A.

Figure 5.3. Atomic force microscopy (AFM) of the co-sputtered Ni-W thin films with respect to their elemental composition: (a) pure Ni, (b) Ni-20 at.% W, (c) Ni-39 at.% W, (d) Ni-55 at.% W,

(e) Ni-79 at.% W and (f) pure W. The red and blue arrows in b point to the two types of surface features observed in the sample.

Figure 5.4. Comparison of Vickers microindentation hardness of the co-sputtered Ni-W thin films of the present work with relevant studies of the literature with respect to the W content [178,179]. The force load and dwell time of indentation in our hardness measurements were 0.098 N and 10 s, respectively. Linear regression was fitted to each series of data points to quantitatively indicate the dependency of the hardness on the W addition. c is the W content in the films in atomic percent.

Figure 5.5. Static contact of a water droplet having a volume of 5 µl on the untreated Ni-79 at.% W thin film (right) and treated sample with 5 wt.% AKD solution in n-hexane (left).

Figure A1. SEM images of AKD coatings prepared from a melt isothermally held at different times at 40°C and undergone different post-synthesis modifications: (a) isotherm time was 3 min without any post-solidification treatments, (b) isotherm time was 3 h without any post-solidification treatments, (c) isotherm time was 6 h without any post-solidification treatments, (d) isotherm time was 3 min and the solid coating was treated with ethanol, (e) isotherm time was 3 h and the solid coating was treated with ethanol and (f) isotherm time was 6 h and the solid coating was treated with ethanol. Red arrows show particles with irregular random morphologies on the solid coatings with no post treatment.

Figure A2. FT-IR spectra of solidified AKD from the isothermally heated melt at 70°C for 3min (a) as-solidified, (b) solid coating was treated with ethanol and (c) the as-solidified sample cured over time with no extra modifications.

Figure A3. XPS scan surveys of AKD coating from the isothermally heated melt at 70°C for 3 min (a) as-solidified, (b) solid coating was treated with ethanol and (c) the as-solidified sample cured over time with no extra modifications.

Figure A4. Scanning electron microscopy (SEM) images of the impact substrate: (a) AKD, (b) PTFE and (c) Glass. All the substrates were coated with a thin layer (~2 nm) of platinum prior to imaging for better electrical conductivity.

Figure A5. Surface topography of the impact substrates obtained using laser scanning confocal microscopy: (a) AKD, (b) PTFE and (c) Glass.

Figure A6. Cross-sectional scanning electron microscopy (SEM) images of the co-sputtered Ni-W thin films with respect to their W content: (a) pure Ni, (b-e) Ni-W coating with 20, 39, 55 and 79 at.% W, respectively and (f) pure W.

List of Tables

Abstract

Impact Dynamics of Surfactant-Laden Droplets on Non-Wettable Coatings

By Amir Reza Esmaeili, M.S.

A dissertation submitted in partial fulfillment of the requirements for the degree of Doctor of Philosophy at Virginia Commonwealth University.

Virginia Commonwealth University, 2021

Director: Reza Mohammadi, Ph.D.

Assistant Professor, Department of Mechanical and Nuclear Engineering

Owing to their excellent water repellency, non-wettable (superhydrophobic) coatings have gained tremendous attention in the past couple of decades. Alkyl ketene dimer (AKD), an inexpensive polymer frequently used in paper industry as a sizing agent, has shown potentials to become superhydrophobic. The formation of a porous structure after curing the solidified AKD for an extra-long time (4–6 days) results in superhydrophobicity, i.e., a static contact angle with water of >150° and a roll-off angle of <10°. In this work, a facile and low-cost method was used to turn the surface of AKD superhydrophobic in a very short period of time by briefly treating the coatings, obtained from isothermally heated molten AKD at 40 °C for 3 min, with ethanol. The resulting superhydrophobicity is due to the formation of porous, entangled irregular micro/nano textures that create air cushions on the surface leading to droplet state transition from Wenzel to Cassie. As a proof of concept, the same material was applied to the co-sputtered nickel-tungsten thin films, commonly used in micro/nano-electro-mechanical systems, to improve their hydrophobicity. According to the results, at least 20% increase was observed in the dynamic contact angles of the treated substrates.

In addition, this work presents a detailed high-speed imaging analysis of the influence of the molecular weight, concentration and ionic nature of surfactants on droplet impact of such solutions on hydrophilic, hydrophobic and superhydrophobic substrates. Among all these surfaces, the concentration and ionic nature of the solutions were found to be more dominant parameters in determining the energy dissipation in the retraction phase of the droplet impact on the superhydrophobic (AKD) surfaces at room temperature. As the concentration decreases or when positive charges are present in the solution, it is more likely to observe a similar retraction dynamic to pure water when the droplet hits the superhydrophobic AKD having negatively charged surface sites.

Finally, the impact dynamics and freezing behavior of these solutions were studied at very low temperatures of –10 to –30 °C. The results show that the dynamic behavior of the solutions is also a function of their temperature-dependent viscosity. The surfactant-laden droplets generally demonstrated an accelerated freezing compared to pure water. This might be due to the fact that the presence of surfactants can promote heterogeneous ice nucleation both from within the liquid as well as a larger solid-liquid interfacial area, resulted from filling the air pockets of the surface by surfactants, leading to enhanced heat transfer. The behavior of the cationic surfactant at certain concentrations was, however, an exception leading to a freezing delay, for which a mechanism will be proposed.

Chapter 1. Introduction

1.1 Background Information

1.1.1 Contact Angle of Droplets

The contact angle that a sessile droplet forms with a solid surface is determined by the equilibrium of the adhesive and cohesive forces. This parameter, which can have a value between 0 to 180°, is a function of the interfacial tensions of the droplet as well as the surface energy of the substrate. Thomas Young was one of the pioneers studying the contact angle of droplets on flat substrates [1]. The results of his study led to the introduction of an equation correlating the surface energy of the solid surface (γ_{SG}), the energy of solid-liquid interface (γ_{SL}) and the surface tension of the liquid droplet (γ_{LG}) with the contact angle (θ):

$$\gamma_{SG} - \gamma_{SL} - \gamma_{LG}\, cos(\theta) = 0 \tag{1.1}$$

In Eq. (1.1), the solid surface is assumed to be ideal (i.e., rigid, flat and chemically homogeneous surfaces) and surface roughness has not been considered. However, most practical surfaces are relatively rough with unique textures. In some cases, these textures result in the trap of air pockets on the surface, altering the solid-liquid interfacial area. If the droplet penetrates these air pockets, the solid-liquid interfacial area increases; consequently, the contact angle changes. To better understand the relationship between the intrinsic contact angle, which is the contact angle of a droplet on an ideal surface, the apparent contact angle and the surface roughness, Wenzel proposed Eq. (1.2) for uniform surfaces [2]:

$$cos\theta^* = r\, cos\theta \tag{1.2}$$

In Eq. (1.2), r is the ratio of the actual surface and apparent surface and θ^* and θ are the apparent and intrinsic contact angles, respectively. The influence of surface roughness on the contact angle was further investigated by Cassie and Baxter in 1944 [3]. Their study focused on the influence of the porous medium on the contact angle, where the droplet does not penetrate the micro-textures on the rough and chemically homogeneous surfaces; as a result, the preserved air pockets on the surface can increase the contact angle based on Eq. (1.3):

$$cos\theta^* = -1 + \varphi_s(1 + cos\theta) \tag{1.3}$$

where φ_s is the fraction of solid substrate, which is in contact with the liquid droplet. According to Eq. (1.3), as the solid-liquid interfacial area decreases and φ_s approaches 0, the contact angle increases up to 180°. Figure 1.1 shows different wetting states of a droplet on a solid substrate.

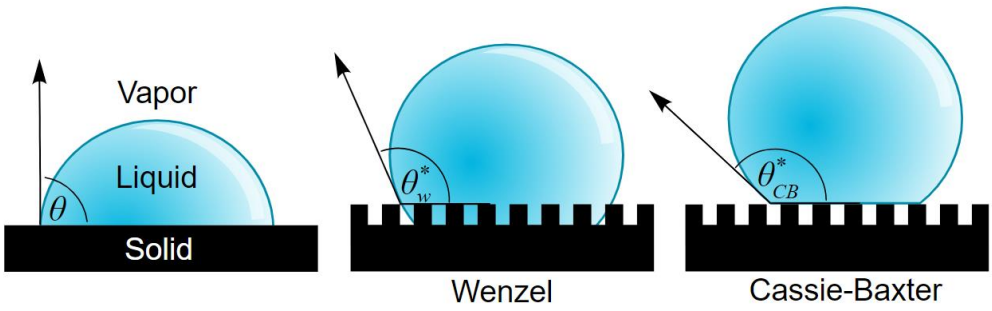

Figure 1.1. Different wetting states of a droplet on a solid substrate.

Additionally, Mettu *et al.* studied the influences of surface nonidealities on the contact angles more in-depth [4]. Generally, when the surface is not smooth or homogeneous, by adding some liquid to a sessile droplet, while the three-phase (vapor-liquid-solid) contact line is initially pinned, the contact angle increases to a specific point, which is called advancing contact angle. Beyond this point, the addition of more liquid results in the free movement of the three-phase contact line. The

opposite of this behavior can be seen by removing some liquid from the droplet. In this case, the contact angle decreases to the receding angle. The difference between the advancing and receding contact angles is called hysteresis. Mettu *et al.* showed that the droplet remains in a metastable state when the contact angle deviates from its equilibrium value. They subjected the substrate to white noise to investigate the dynamics of relaxation of the droplets [4].

1.1.2 Wetting Properties of Coatings

Two parameters that significantly affect the wetting properties of coatings are their surface energy and morphology [5]. There are three main types of coatings in terms of their wetting properties. The first type is hydrophilic or water-loving coatings, which have a water contact angle of <90°. In hydrophilic coatings, as the droplet is placed on the surface, it spreads, the wetting area increases and the contact angle drops to lower than 90° in a very short time. Roll-off angle is the minimum tilting angle to make the droplet roll down the substrate. Due to the strong adhesion between the droplet and hydrophilic substrates, this type of coatings has a large roll-off angle. In some cases, even by making the substrate upside down, the droplet does not detach from the coating. The second type of coatings having a water contact angle of 90 to 120° is called hydrophobic. Hydrophobic coatings have lower surface energy, surface adhesion and roll-off angle compared to the previous type of coatings. It is well documented that flat and smooth hydrophobic surfaces having low energy (e.g., nonstick cookware coated with Teflon) can have a contact angle of up to 120° [6]. Consequently, for further enhancement of the contact angle, a rough structure must be developed on the substrate to trap the air beneath the droplet and reduce the solid-liquid interfacial area. Surfaces having a water contact angle of >150°, a roll-off angle of <10° and low surface energy are known as superhydrophobic or non-wettable substrates [7,8]. These coatings are generally made of low energy materials (e.g., polymers) with adequate surface roughness. As it is

clearly shown in Figure 1.2, the sessile water droplet has formed an almost perfect sphere on the superhydrophobic coating with a small contact area.

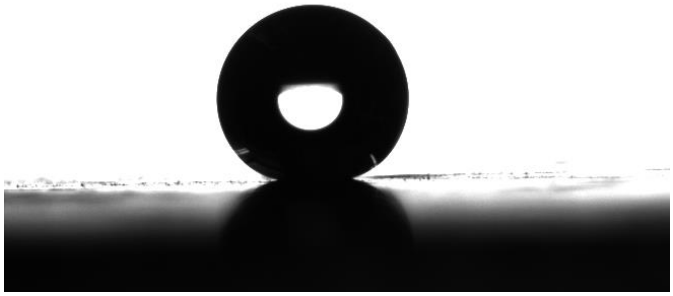

Figure 1.2. A water droplet on a superhydrophobic surface having a contact angle of >150°.

Due to their unique properties, superhydrophobic coatings are very popular in many industrial applications such as self-cleaning [9–12], anti-corrosion [13,14], anti-icing [15,16] and drag reduction [17]. Some of their industrial applications are in powerlines [18], wind turbines [19], aircrafts [20] and heat exchangers [21]. These surfaces can be fabricated through several methods, such as wax solidification, lithography [22], chemical vapor deposition [23], sol-gel processes [24] and electrospinning [25–30].

1.1.3 Impact Dynamics of Droplets

The shape evolution of a droplet impinging on a substrate is governed by its kinetic and capillary energies. The impact dynamics of a droplet is divided into two stages. The first stage is the spreading phase, starting as the droplet contacts the surface (Figure 1.3a). During the spreading phase, according to the energy conservation, a portion of the initial kinetic and capillary energies of the droplet just before the impact (state 1) transforms into the capillary energy at the maximum diameter. The rest of the initial energies is lost due to the viscous dissipation. The viscosity of the

droplet and the time required to reach the maximum diameter are two main parameters determining the energy loss in the spreading phase. This phase continues to the point that the diameter of the droplet reaches its maximum value and the kinetic energy of the droplet becomes zero (Figure 1.3e).

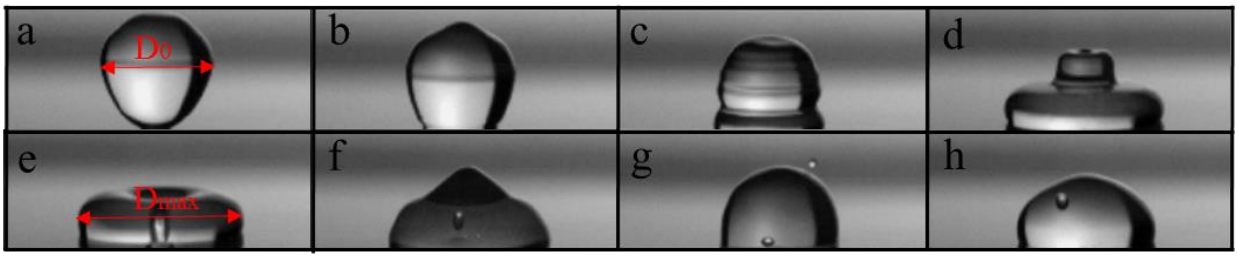

Figure 1.3. Snapshots of the water droplet impact on a superhydrophobic substrate. The spreading phase starts from (a) where the droplet touches the surface and continues to (e) where it has reached its maximum diameter. (f-h) Show the retraction phase of water droplets.

The second stage of the impact dynamics is called the retraction phase. In this phase, due to the stored capillary energy, the droplet minimizes the wetting area. Various outcomes are expected from the impingement of a droplet on a surface: (1) complete rebound, where the kinetic energy of the droplet is sufficient for overcoming the energy dissipated in this phenomenon, (2) partial rebound, where the droplet gets pinned on the surface and several secondary droplets eject (3) deposition, where the droplet experiences some vertical oscillation on the substrate (Figure 1.3f-h) and (4) splashing. The impact outcome is a function of the wetting properties of the substrate as well as the Weber number (*We*) of the droplet. Weber number is a function of the density (ρ), impact velocity (V), initial diameter (D_0) and surface tension (γ) of the impinging droplet and it is defined as the ratio of the inertial forces to surface tension forces:

$$We = \rho V^2 D_0/\gamma \quad (1.4)$$

According to the previous studies, it has been shown that the dynamic behavior of the impinging droplets is similar to a single-degree-of-freedom oscillating model (a mass-spring-damper model) and it can be described via the spring constant and damping coefficient [31–33].

1.1.4 Surfactants Solutions

In many industrial applications, the impinging droplets on the superhydrophobic coatings include various additives. Surfactants are one of the most common additives used in lubricants and cleaning agents in numerous applications. When surfactants are dissolved in pure water, their molecules diffuse toward the interfacial areas and bond with water molecules. Due to the weaker interaction between the molecules of water and surfactants compared to water molecules (hydrogen bonds), the surface tension of the solution decreases. It is worth mentioning that the equilibrium surface tension of the solutions, which is the equilibrium state between the bulk concentration and surface concentration of the droplet, is a function of the concentration and diffusion rate of the surfactants molecules. This parameter is also time-dependent, meaning that the time required for each solution to reach its equilibrium value is different. This phenomenon leads to remarkable changes in the dynamic behavior of surfactants solutions impacting superhydrophobic substrates during the spreading and retraction phases. According to the previous studies, the surface tension of the solutions decreases by an increase in concentration. However, there is a critical point for the concentration, where a bilayer of surfactants molecules is formed on the interfacial areas of the droplet. At this point, which is called critical micelle concentration (CMC), the surface tension of the solution does not change with any further increase in the concentration.

The chemical structure of the surfactants includes a polar head, which is hydrophilic and has high interaction with water and a non-polar tail, which is hydrophobic. They are categorized into three groups of anionic, cationic and non-ionic surfactants based on their polar head. Cationic, anionic and non-ionic surfactants carry positive, negative and neutral charges, respectively. Some of the common applications of surfactants are in cleaning the photovoltaic panels [34,35] and improving the thermal performance of wickless heat pipe solar collectors [36].

1.1.5 Freezing of Droplets

The freezing rate of a sessile droplet on a substrate is governed by the heat conduction through the substrate as well as the heat convection of the droplet with the ambient air [37,38]. The heat conduction rate through the substrate is a function of the heat conduction coefficient (k), interfacial area (A) and temperature difference between the solid-liquid phases (ΔT) and it is given in Eq. (1.5):

$$dQ/dt = -kA\Delta T \tag{1.5}$$

There are two main stages for the freezing of a sessile droplet. The first stage starts with rapid kinetic crystal growth and it is identified by a change in transparency of the droplet. This stage typically happens in less than 50 milliseconds by starting from one point and progressing throughout the whole droplet. The second stage begins when the droplet has become fully opaque. During this stage, the temperature of the droplet remains at the equilibrium temperature, which is 0 °C. Then, an ice front is formed in the droplet. The starting point of this ice front depends on the freezing mechanism of the droplet. Generally, there are two different freezing types: (1) homogeneous and (2) heterogeneous freezing. While in the former one, the supercooled droplet freezes with no assistance, in the latter mechanism, the presence of particles boosts the freezing by acting as ice nuclei. In heterogeneous freezing, the ice front usually forms on the solid-liquid

interface and vertically progresses toward the tip of the droplet. This stage happens isothermally and it is a function of the heat transfer through conduction and convection among three phases [37,38]. It is worth mentioning that in heterogeneous freezing, the presence of these particles enables the freezing process to happen at higher temperatures.

1.2 Overall Objectives

The first objective of this dissertation is using a facile method to fabricate low-cost superhydrophobic coatings. To fabricate these coatings, alkyl ketene dimer (AKD), which is commonly used in paper industry to improve the non-wettability of standard papers, is used as an inexpensive polymer. If the molten AKD solidifies at room temperature, a relatively smooth structure is formed on the substrate having a water contact angle of approximately 90°. After keeping the substrate in a desiccator at room temperature for 4 days, the surface morphology transforms to a porous/rough structure resulting in an increase in the water contact angle up to 174° [39,40]. Several studies have focused on methods to reduce the long curing time of AKD. The introduced methods usually require toxic solvents, expensive instruments and complex methods. However, the introduced method in this work is a straightforward method having advantages of low synthesis time (~3 min), simple solvent for etching (ethanol) and basic instruments. More details of this objective are given in Chapter 2.

Predicting and controlling the dynamic behavior of droplets have always been a challenging issue in numerous industrial applications, including spray cooling [41], inkjet printing [42], aerosol drug delivery [43,44], surface cleaning [45] and agrochemical sprays [46]. In the majority of these applications, the presence of surfactants or surface-active agents in the solutions results in significant changes in the liquid properties. The focus of the previous studies was on modeling the dynamic behavior of pure water. Only a few studies have characterized the impact dynamics of

surfactants solutions. The second objective of this dissertation, presented in Chapter 3, is to study the influence of physicochemical properties of surfactants solutions (i.e., concentration, molecular weight and ionic nature) on the impact dynamics and impact outcomes of these droplets in a wide range of Weber numbers. Additionally, three impact substrates with different wetting properties, ranging from hydrophilic to superhydrophobic coatings, have been used to comprehensively study the influence of impact substrates on these phenomena.

In the last decade, superhydrophobic coatings, due to their excellent anti-icing properties, have gained tremendous attention in subzero applications, which surfaces are essential to avoid ice formation. Since surfactants solutions can influence the liquid properties as well as the surface chemistry, it is indispensable to understand their dynamic behavior at low temperatures. Chapter 4 presents a detailed investigation on the dynamics and freezing behavior of surfactants solutions at subzero temperatures of –10 to –30 °C as the third objective of this dissertation.

Ultimately, the application of AKD coatings in improving the non-wettability of thin films is investigated in Chapter 5. In the last few years, nickel-tungsten thin films have gained much attention due to their novel mechanical [47,48], tribological [49], thermal [50] and anti-corrosion properties [51]. Additionally, they have been used in several high-tech applications, including but not limited to micro-electro-mechanical systems. First, the influence of tungsten content on the mechanical properties and microstructure of the co-sputtered nickel-tungsten alloy thin films has been investigated in the first part of Chapter 5. Then, the molten AKD has been applied to the fabricated thin films to increase the contact angle of the substrates, the results of which are presented in the second part of Chapter 5.

In the last part, Chapter 6, the concluding remarks and future directions of this dissertation are presented.

Chapter 2. A Facile, Fast and Low-Cost Method for Fabrication of Micro/Nano-Textured Superhydrophobic Surfaces

2.1 Introduction

Superhydrophobicity is the characteristic of surfaces that can demonstrate a static water contact angle greater than 150° and a roll-off angle of less than 10° [52]. Such surfaces have recently attracted a great deal of attention due to their numerous applications in self-cleaning [9–11], anti-corrosion [13,14,53], anti-icing [15,54,55] and drag reduction [17,56]. The principle of this technology is based on producing micro/nano structures on a surface of low energy [5,57].

To fabricate these surfaces, several methods including lithography [22], plasma treatment [58], colloidal self-assembly [59], wax solidification [39], wet chemical reaction [60,61][19,20] and electrospinning [25,26,62] have been introduced. To enhance the superhydrophobicity of materials that are weak in mechanical properties and chemical stability (e.g., cellulose-based paper), special treatments with chemicals such as fluorinated SiO_2 nanoparticles [63–65] are needed. To avoid the use of fluorochemicals, which are detrimental to human health and the environment, researchers have focused on fabrication of a superhydrophobic layer on the paper through building micro/nano structures on the substrate [66].

Alkyl ketene dimer (AKD), a widely used sizing agent in the paper industry, is an inexpensive and low-surface energy wax capable of forming a non-wettable layer on the substrate [67–72]. By applying the low cost and simple method of melting-solidification to this material [73–75], a relatively fine structure is spontaneously formed on the surface and fully develop to a porous/rough morphology after 4 days at room temperature, leading to an increased static contact angle from 90° to 174° [39,40].

Several studies have focused on methods to reduce the long curing time of AKD. For example, supercritical carbon dioxide ($scCO_2$) has been commonly used as the carrier solvent to produce coatings of AKD nanoparticles on the paper surface [76–80]. The main problem of this method is the energy cost for compression of CO_2 to its supercritical pressure [81,82]. In another approach, Fang *et al.* [83] reported a metastable to stable phase transformation by heat treatment of solidified AKD, resulting in spontaneous formation of fractal structures and sub-micrometer particles on its surface. Based on their results, when the heat treatment temperature of AKD increases from 40 to 50°C, its curing time decreases from 6 days to 1 h. In addition, Shen *et al.* [84] monitored the migration of AKD on glass as well as macroscopic sizing effect at temperatures well above its melting point.

We have previously conducted some studies on the modification of surfaces by treating them with organic solvents to improve their hydrophobicity [8,55,85–87]. As such, the goal of the present work is to develop a micro/nano structure on the surface of AKD to obtain a superhydrophobic surface by using ethanol and heat treatment. This method is a step forward for advancing an important field in colloid science known as "microphase separation" [88], in which a highly porous structure is formed in the presence of an inert solvent. This approach usually requires expensive polymers and highly toxic solvents [89], co-polymerization [88–90], etching [91], or UV/microwave curing [89–92]. However, herein by using a very low-cost polymer and presenting a straightforward approach with several advantages including low temperature (40-70°C), short synthesis time (3 min) and simple solvent (ethanol), we have successfully achieved high dynamic contact angles (156.8-163.7°) and low hysteresis (1.1-1.9°). As a proof of concept, we apply our method to glass and paper, two commonly used substrates in industry and investigate their wetting. Additionally, this method has also been applied to the co-sputtered nickel-tungsten thin films,

commonly used in micro/nano-electro-mechanical systems, the results of which are presented in Chapter 5.

2.2 Experimental Procedure

2.2.1 Sample Preparation

Glass slides (25.4×25.4×1 mm, AmScope, USA) were cleaned in ethanol (99%, Sigma-Aldrich, USA) for 10 min using an ultrasonic cleaner (Thermo Fisher Scientific, USA) and then dried using compressed air at room temperature (~23°C). Equal portions (11 g) of AKD pellets (Solenis, USA) were each placed in a polymethylpentene beaker (Kartell, Italy) and separately heated on a hot-plate up to ~40 (melting point), 50, 60, 70 and 80°C. The molten AKD samples were each isothermally heated at these temperatures for different durations of 3 min, 3 h, 6 h and 9 h. Next, the glass slides were covered with molten AKD by dip-coating, i.e., submerging them in the molten AKD (obtained from each condition discussed above) for a few seconds and removing them immediately. Then, we left the coated samples in the air at room temperature for ~3 min to allow the AKD coating to solidify and form a thin layer (~20 µm) on the glass slides. Next, some of the coated glass samples were dipped in ethanol for 1 min and dried in air at room temperature for ~1 min.

2.2.2 Sample Characterization

To determine the functional groups of the samples, their Fourier transform-infrared spectroscopy (FT-IR) spectra were recorded using a Nicolet Nexus 670 FT-IR spectrometer (Thermo Fisher Scientific, USA) in the range of 400–4000 cm^{-1}. In order to identify the phases of the samples, their X-ray diffraction (XRD) patterns were collected with a PANalytical X'Pert Pro Diffractometer (Malvern, UK) with Ni-filtered $Cu_{K\alpha}$ radiation having a wavelength of 0.15418 nm.

The samples were scanned over a range of $5^{\circ}<2\theta<50^{\circ}$ with a scan rate of 2.2°/min. Scanning electron microscopy (SEM) images were taken using a Hitachi SU-70 scanning electron microscope (Hitachi, Japan). Since the samples were not conductive, they were coated with a very thin layer (~2 nm) of gold by sputtering (Artisan Scientific Corp., USA) prior to imaging. In addition, X-ray photoelectron spectroscopy (XPS) data were collected with an ESCALAB 250 X-ray photoelectron spectrometer (Thermo Fisher Scientific, USA) using a monochromated aluminum X-ray source with a step of 1 eV. Besides, using a Confocal laser scanning microscope (Zeiss LSM 710, Germany), the topography of the coatings was constructed, from the data of which the roughness values were extracted. In addition, in order to measure the mean diameter and fraction of pores on the surface of AKD coatings, the SEM images were analyzed with an image-processing software (ImageJ 1.52a).

2.2.3 Contact Angle Measurements

In the present study, advancing and receding contact angles were measured for 9 randomly-chosen spots on each sample with the liquid increase/decrease method. First, a 3 µl of de-ionized (DI) water (Resistivity = 18.2 MΩ.cm, from MiliQ, Milipore, USA) droplet was gently placed on the surface using a needle with a diameter of 0.1 mm. Next, another 3 µl DI water was pumped into the initial droplet at a constant rate of 0.002 ml/min for the advancing contact angle measurement. Then, 3 µl DI water at the same speed was removed from the existing droplet on the surface to measure the receding contact angle. Moreover, a drop shape analyzer (DSA25E, Krüss, Germany) was used to measure the contact angles [93,94].

2.3 Results and Discussion

Figure 2.1 illustrates the XRD patterns of AKD with different post-solidification treatments. The coating was prepared from a 70°C melt isothermally heated for 3 min. When the as-solidified AKD is left in air at room temperature for 4 days, the morphology and crystal structure of the sample change and the number of air pockets on the surface increases. As a result, the static contact angle of the sample with water increases up to 174° [40], leading to an excellent superhydrophobicity [6,39,95]. According to the study of Fang *et al.* on the formation mechanism of superhydrophobic AKD, the material transforms from a metastable to a stable phase during its curing process, which is typically characterized by X-ray reflections at 2θ=23.5 and 24.3°, respectively [83]. When AKD rapidly solidifies from its melt, the molecules on the surface of the samples are poorly arranged in the metastable phase. By heat treatment of the solid, as demonstrated by Fang *et al.* [83], AKD molecules obtain enough energy to spontaneously re-arrange themselves in a short period of time. From our XRD patterns, it is clear that the location of the peaks does not change by a long period of isothermal heating or ethanol treatment. However, the relative intensity of the peaks changes. Besides, metastable and stable peaks of our samples, labeled in Figure 2.1 with (**) and (*) respectively, have slightly shifted to higher diffraction angles in comparison with the study of Fang. *et al.* [83]. By comparing the XRD patterns of untreated (Figure 2.1a and 2.1c) and ethanol-treated (Figure 2.1b and 2.1d) samples, it is observed that by ethanol treatment, the intensity of the metastable phase has decreased while that of the stable phase has increased. From these results, it can be concluded that ethanol treatment plays the same role as the heat treatment in the curing process of AKD and increasing its degree of crystallization.

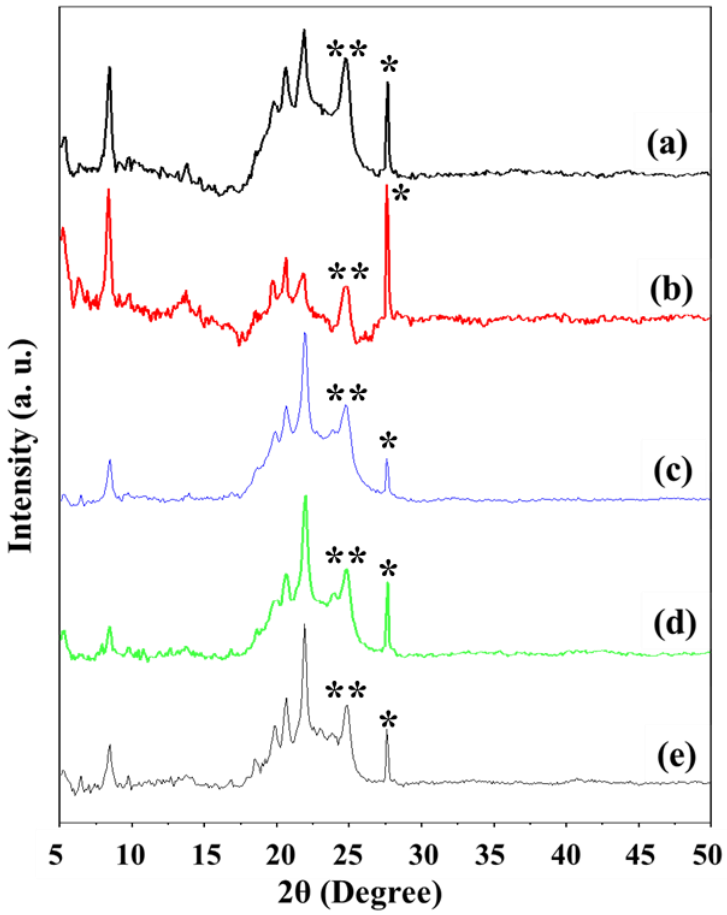

Figure 2.1. X-ray diffraction patterns of AKD prepared from a 70°C melt, isothermally heated for different durations and treated under various conditions after solidification: (a) isotherm time was 3 min without any post-treatments, (b) isotherm time was 3 min and then the solid coating was treated with ethanol, (c) isotherm time was 6 h without any post-treatments, (d) isotherm time was 6 h and then the solid coating was treated with ethanol and (e) molten AKD was isothermally heated for 3 min and cured over 4 days without any post-treatments. Metastable and stable peaks are labeled with (**) and (*), respectively.

Scanning electron microscopy was used to study the effect of molten AKD's temperature (40 - 80°C), the isothermal heating time of the melt at each temperature before dip coating and post-solidification ethanol treatment on the surface morphology of the samples. First, to study the

impact of ethanol treatment on the AKD surface, two samples were considered from the batch prepared from the isothermally heated melt of AKD at 40°C for only 3 min, one without and with ethanol treatment. According to the SEM image of untreated sample, shown in Figure 2.2a, the surface is very smooth and almost no outstanding textured structure has formed. Previous reports have also shown almost the same morphology for the similar reaction condition [60,83]. The smooth morphology favors hydrophobicity of the surface due to the lack of sufficient number of air pockets on the surface. Figure 2.2b, on the other hand, shows the SEM image of ethanol-treated sample containing a peculiar entangled micro/nano structure. Based on previous studies, the formation of micro/nano particles ranging from ~100 nm to ~10 μm on a substrate of low surface energy (e.g., polymers) can increase the contact angle [63–66,96]. By comparing the water droplets in the insets of Figures 2.2a and 2.2b, it is evident that ethanol treatment has drastically increased the contact angle. While the untreated sample has advancing and receding contact angle values of 92.9±3.0 and 78.4±4.7°, the ethanol-treated sample has non-wettable properties with advancing and receding contact angle values of 158.7±1.4 and 156.8±0.9°, respectively.

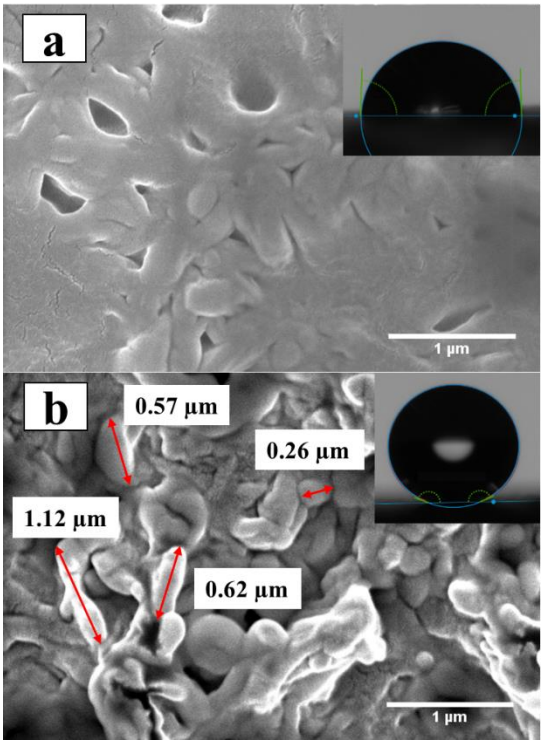

Figure 2.2. SEM images of AKD coatings prepared from a 40°C melt, isothermally heated for 3 min: (a) with no post-solidification modifications and (b) solid coating was treated with ethanol. Insets: water droplet on the samples.

Treatment of the molten AKD before dip coating is another critical factor that can have a remarkable impact on the formation of micro/nano structures on the surface of this polymer. It has been shown that isothermally heating the melt can be an alternative to the 4 days curing time of AKD [83]. Here, we study the surface morphology of the AKD coatings with respect to its melt isotherm time at a specific temperature, each followed by post-solidification ethanol treatment. First, the molten AKD was isothermally heated at 40 and 70°C for 3 min, 3 h and 6 h, separately. Then, the glass slides were coated with the molten AKD, following the procedure detailed in the Experimental section. Finally, the coated samples were treated with ethanol.

Figure A1 shows the morphology of AKD coatings from an isothermally heated melt at 40°C with

different modifications. All as-synthesized (without ethanol treatment) and ethanol-treated coatings prepared from pre-heated melt for 3 min, 3 h and 6 h are shown on the left side and right side of Figure A1, respectively. According to the results of untreated samples (Figure A1a, A1b and A1c), it is clear that increasing the isotherm time of the AKD melt at 40°C has not markedly changed the morphology of the samples. A large part of all these three samples consists of smooth regions. Interestingly, by treating the same samples with ethanol (Figure A1d, A1e and A1f), the surface morphology changes and those smooth regions turn into irregular entangled patterns potential for trapping air. In addition, there are some particles with irregular random morphologies on the surface of untreated samples (shown by red arrows) that have been removed by ethanol treatment, leading to a more homogeneous surface.

The SEM images of the solid coating from isothermally heated of AKD melt at 70°C are illustrated in Figure 2.3; untreated samples are shown on the left and ethanol-treated samples are shown on the right. As can be observed, while in all three untreated samples (Figure 2.3a, 2.3b and 2.3c), some areas are smooth, by treating them with ethanol (Figure 2.3d, 2.3e and 2.3f), the smooth areas have transformed to irregular entangled structures. After ethanol treatment, in some regions, the features look like more fused together and form wall-like patterns. Moreover, there are two types of features seen in the three treated samples; the first type includes nano spherical particles with a diameter of 0.36±0.08 μm and in the second type, there are some elongated patterns with a length of 1.07±0.30 μm (blue and red arrows, respectively, in Figure 2.3d, 2.3e and 2.3f). In addition, it is seen that there are some distinct features on the surface of untreated sample prepared from the isothermally heated melt for 3 min (Figure 2.3a) that disappear after increasing the heating time and treating the solid coating with ethanol (Figure 2.3d).

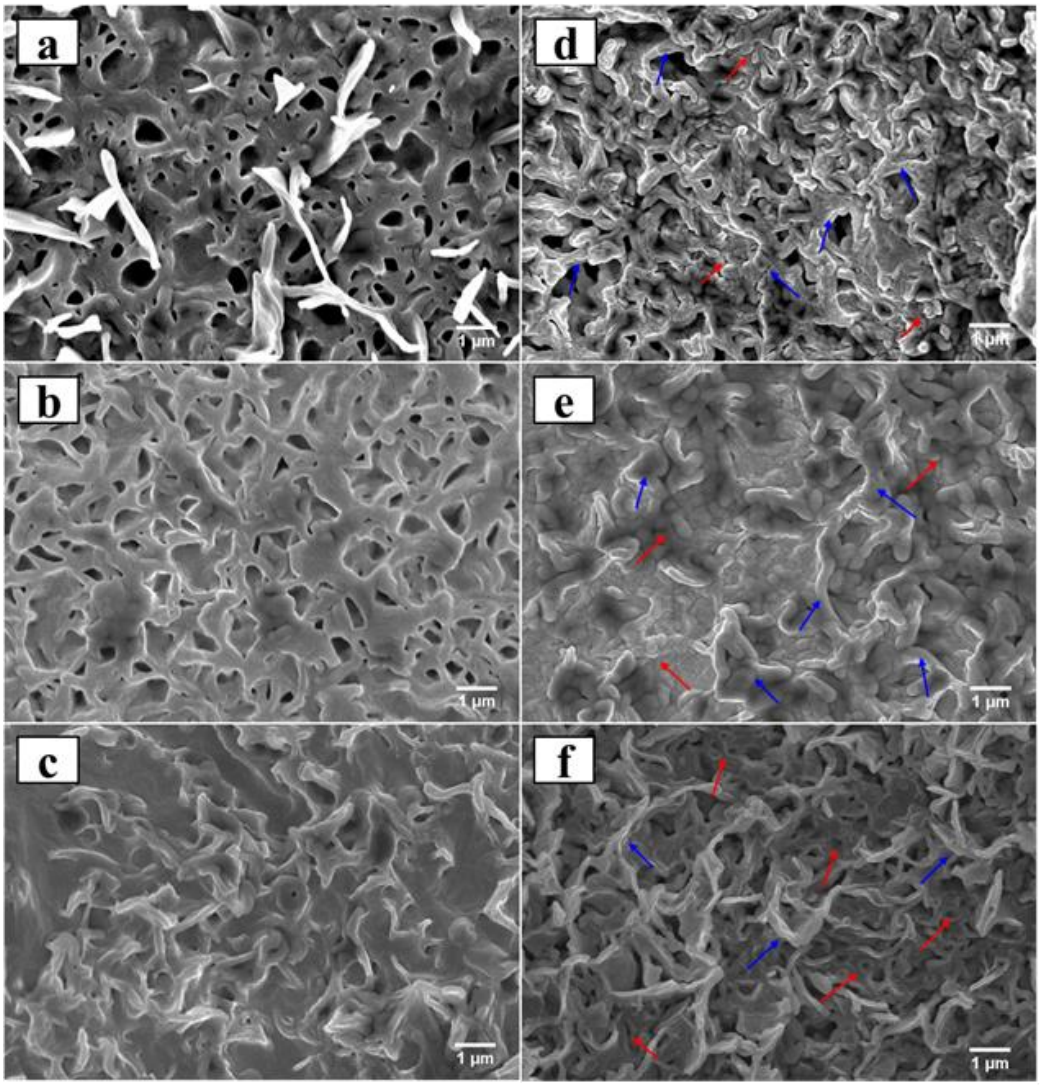

Figure 2.3. SEM images of AKD coatings prepared from a 70°C melt with different isotherm times and post-solidification modifications: (a) isotherm time was 3 min without any post-treatments, (b) isotherm time was 3 h without any post-treatments, (c) isotherm time was 6 h without any post-treatments, (d) isotherm time was 3 min and the solid coating was treated with ethanol, (e) isotherm time was 3 h and the solid coating was treated with ethanol and (f) isotherm time was 6 h and the solid coating was treated with ethanol. Blue and red arrows indicate the elongated patterns and nano spherical particles, respectively.

Besides the role of ethanol treatment, the influence of melt heating time of 3 min, 3 h and 6 h at

70°C (isotherm) on the surface morphology of coatings are shown in Figure 2.3a, 2.3b and 2.3c, respectively. Comparing 3 min, 3 h and 6 h shows that the morphology of the solid surface does not significantly change up to 3 h of heating the melt, but after 6 h, porous structure starts to form in some areas of the sample. However, even after 6 h, the smooth morphology is still observed in some areas on the surface and it seems that increase of melt isotherm time has not helped the full transformation of this morphology to a porous structure. It is worth noting that the non-smooth areas of the structure formed in Figure 2.3c, which consists of flakes with different heights resembles the Cassie–Baxter model, in which air is trapped inside the surface pockets underneath the water droplet [39,97]. On the other hand, as mentioned above, the treatment with ethanol has contributed to the increase of air pockets on the surface of all the samples with different isotherm time. Therefore, the study of the sample morphologies shows that a combination of melt isothermal heating and subsequent ethanol treatment of the solidified AKD results in the best outcome for creating micro/nano textures and the desired porous structures.

By comparing Figures A1 and 2.3, it is evident that increasing the isotherm time of the AKD melt at 40°C does not have a significant effect on the surface morphology of the samples. However, when the melt temperature increases to 70°C, by an increase in the isotherm time from 3 min to 6 h, the surface morphology for all samples changes and more porous structures are formed on the surface. We hypothesize that AKD molecules at 70°C have enough energy to be re-arranged and the increase in isotherm time of the melt helps this phenomenon, yielding a more pronounced structure.

To investigate the effect of melt temperature on the morphology of coatings, we heated AKD pellets to a temperature range of 40 to 80°C (with 10°C increments), coated the glass slides individually 3 min after each mentioned temperature was stable and treated the solid coatings with

ethanol for 1 min. Figure 2.4 shows the SEM images of the prepared samples. It can be seen that by increasing the melt temperature from 40 to 80°C, the micro/nano structure of the coatings changes gradually. At 40°C, the structure transforms to a smooth, elongated pattern at 50°C while at 70°C and 80°C, that pattern is turned into an entangled and irregular morphology.

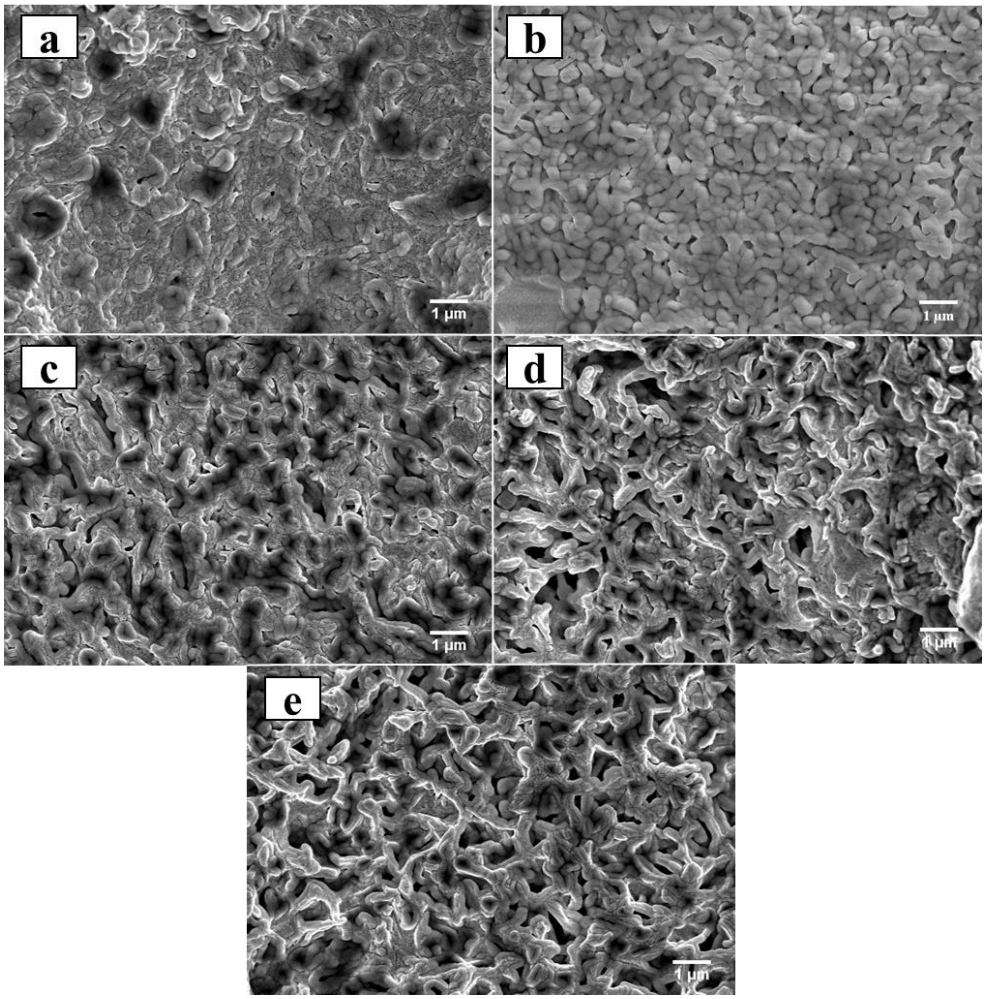

Figure 2.4. SEM images of AKD coating prepared from melts isothermally heated for 3 min at different temperatures, followed by post-solidification ethanol treatment: (a) 40, (b) 50, (c) 60, (d) 70 and (e) 80°C.

From the results of Figures A1, 2.3 and 2.4 it seems that treatment of the melt and subsequent post-solidification ethanol modification are both beneficial for increasing the number of pores on the

surface. On the one hand, ethanol treatment contributes to the modification of the smooth areas of the surface and on the other hand, the use of high-temperature melt results in the formation of more surface pores. Although an extended heating time of the melt (isothermally) helps the development of larger flakes on the solidified coating, combining a short heating time (3 min) with subsequent post-solidification ethanol immersion provides the required morphology for having a superhydrophobic surface in the final product. In contrast to the method of Feng *et al.* [83], this approach is also beneficial for industrial applications since energy is a valuable source and replacing it with a simple organic solvent that can be used for several times could be an alternative solution.

To study the impact of post-solidification time on the surface morphology of AKD, we left the as-solidified coating (obtained from the melt held at 70°C For 3 min) at room temperature for 4 days to let the sample be cured over time with no extra modifications (Figure 2.5a). Moreover, to investigate the effect of pre-curing ethanol treatment on such coatings, we dipped a similarly-prepared solid sample in ethanol for 1 min and let it dry before curing at room temperature for 4 days (Figure 2.5b). According to Figure 2.5a, the sample cured over time has developed a big flake-like microstructure, the morphology of which has been already shown by the previous studies [39,83]. In addition, according to Figure 2.5b, after the formation of the stable phase over time, ethanol can no longer play an effective role in changing the morphology of the sample. We hypothesize that ethanol is effective when the smooth metastable phase is present in the sample (uncured AKD). However, in the sample cured over time, this phase has been already transformed to the stable phase and therefore, ethanol treatment has almost no influence.

In the next step, the effect of post-treatment time on the morphology of the ethanol-modified AKD was studied. First, a glass slide was dip-coated in a 70°C melt, isothermally heated for 6 h. Then,

the solidified coating was treated with ethanol (Figure 2.5c). Second, the very same sample was cured over time for 4 days (Figure 2.5d). According to SEM images, it is seen that the entangled and irregular micro/nano pattern available in the ethanol-treated sample before curing over time (Figure 2.5c) has turned into an organized micro scaled flake-like pattern after 4 days (Figure 2.5d).

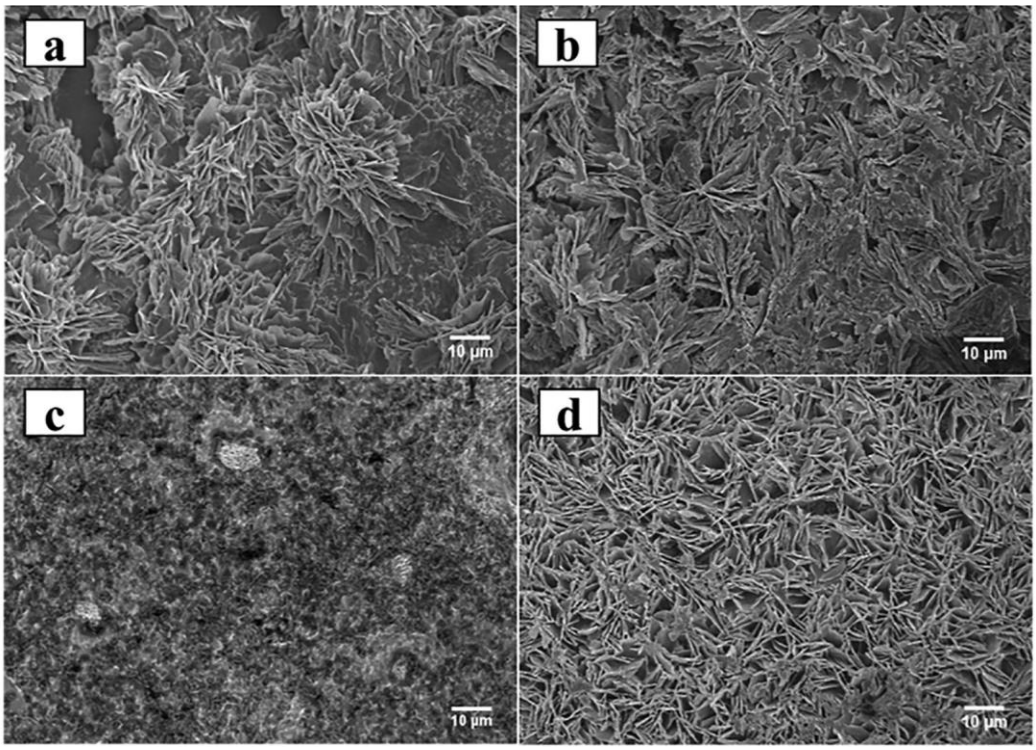

Figure 2.5. SEM images of AKD samples prepared from heated melt at 70°C with different isotherm times and post-solidification modification: (a) isotherm time was 3 min and the sample cured over 4 days without any post-modifications, (b) a similarly-prepared sample of part (a) was treated with ethanol prior to curing, (c) isotherm time was 6 h and then the solid coating was treated with ethanol and (d) the same sample in part (c) left at room temperature for 4 days.

By comparing all the SEM images of AKD samples (Figures 2.2-2.5 and Figure A1), it is observed that as-solidified AKD near its melting point (ca. 40°C) forms almost no micro/nano structures. The smooth regions on the surface explain why the surface shows a slightly-hydrophobic behavior.

However, by isothermally heating the melt for a longer period of time at high temperatures (~70°C), these flat parts are converted to entangled micro/nano structures. The results show that as the temperature of melt and isotherm time increase, more pores form on the surface. However, even after a long time of heating the AKD melt at high temperatures, some flat regions still remain on the surface. Here, it is shown that ethanol treatment is an effective method to turn these smooth regions into micro/nano structures, which in turn will lead to improved wetting properties of the surface.

FT-IR spectroscopy was used to determine the functional groups and available chemical bonds in the samples. Figure A2 illustrates the spectra of three samples prepared from a 70°C melt isothermally heated for 3 min: (i) as-solidified AKD, (ii) ethanol-treated AKD right after solidification and (iii) cured AKD over time with no extra modifications. Sharp peaks at 1720 cm^{-1} and 1847 cm^{-1} are related to C=C double bond and C=O double bond in carboxyl group of lactone ring, respectively [98]. Some of the structural motifs, such as the C(=O)O, are retained after polymerization [99]. The peak at 1467 cm^{-1} is related to the bending mode of CH_2 bonds. Moreover, sharp peaks from 2845 cm^{-1} to 2955 cm^{-1} are because of C–H stretching vibrations. According to Figure A2, it is seen that neither ethanol treatment nor long curing process of AKD has a noticeable impact on the functional groups of the as-solidified AKD.

To study the relationship between the surface chemical bonds and the wettability, XPS analysis was performed on the very same samples studied using FT-IR. Carbon and oxygen are two elements that were detected by XPS, the peaks of which appeared at ~285 eV and ~532 eV, respectively. According to Figure A3, the as-solidified sample, sample treated with ethanol and sample cured over time are mainly composed of carbon with 92.47, 95.67 and 94.72 at.%, respectively. According to the low amount of oxygen in the samples, which is between 4.33 to

7.53 at.%, it can be concluded that its effect on the wettability is negligible. The results are in agreement with the study of Shen *et al.* [84], which indicated that AKD is dominated by saturated hydrocarbon chains.

The XPS results reveal that in both processes of curing over time and ethanol treatment, there are no noticeable changes in the chemical bonds, which is entirely in agreement with the FT-IR conclusions. Comparing the results of XRD, SEM, FT-IR and XPS suggests that in the curing process of AKD, surface morphology is the critical parameter and possibly has more influence on its wetting behavior than the surface chemistry. During this process, the degree of crystallization of AKD increases and air cushions and pores are formed on the surface resulting in improved contact angle and hydrophobicity. It is observed that this phenomenon also happens in the treatment of as-solidified AKD with ethanol. Organic solvent treatment has a substantial impact on the surface morphology of solidified AKD and decreases the required curing time by stimulating the formation of a porous structure on the polymer surface.

Moreover, the topography of the aforementioned samples was constructed using a confocal laser scanning microscope (Figure 2.6). According to Figure 2.6a and 2.6c, there are so many bumps and dents on the surface of the untreated samples. However, after treating the samples with ethanol, the bumps are removed. The mean diameter and fraction of the Surface pores for the samples prepared from isothermally heated melt for 3 min at 40°C and 70°C were measured by an image-processing software and the results are reported in Table 2.1. According to the results, it is seen that both elements of ethanol treatment and high melt temperature increase the pores fraction and as a result, more air cushions are formed on the surface [14]. The roughness average (R_a) and Root Mean Square (*RMS*) values of the surface (Table 2.1) show that, compared to untreated samples, ethanol treatment has decreased the roughness of the samples. Therefore, it can be concluded that

the surface roughness does not have a significant role in improving superhydrophobicity after ethanol treatment. On the other hand, the increased fraction of the surface pores is more prominent in enhancing these properties.

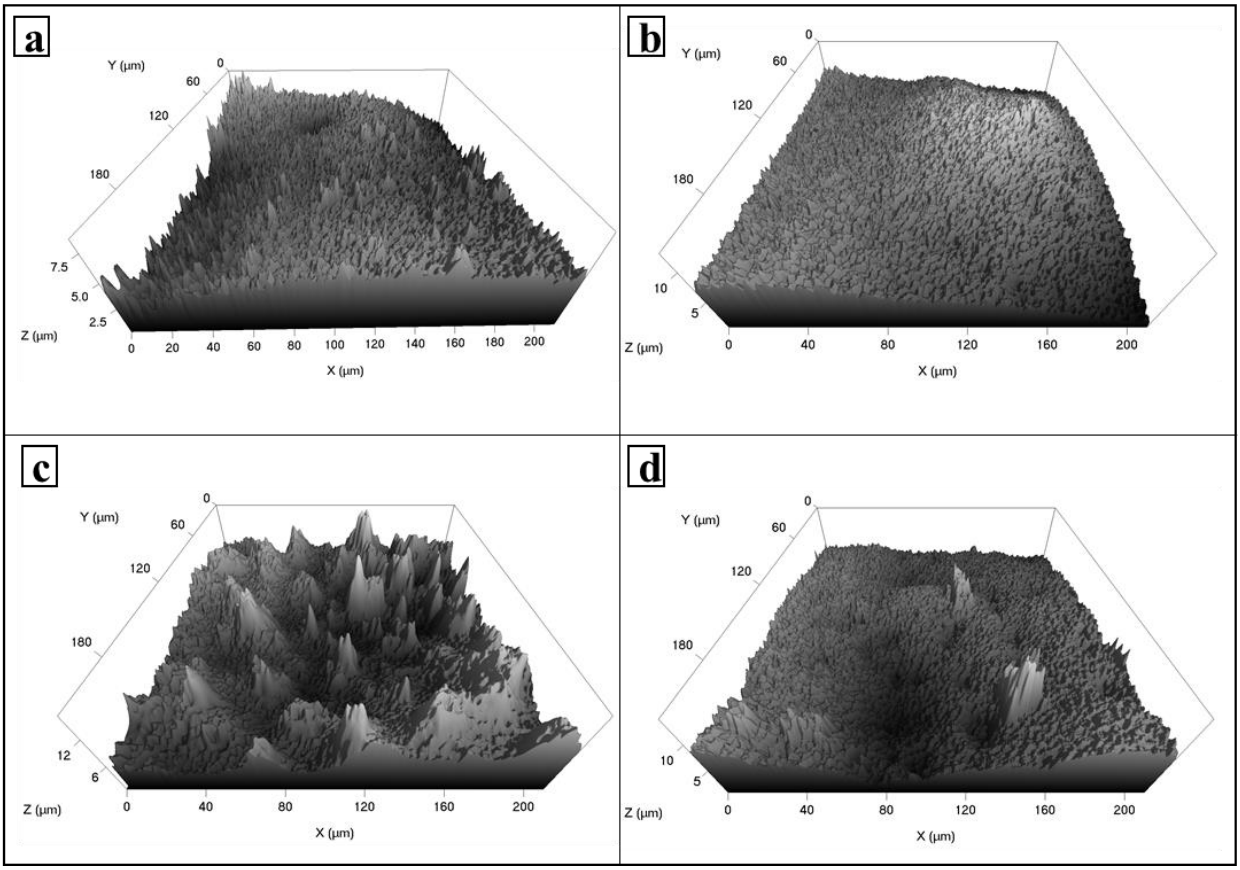

Figure 2.6. Topography of AKD coating prepared from melts isothermally heated for 3 min at different temperatures with different post-synthesis modifications: (a) the melt was isothermally heated at 40°C without any post-solidification treatments, (b) the melt was isothermally heated at 40°C min and the solid coating was treated with ethanol, (c) the melt was isothermally heated at 70°C without any post-solidification treatments, (d) the melt was isothermally heated at 70°C min and the solid coating was treated with ethanol.

Table 2.1. The impact of ethanol treatment of the solid coatings, obtained from the isothermally heated samples for 3 min at different temperatures, on the pores size and roughness of the samples

Sample	Melt temperature (°C)	Pores mean diameter (µm)	Pores fraction (%)	R_a (µm)	*RMS* (µm)
As-solidified AKD	40	0.119±0.056	9.75±3.45	0.680	0.858
	70	0.202±0.138	19.00±3.27	0.867	1.194
Ethanol-treated AKD	40	0.120±0.054	24.80±2.45	0.600	0.788
	70	0.139±0.046	27.38±3.00	0.720	0.934

To investigate the superhydrophobicity of the AKD coatings, advancing and receding contact angles were measured at 9 randomly-chosen spots on each sample. Table 2.2 shows the average values of the advancing and receding contact angles of the samples with water to compare the impact of the molten AKD's temperature, isothermal heating time of the melt and post-solidification ethanol treatment on wetting properties. According to Table 2.2, advancing and receding contact angles of as-solidified AKD from an isothermally heated melt at 40°C for 3 min are 92.9±3.0 and 78.4±4.7°, respectively. It is seen that after ethanol treatment of the very same sample for 1 min, the surface becomes superhydrophobic with significantly enhanced advancing and receding contact angle values of 158.7±1.4 and 156.8±0.9°, respectively. It can be concluded that the micro/nano structure that is formed on the surface of the samples after ethanol treatment has increased the number of air pockets on the surface; therefore, due to the low surface energy of solidified AKD, the final sample shows excellent superhydrophobicity. It is worth noting that this treatment has also greatly improved the contact angle hysteresis (the difference between advancing and receding angles) of the samples.

Moreover, by increasing the temperature of the melt from 40 to 70°C and also heating the melt isothermally for 6 h, it is observed that advancing and receding contact angle values of the untreated samples significantly improve from 93.4±4.1 and 80.9±7.6° to 144±7.6 and 137.5±8.0°, respectively. However, when we increase the heating time from 3 min to 6 h at 40°C, the advancing and receding contact angle values only increase by 5.3% and 13.5%, respectively, which is entirely in agreement with Figure A1. Based on these results, therefore, it can be concluded that increasing the heating time at low temperatures (40°C) does not markedly change the surface morphology and by measuring the dynamic contact angles, it is proved that the superhydrophobic properties of these samples do not increase. In contrast, for the samples prepared from the melt at a higher temperatures (i.e., 70°C), by increasing the heating time from 3 min to 6 h, advancing and receding contact angles increase by 54.2% and 70.0%, respectively. According to Figure 2.3, an increase in the heating time from 3 min to 6 h results in a morphology containing irregular patterns being more prone to trapping air under the droplet. It also can be concluded that the impact of heating time is significantly dependent on the temperature of molten AKD. We hypothesize that this phenomenon occurs due to the polymerization process of molten AKD over time and can be an interesting subject for future studies.

To study the effects of molten AKD's temperature and ethanol treatment of the coatings on the dynamic contact angles, we increased the temperature of the melt from 40 to 70°C (held isotherm for 3 min) and treated the sample with ethanol after solidification. It is seen that the advancing and receding contact angles are 160.5±1.1 and 158.5±1.5°, respectively; therefore, the molten AKD's temperature plays an important role in the wettability of the samples. In order to make the sample with the highest dynamic contact angles, we optimized the values of AKD's melt temperature, melt isothermal holding time and ethanol treatment. When as-solidified AKD from an isothermally

heated melt at 40°C for 3 min is compared to solid coating from the isothermally heated melt at 70°C for 6 h and then treated with ethanol, a remarkable rise is noticed (Table 2.2). The advancing and receding contact angles increase from 92.9±3.0 and 78.4±4.7° to 163.7±1.3 and 162.6±1.2°, respectively. We also measured the dynamic contact angles of the cured samples over 4 days after their solidification. When the dynamic contact angles of solidified samples treated with ethanol are compared to the non-modified samples cured over time, it is found that the difference is not noticeable. This shows that with the low surface energy of as-solidified AKD, the formed micro/nano structures by ethanol treatment make the surface superhydrophobic in a very short period of time. By comparing the results, it is clear that our facile, fast and low-cost method (i.e., isothermally heating the AKD melt at 40°C for 3 min and then treating the solid coating with ethanol) is a good alternative to other methods of improving the hydrophobicity of this polymer such as curing it over an extended period of time and/or heat treatment of the as-solidified samples. In addition, since the organic solvent (ethanol), utilized in our method, can be used several times, a huge amount of energy will be saved when the fabrication is scaled up for industrial applications.

In the previous section, it was shown that increasing both melt temperature and isothermal heating time are beneficial for improving the superhydrophobic properties of AKD. Figure 2.7a shows the impact of different melt temperatures from 40 to 80°C on the wetting behavior of AKD samples from isothermally heated melt with different isotherm times. According to the results, by increasing the melt temperature up to 70°C, the dynamic contact angles of all samples increase, the optimal melt temperature of which is 70°C resulting in the highest advancing and receding contact angles for all samples with different isotherm times.

Figure 2.7b demonstrates the impact of molten AKD isothermal heating time for 3 min, 3 h, 6 h and 9 h at 70°C (the optimal temperature) on the advancing and receding contact angles of ethanol-

treated samples. From this figure, it is clear that by increasing the melt heating time up to 6 h, both advancing and receding contact angles of the ethanol-treated samples increase. The maximum values, obtained at t = 6 h, are 163.7±1.3 and 162.6±1.2° for advancing and receding contact angles, respectively.

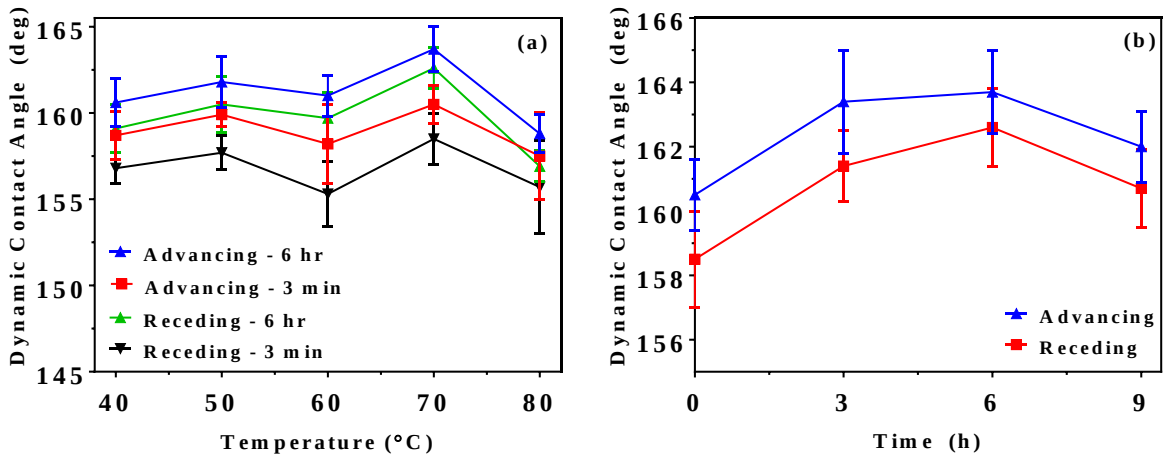

Figure 2.7. Advancing and receding contact angles of ethanol-treated solidified AKD from: (a) isothermally heated melt at 40 to 80°C for 3 min and 6 h and (b) isothermally heated melt at 70°C for 3 min, 3 h, 6 h and 9 h.

Table 2.2. The impact of melt temperature, isothermally heating time, ethanol treatment and curing over time (with no extra modifications) on advancing and receding contact angles of AKD

Sample	Melt temperature (°C)	Isothermally heating time	Advancing contact angle (°)	Receding contact angle (°)
As-solidified AKD	40	3 min	92.9±3.0	78.4±4.7
		6 h	97.8±6.0	89.0±7.0
	70	3 min	93.4±4.1	80.9±7.6
		6 h	144.0±7.6	137.5±8.0
Ethanol-treated AKD	40	3 min	158.7±1.4	156.8±0.9
		6 h	160.6±1.4	159.1±1.4
	70	3 min	160.5±1.1	158.5±1.5
		6 h	163.7±1.3	162.6±1.2
As-solidified AKD cured after 4 days	40	3 min	159.8±0.7	157.7±1.5
		6 h	160.9±1.9	156.0±2.0
	70	3 min	160.8±1.7	157.1±1.4
		6 h	161.3±1.3	157.4±0.7

By comparing Table 2.2 and Figure 2.7, it is seen that the as-solidified samples before ethanol treatment are not superhydrophobic due to their smooth surface that covers a large region of the samples. It is well worth mentioning that this phenomenon occurs when there are not enough air cushions on the surface and the water droplet rests on the solid layer. This is interpreted as a Wenzel state and the solid-liquid interface follows the smooth texture of the surface. As soon as the as-solidified samples are treated with ethanol, it is seen that the advancing and receding contact angles exceed 150° and the samples become superhydrophobic. This behavior is due to the regime transition from Wenzel to Cassie [6]. During this process, so many micro/nano particles are formed on the surface of the samples and the air is trapped in the pores.

The result from Figure 2.7 is in agreement with the SEM images shown in Figures A1, Figure 2.3 and Figure 2.4. We showed that by increasing the melt temperature and heating time, due to the surface morphology change and increasing the pores fraction on the surface, dynamic contact

angles increase (see Table 2.1). Besides, by comparing Figure 2.6a and 2.6b as well as Figure 2.6c and 2.6d, it can be seen that the outstanding large patterns are completely removed after ethanol treatment. The mechanism of this process has been attributed to the solubility of the monomer in the porogenic solvent and phase separation of the formed polymer after solvent evaporation [100,101]. The role of ethanol is to dissolve the smooth structures containing monomers and help nano-patterns to separate and stand out. This promotes the increase of pores fraction, which is beneficial for improving the superhydrophobic properties of the surface.

In order to study the efficiency of the introduced dip-coating method on the materials other than the glass slides, a piece of standard hydrophilic paper was examined. We followed the same procedure, already mentioned in the Experimental section for coating the glass slides, to fabricate a thin layer of AKD on the paper. The surface morphology of the paper sample prepared from an isothermally heated melt at 70°C for 3 h with no ethanol treatment is illustrated in Figure 2.8a. It is seen that there are some shallow porous structures embedded in a rather smooth surface. By treating the same sample with ethanol for 30 s, these structures have transformed to entangled patterns containing deep holes with different sizes that are indicated in Figure 2.8b. It seems that ethanol treatment has significantly changed the smooth parts on the surface. The creation of these pores results in the transition to Cassie-Baxter state and formation of air pockets on the surface [5,6]. Moreover, we measured the dynamic contact angles of the droplet on the paper before and after ethanol treatment. The results show that advancing and receding contact angles increase from 146.8±4.1 and 143.2±4.1° to 158.4±2.2 and 156.7±2.9°, respectively. It is worth mentioning that not only has ethanol treatment increased the dynamic contact angle values, but it also has decreased the standard deviations showing the improved consistency of the wettability over the entire surface.

Interest in the preparation of superhydrophobic papers due to their broad applications in the industry is growing and as a result, several methods have been proposed to increase the contact angle of papers. For example, Peng *et al.* prepared a superhydrophobic paper with enhanced physical strength using a layer-by-layer self-assembly of poly (allylamine hydrochloride) (PAH) and lignosulfonates-amine (LSA) that followed by 30 min of heat treatment at 160°C, which led to a contact angle of as high as 151.7° [102]. Moreover, plasma treatments [103] and the rapid expansion of supercritical solutions [76] are other techniques to increase the contact angle of paper to more than 150°. Although these sophisticated methods have some advantages, they require specialized and expensive instruments that make their applications limited. In our low-cost method, presented here, we are able to obtain advancing contact angles of as high as 158.4±2.2° through two simple steps without using any costly instruments or toxic chemicals (see Table A1 for comparison among all methods). Inset of Figure 2.8b shows a digital photo of water droplets with a volume of ~3 µl on a printed standard hydrophilic paper that is coated with AKD melt (isothermally heated at 70°C for 3 h) after treatment with ethanol. The non-wettable properties of the paper are clearly shown by blue droplets standing on it.

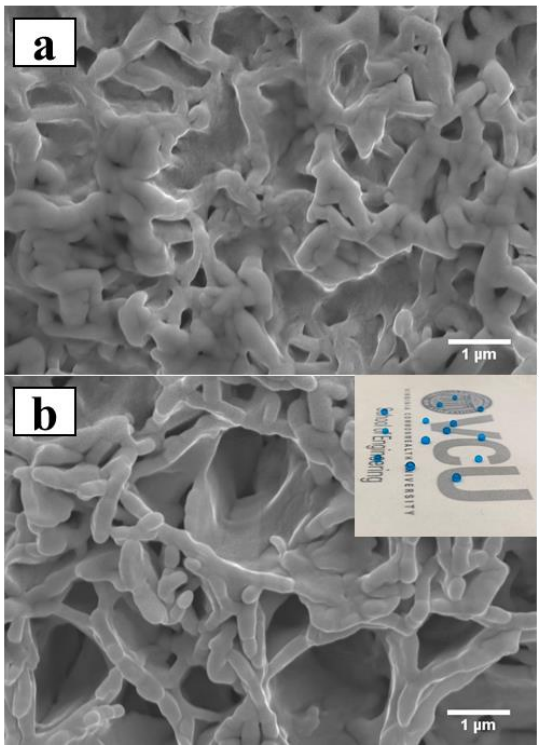

Figure 2.8. SEM images of an AKD coating obtained from an isothermally heated melt at 70°C for 3 h on a piece of standard paper: (a) as-solidified and (b) the solid coating was treated with ethanol for 30 s – inset: digital image of water droplets on the surface of the treated paper with ethanol.

Finally, to find the efficiency of our method with other organic solvents, we repeated our experiments by treating the AKD coating on the glass slides with ethanol, methanol and isopropanol to measure advancing and receding contact angles of as-solidified AKD from an isothermally heated melt at 70°C for 3 min. According to Table A2, it is seen that all the samples are superhydrophobic and their advancing and receding contact angles exceed 150°. The difference between the dynamic contact angle values for the organic solvents is not noticeable and all of them are effective in improving the superhydrophobicity. These results show that this method has flexibility in solvent selection and a wide range of available solvents can be used for surface

treatment. However, due to lower flammability and toxicity, ethanol was chosen for this study and is recommended for large-scale applications.

2.4 Conclusions

We used a facile method to transform inexpensive alkyl ketene dimer (AKD) to a superhydrophobic surface in less than 10 min. A brief ethanol treatment of the as-solidified coating, prepared from a 40°C melt, impressively boosted the advancing and receding contact angles from 92.9 and 78.4° to 158.7 and 156.8°, respectively. This superhydrophobic performance was even further improved by ramping up the temperature of the melt from 40 to 70°C, leading to increased advancing and receding contact angles of 160.5 and 158.5°, respectively. The results show that the temperature and isothermal heating of the AKD melt before solidification as well as the solvent treatment of the solid coatings are crucial parameters that significantly influence the wetting behavior of this material. By using ethanol treatment as a facile approach, the smooth surface morphology of the samples successfully transformed to a very porous structure containing micro/nano textures causing the transition of droplet state from Wenzel to Cassie [5,6,57]. Besides ethanol, this technique was also demonstrated to be working with some other organic solvents such as methanol and isopropanol. In addition to glass, our method seems to also work for other substrates including paper. This study further approves the previous findings on the curing mechanism of AKD, i.e., increasing the degree of crystallization by transforming from a metastable to a stable state [40,82–84]. Unlike the previous reports, however, instead of benefiting from the low surface energy of non-eco-friendly compounds (like fluorochemicals) [63–65], turning to sophisticated and expensive methods (e.g., supercritical carbon dioxide) [76,77], using expensive polymers and highly toxic solvents [89] and utilizing post UV or microwave curing [89], we sought to exploit a commonly used green chemical and innovated a simple method (dip-

coating in ethanol) with a short reaction time (<10 min) without using any highly-toxic solvent or post-curing step (Table A1).

Here we compare our material and method with three common methods to fabricate superhydrophobic coatings:

Table 2.3. Comparison of the fabrication cost of superhydrophobic coatings

Material	Fabrication Method	Fabrication Cost (per m^2)
Aluminum Coatings	Sputtering	$100-200
Commercial Sprays	-	$3
Alkyl Ketene Dimer	Dip-Coating	$0.26

One of the common methods to fabricate superhydrophobic substrates is using aluminum as the base and manufacturing micro/nano textures on the surface. Magnetron sputtering must be utilized to fabricate a thin layer of aluminum as a superhydrophobic coating, which is a costly method ($40 per hour). Since the fabrication of 1 m^2 of aluminum takes several hours, the final superhydrophobic coating will cost approximately a few hundred dollars. Using commercial sprays is another method to improve the non-wettability of substrates. A 200 ml of commercial sprays costs roughly $15 and it can cover up to 5 m^2. Although this method is more facile and cheaper than the previous one, it causes environmental issues and is not durable. The last one is our facile method, where we used inexpensive AKD ($2.64 per kilogram) to fabricate superhydrophobic coatings. To fabricate 1 m^2 of this coating, around 100 gr of AKD pellets must be melted at ~40 ℃. Consequently, the fabrication cost of 1 m^2 of this coating will be around less than $1, significantly lower than the previous methods.

Chapter 3. Further Step toward a Comprehensive Understanding of the Effect of Surfactant Additions on Altering the Impact Dynamics of Water Droplets

3.1 Introduction

In the last decade, controlling the spreading and retraction of liquid droplets has become an uprising field in various practical applications including spray cooling [41], inkjet printing [42], aerosol drug delivery [43], surface cleaning [45] and agrochemical sprays [46]; as a result, this area has widely attracted attention from researchers. For example, showing the remarkable importance of this phenomenon in the industry, it has been reported that more than half of the pesticides are wasted, due to their undesired bouncing on the crop leaves [104], which in turn, results in low efficiency of the pesticides as well as environmental pollution. The impact dynamics of pure liquids have been broadly explored by prior studies [8,87,105–108]. Two main dimensionless parameters describing the behavior of the droplets during the impact are spreading factor (d/D_0) and flattening factor (h/D_0), where d, h and D_0 are the instantaneous diameter, height and initial diameter of the impinging droplet. Several studies have proposed theoretical and computational models to predict the maximum spreading diameter of pure liquids during the impact on horizontal substrates by applying the energy conservation between the two moments just before the impact and the maximum diameter that the droplet reaches [109–114].

The most challenging issue in this field is the fact that in almost all the applications mentioned earlier, a surface-active agent or a surfactant is added to the pure water, which results in a significant change in its predicted dynamic behavior due to the time-dependent surface tension of the impinging droplet. Thus, to control the impact outcomes of the aqueous surfactant-laden droplets, it is indispensable to understand how these additives alter the impact dynamics [115–119].

To address this question, Crooks *et al.* studied the spreading and recoil phases of the surfactant-laden droplets on hydrophobic parafilm surfaces using a high-speed camera at 1000 frames per second (fps). They showed that when the concentration of the solution is below the critical micelle concentration (CMC), the recoil behavior is controlled by the hydrodynamics in the droplets. Moreover, for solutions having concentrations > CMC, this phenomenon is governed by the demicellisation [118]. Pasandideh-fard *et al.*, as one of the pioneers in this field, numerically and experimentally investigated the influence of dynamic surface tension on the dynamic behavior of water and surfactant-laden droplets on a flat stainless-steel. They showed that although surfactant addition (~0.5×CMC) does not change the shape of the droplet in the spreading phase, it affects the retraction dynamic [120]. In another study, Aytouna *et al.*, used five different non-ionic surfactants to study the effects of dynamic surface tension on the spreading and retraction of aqueous surfactant-laden drops on a hydrophobic surface [121]. As a follow-up on the mentioned studies, Gatne *et al.* investigated the role of diffusion and interfacial adsorption rate of surfactants in the spreading and retraction phases of impact dynamics [122].

Despite the substantial role of surfactant additions in changing the dynamic behavior of pure water droplets, only a few studies have characterized the impact dynamics of these droplets. Most of the prior studies are focused on the role of dynamic surface tension on the impact dynamics. Moreover, they are limited to the characterization of droplet impact on either a hydrophobic or hydrophilic substrate [123]. Therefore, the current study aims to extend the existing literature to shed light on the influence of critical parameters, including the ionic nature, molecular weight (MW) and concentration (~0.2 – 2×CMC) of the surfactants, on the spreading and retraction of surfactant-laden droplets.

To our knowledge, this is the first comprehensive report on the influence of surfactant additions to pure water on the impact outcomes. Moreover, the relationship between the contact time of the droplet during the impact and performance of the surfactant additions is thoroughly studied. To gain a solid conclusion on the influence of the mentioned parameters, we conducted a series of systematic experiments, where the Weber number ($We = \rho V^2 D_0/\gamma$), which is a function of density (ρ), impact velocity (V), initial diameter (D_0) and surface tension (γ) of the impinging droplet, varied from ~6-353. We believe that the present work will contribute to obtaining a better understanding of controlling the impact dynamics of the aqueous surfactant-laden droplets with an insight into enhancing the efficiency of utilizing these surfactants in industry.

3.2 Experimental Section

Figure 3.1 shows the experimental apparatus used in the present work. This apparatus includes a precise droplet generator (DSA25E, Krüss, Germany) with a precision syringe controlled by a personal computer. It also includes a calibrated vertical stand. Pursuant to the energy conservation stating that the potential energy of the released droplet is equal to its kinetic energy at the moment of impact, the impact velocity was measured based on the $V = \sqrt{2gh}$, where g is the gravational constant (9.81 m/s^2) and h is the droplet release height. The vertical stand enabled us to obtain an impact velocity of 0.4 to 2.4 m/s with 0.5 m/s increments by precisely varying the release height of the droplets from 8 to 294 mm.

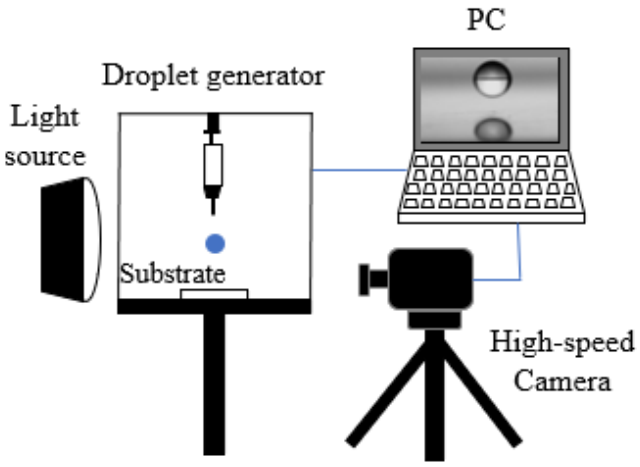

Figure 3.1. Schematic of the experiment apparatus.

To clearly understand how contact time influences the impact dynamics in the presence of surfactants, three substrates with various wetting properties ranging from hydrophilic to superhydrophobic were used. Glass slides (AmScope, USA) were used as a hydrophilic surface. For the hydrophobic sample, we used a thin sheet (~0.5 mm) of polytetrafluoroethylene (PTFE), which was previously polished with 600, 800 and 1200 grit silicon carbide sandpapers (Allied high tech productions, USA) to achieve a uniform surface. Prior to conducting each experiment, the glass slides and PTFE substrates were cleaned with ethanol, rinsed with de-ionized (DI) water (Resistivity = 18.2 MΩ.cm, from MiliQ, Milipore, USA), wiped with Kimwipes (Kimberly-Clark Professional, USA) and completely dried with compressed air at room temperature.

Finally, to produce our superhydrophobic substrates, we coated new glass slides with a thin layer of molten alkyl ketene dimer (AKD) at 70 °C. Then, the coated slides were solidified after 2 min and cured over 4-6 days at room temperature to become superhydrophobic. More details regarding the fabrication of the superhydrophobic samples are given in Chapter 2 [12]. In order to ensure that the non-wettability of the superhydrophobic samples does not change due to the surfactant residues from the previous experiments, fresh samples were fabricated and used in each

experiment. The static water contact angle of these samples was measured using a goniometer (DSA25E, Krüss, Germany) at 5 randomly-chosen points. Moreover, we measured the surface free energy of the substrates using the contact angle method [124]. We used pure water and diiodomethane (Fisher Scientific, USA) as the polar and non-polar liquids, respectively. The total surface tension of pure water and diiodomethane was measured with the above-mentioned goniometer, which were equal to 72.8 and 48.5 mN/m, respectively. However, the dispersive and polar components of the total surface energy of the liquids were found from the data available in the literature [124]. To further investigate the surface morphology and measure the surface roughness, all the substrates were characterized using a confocal laser scanning microscope (Zeiss LSM 710, Germany) and scanning electron microscope (SU-70, Hitachi, Japan).

As it is shown in Figure 3.1, we placed the substrates on a flat table perpendicular to the needle and captured the evolution of droplets using the Phantom high-speed camera (USA) at 10000 fps. To obtain the frontal view of the droplet impact, the high-speed camera was aligned at 0° to the samples and a powerful lighting system, which was equipped with a white reflector, was utilized to provide sharp videos with high contrast. In the next step, to analyze the captured videos and measure the droplet size, spreading and flattening factors, post-impact oscillations, etc., the software of the camera was used to tune the brightness and contrast of the videos. Then, the videos were analyzed with a commercial image-processing software (Tracker 5.1.5).

To study the influence of ionic nature of the surfactants on the impact dynamics, we used sodium dodecyl sulfate (SDS), hexadecyltrimethylammonium bromide (CTAB) and n-decanoyl-n-methylglucamine (MEGA-10), which are respectively categorized into three groups: (1) anionic, (2) cationic and (3) non-ionic, in accordance with the composition and polarity of the heads of their molecules. More details, including the chemical formula, ionic properties, molecular weight,

CMC and the concentrations used in this study are given in Table 3.1. Note that all the mentioned surfactants were purchased from Sigma-Aldrich (USA). We prepared 100 ml solutions of the surfactants with each of the desired concentrations reported in Table 3.1. Then, the equilibrium surface tensions of the solutions were measured at least 10 times for each sample at room temperature using a goniometer (DSA25E, Krüss, Germany) with pendant droplet method. For each solution, a separate non-stick needle with an outer diameter of 1.52 mm and a disposable syringe were used. It should be pointed out that before measuring the equilibrium surface tension of the solutions, the instrument was calibrated by measuring the surface tension of DI water, which is equal to 72.8 mN/m.

Table 3.1. Physicochemical properties and desired concentrations of SDS, CTAB and MEGA-10

Surfactant Name	Chemical Formula	Ionic Nature	MW (g/mol)	CMC (mM)	Concentration (mM)
SDS	$C_{12}H_{15}SO_4$	Anionic	288.4	7-10	2
					4
					8
					16
CTAB	$C_{19}H_{42}BrN$	Cationic	364.5	0.92	0.2
					0.45
					0.9
					1.8
MEGA-10	$C_{17}H_{35}NO_6$	Non-ionic	349.5	6-7	0.5
					2
					7
					14

3.3 Results and Discussion

Table 3.2 shows the results of surface characterization of the impact substrates, including their contact angle values with water and diiodomethane, surface free energy and root mean square (*RMS*). More details of the surface morphology and topography of AKD, PTFE and glass substrates are given in the supporting information (Figures A4 and A5). By comparing the surface morphology (Figure A4), surface topography (Figure A5), surface free energy and roughness of the substrates, it is seen that AKD having the lowest surface free energy of 11.02 mJ/mm^2, highest surface roughness of 2.92 µm and distinct features resembling air pockets on the surface, shows the highest non-wettability with a static water contact angle of 156.9±0.58°. PTFE and glass slides with higher surface free energy and lower surface roughness show a lower degree of non-wettability. This phenomenon has been comprehensively investigated in our recent study on the superhydrophobic surfaces [12].

Table 3.2. Characterization of the impact substrates, including their contact angle values with water and diiodomethane, surface free energy and *RMS*

Substrate	Water Contact Angle (°)	Diiodomethane Contact Angle (°)	Surface Free Energy (mJ/mm^2)	*RMS* (µm)
AKD	156.9±0.58	85±0.90	11.02	2.92
PTFE	102.9±2.72	75±1.12	23.42	0.48
Glass	73.15±1.83	70±1.03	38.06	0.13

The concentration of the surfactants has a vital role in the gas-liquid interfacial tension of solutions. In order to study the influence of this parameter on the dynamic behavior of the aqueous surfactant-laden droplets, the concentrations of SDS, CTAB and MEGA-10 solutions were varied in the range of 2-16, 0.2-1.8 and 0.5-14 mM corresponding to ~0.2 to 2×CMC. Figure 3.2 shows the

equilibrium surface tension of the solutions with respect to the concentration. According to the results, by increasing the concentration of each solution, the corresponding equilibrium surface tension dramatically decreases and reaches a plateau over the range of its CMC (indicated by dashed lines), which is in agreement with previous reports [117,125]. At this point, by further enhancing the concentration, no significant change occurs in the surface tension. Then, a bilayer molecule of surfactants is formed on the interface [126].

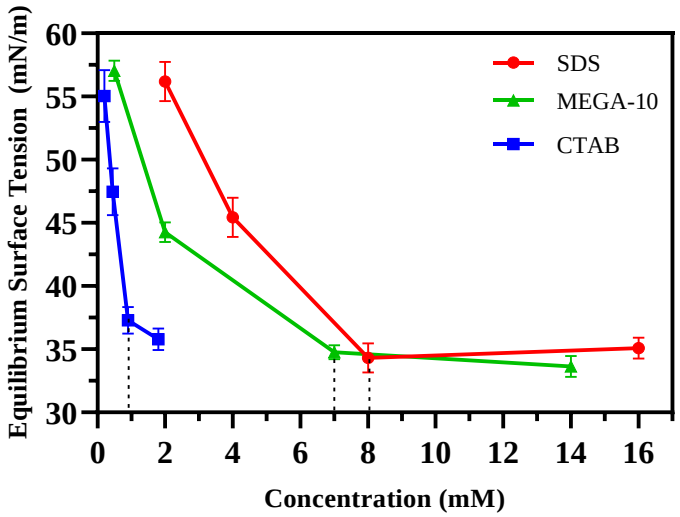

Figure 3.2. Equilibrium surface tension of SDS, MEGA-10 and CTAB with respect to the concentration. The dashed lines indicate the CMC of each surfactant, which is equal to ~8, 7 and 0.92 mM for SDS, MEGA-10 and CTAB, respectively.

The solutions were divided into four groups based on their equilibrium surface tension, the results of which are shown in Table 3.3. We were able to achieve a Weber number of ~6-353 by varying the impact velocity (0.4-2.4 m/s) and equilibrium surface tension (34.84±0.89 to 56.09±0.81 mN/m) of the impinging droplets having a density similar to those of DI water [122] and an initial diameter of 2.05±0.05 mm. It should be noted that based on the previous studies, surfactant addition slightly alters the viscosity of water. However, this slight difference can be negligible

compared to the remarkable decrease in the surface tension of the solution, which can considerably influence the dynamic behavior of the solutions [122,127].

Table 3.3. Four groups of the solutions of SDS, CTAB and MEGA-10 at various concentrations having comparable equilibrium surface tension values

Group	Surfactant Name	Concentration (mM)	Equilibrium Surface Tension (mN/m)
1	SDS	2	56.19±1.54
	CTAB	0.2	55.05±2.07
	MEGA-10	0.5	57.04±0.81
2	SDS	4	45.44±1.56
	CTAB	0.45	47.47±1.87
	MEGA-10	2	44.27±0.78
3	SDS	8	35.12±1.16
	CTAB	0.9	37.28±1.06
	MEGA-10	7	35.26±0.56
4	SDS	16	35.08±0.84
	CTAB	1.8	35.80±0.86
	MEGA-10	14	34.64±0.83

Due to the significant difference among the equilibrium surface tension of each group, in order to generate aqueous surfactant-laden droplets with a similar diameter of 2.05±0.05 mm, two non-stick needles with an outer diameter of 0.33 and 0.58 mm were used. Since the surface tension of DI water (72.8 mN/m) was markedly higher than that of the solutions, a larger non-stick needle with an outer diameter of 1.52 mm was used, which resulted in DI water droplets having a diameter of 4.09 mm.

For example, Figure 3.3 shows the shape evolution of the DI water droplet as well as the droplets of the third group of solutions at c = CMC (c is the concentration of the solutions) having an equilibrium surface tension in the range of 35.12-37.28 mN/m, in the first 50 milliseconds (ms)

after impacting the hydrophilic glass substrates. It is to be noted that the surface tension values of the solutions at their critical micelle concentrations are very close with a difference of about 5 percent. Based on the surface tension and initial diameter of DI water droplets, to have a similar Weber number of 46.07±1.38 for all the droplets, the release heights were 40.5 and 41.0 mm for DI water and the solutions, respectively.

According to the energy balance, during the spreading phase of the impact, a portion of the energy of the droplet at state 1 (just before the impact), including kinetic and capillary energies, transforms into the capillary energy of the droplet at state 2, where the maximum spreading diameter occurs. During the spreading phase, due to the viscous dissipation, the rest of the initial energies is lost. It is to be noted that wetting area and t_{max}, which is the required time for the droplet to reach its maximum diameter, are two of the main parameters influencing the energy loss [128].

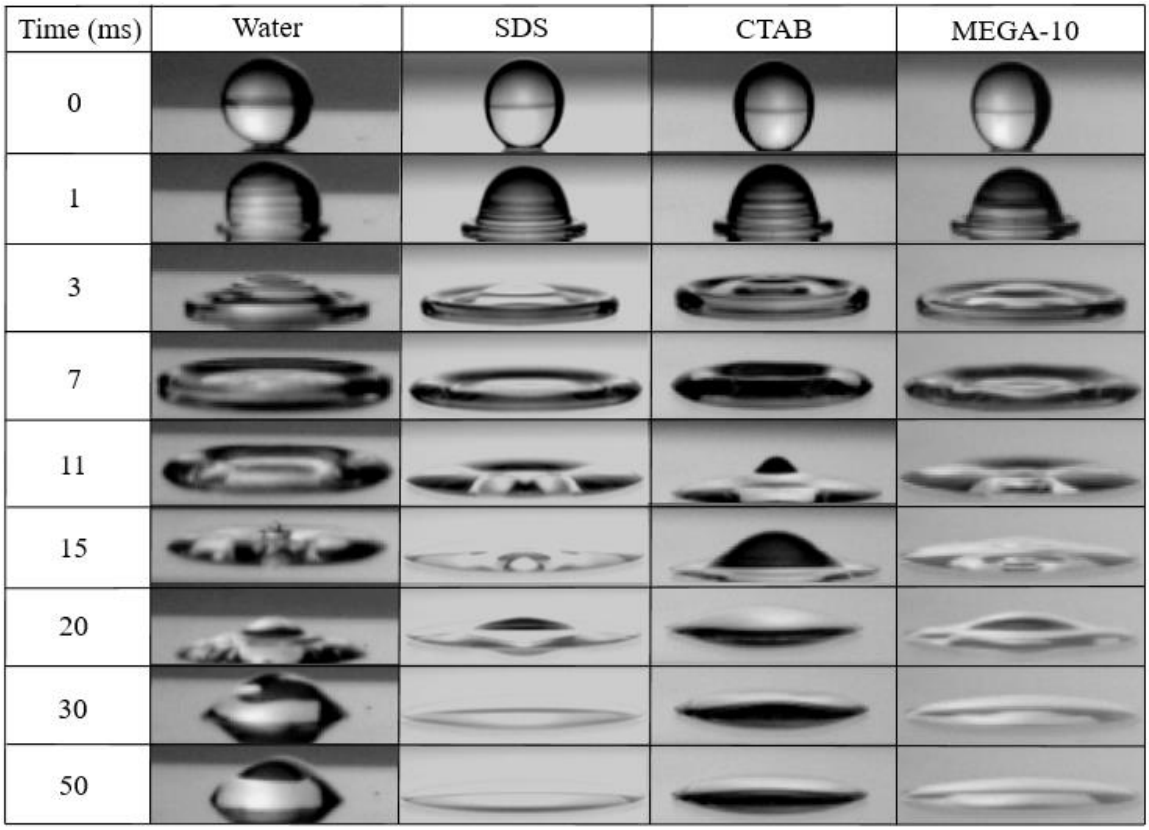

Figure 3.3. Comparison of the droplet evolution of DI water and surfactant-laden droplets, including SDS 8 mM, CTAB 0.9 mM and MEGA-10 7 mM with an equilibrium surface tension in the range of 35.12-37.28 mN/m during the first 50 ms after the impact on the hydrophilic glass slides at *We*=46.07±1.38. The initial diameters of surfactant-laden and DI water droplets are 2.05±0.05 and 4.09 mm, respectively. The scale bar is the same for the entire column.

As can be observed in Figure 3.3, at t = 0 ms, just before the impact (state 1), while the water droplet is spherical, the droplets of other solutions are vertically elongated. The main reason behind this phenomenon may be attributed to the fact that surfactant addition to pure water has reduced its surface tension by weakening the hydrogen bonds among its molecules. Consequently, these droplets having a lower surface tension are not capable of forming a perfect sphere, which can have a remarkable influence on the impact dynamics of the droplets. As soon as the droplets hit

the surface, their wetting area drastically enhances. At this moment, a shoulder region is observed beneath the droplets horizontally advancing on the glass substrates with time. Then, the liquids form a donut-like rim shape with a concave center (t = 7-11 ms) and reach their maximum diameter in a short period of time. So far, the qualitative snapshots have shown that the surfactant addition to DI water has not affected the shape of the droplets during the spreading phase, which is in agreement with other studies [120,122].

Due to the stored surface energy in the droplets, the retraction phase starts after they reach the maximum spreading diameter at state 2 [129]. At this moment, the aqueous surfactant-laden droplets, unlike DI water, do not show a noticeable retraction and only a few weak oscillations are observed, followed by resting on the glass slides after ~30 ms. On the contrary, the wetting diameter of the DI water noticeably decreases; then, the droplet vertically oscillates on the substrate for many cycles. It is evident that the surfactant addition has contributed to a decrease in the vertical oscillations and an increase in the maximum spreading diameter of the impinging droplets on the hydrophilic substrate, which is similar to what reported by the prior studies [122]. It can be concluded that surfactant addition decreases the capillary energy of the droplets in the spreading phase by lowering the liquid surface tension. Consequently, the droplets tend to have a larger wetting area on the substrate, which results in an increase in the energy loss during the spreading phase [130].

The same experiments with the solutions and Weber numbers mentioned above were repeated on the hydrophobic substrate (PTFE), the results of which are displayed in Figure 3.4. It is evident that the aqueous surfactant-laden droplets have reached their maximum spreading diameter in a shorter period of time (~8 ms) compared to that on the glass slides (~11-15 ms, Figure 3.3). Similar to the previous section, surfactant addition to DI water has weakened the vertical oscillations of

the droplets. It is worth mentioning that during the spreading, new surfactant-free interfaces are created with a surface tension close to DI water, which then starts to decrease with time. The reason behind this phenomenon is attributed to the diffusion of the molecules of the surfactants toward the fresh interfaces and their adsorption at those areas, which are governed by the mobility of the molecules [126].

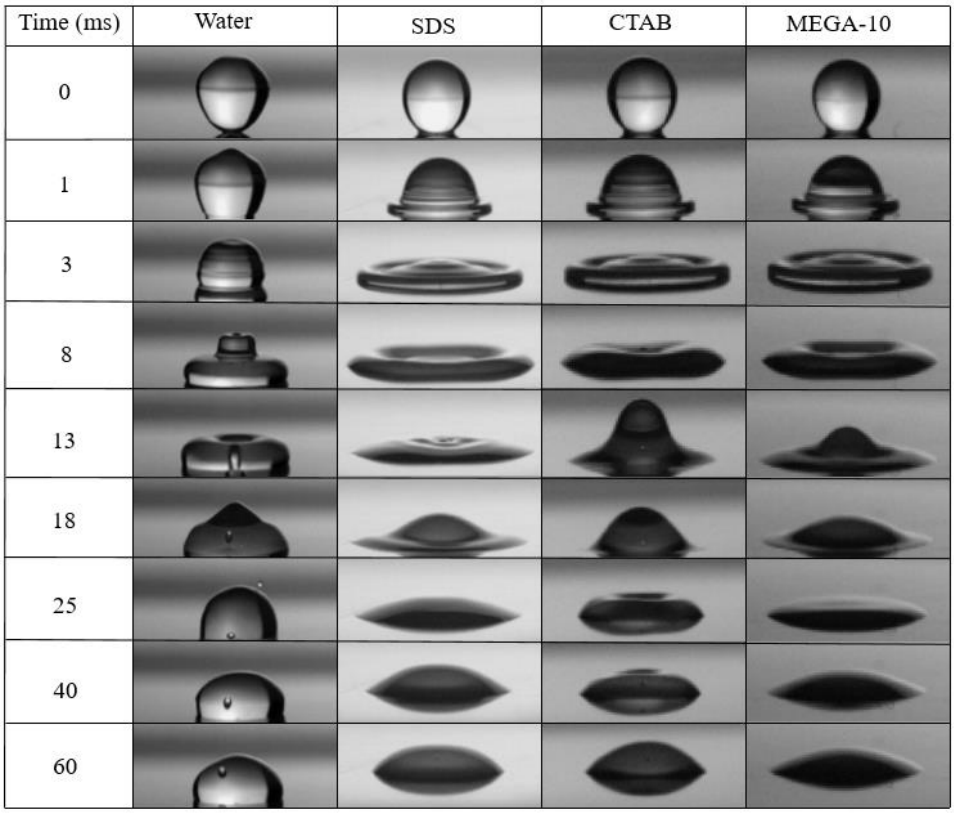

Figure 3.4. Comparison of the droplet evolution of DI water and aqueous surfactant-laden droplets containing 8 mM SDS, 0.9 mM CTAB and 7 mM MEGA-10 with an equilibrium surface tension in the range of 35.12-37.28 mN/m during the first 60 ms after impact on the hydrophobic PTFE slides at *We*=46.07±1.38. The initial diameters of surfactant-laden and water droplets are 2.05±0.05 and 4.09 mm, respectively. The scale bar is the same for the entire column.

In the study of Gatne *et al.* [122], the dynamic surface tension of the SDS-laden droplet having a concentration of CMC with respect to the surface age of the droplet was studied. It was shown that at t=0 ms, the surface tension is equal to 71.61 mN/m, which is very close to that of water. Interestingly, as the surface age of the droplet increases and reaches 100 and 1000 ms, the surface tension decreases to 38.59 and 37.95 mN/m, respectively. It can be said that when new interfaces are created on the droplet, it takes time for the added surfactants to reach an equilibrium state. This equilibrium state is between the bulk concentration and the surface concentration in the droplet. It was shown that this time scale is a function of the diffusion rate of the surfactants molecules [122]. In the present study, by comparing the equilibrium time scale of the surfactants, which is between 100 to 1000 ms [122], with the maximum spreading time scale of the solutions on PTFE (~8 ms), it is evident that the droplets do not reach their equilibrium condition during the spreading phase. Consequently, when the droplets reach their maximum diameter at state 2, each solution has a different surface tension based on the diffusion rate of the surfactants. This phenomenon explains why the solutions do not have a similar dynamic behavior in the spreading phase until the state 2 although the initial energy and equilibrium surface tension of all the droplets are the same at the state 1.

By comparing Figures 3.3 and 3.4, it is seen that in both cases, SDS-laden droplets have a weaker oscillation than the other solutions. The difference in the molecular weight of the surfactants can be thought of as the main reason for this phenomenon [122]. Due to the lower molecular weight of SDS in comparison with other surfactants (i.e., CTAB and MEGA-10, see Table 3.1), the repopulation of molecules of the SDS on the outer interface of the droplet is faster than that of others. This means that SDS reaches a lower surface tension than the other two surfactants in a shorter period, resulting in a weaker vertical oscillation. This phenomenon is clearly seen in Figure

4 (t = 13 ms), where droplets containing 0.9 mM CTAB and 7 mM MEGA-10 are elongated vertically and the capillary wave is amplified, while the droplet of 8 mM SDS is fully spread on the substrate. The static contact angle of all the droplets on the PTFE substrate, 100 ms after the impact, was also measured by analyzing the captured videos. The average static angle of all the surfactant-laden droplets is 46.38±6.13°, which is ~43° smaller than that of DI water and confirms that the surfactant addition has increased the wetting area of the DI water 100 ms after the impact.

To further investigate the impact of non-wettability of the substrate on the dynamic behavior of surfactant-laden droplets, another series of experiments with the same solutions were conducted on the superhydrophobic AKD samples at the same Weber number. The snapshots of the evolution of the droplets in the first 55 ms after the impact are shown in Figure 3.5. It is seen that there is no considerable difference in the shape of the droplets in the first 3 ms, where the maximum spreading diameter is observed. However, there are noticeable differences in the retraction phase of the solutions, which need to be studied in-depth.

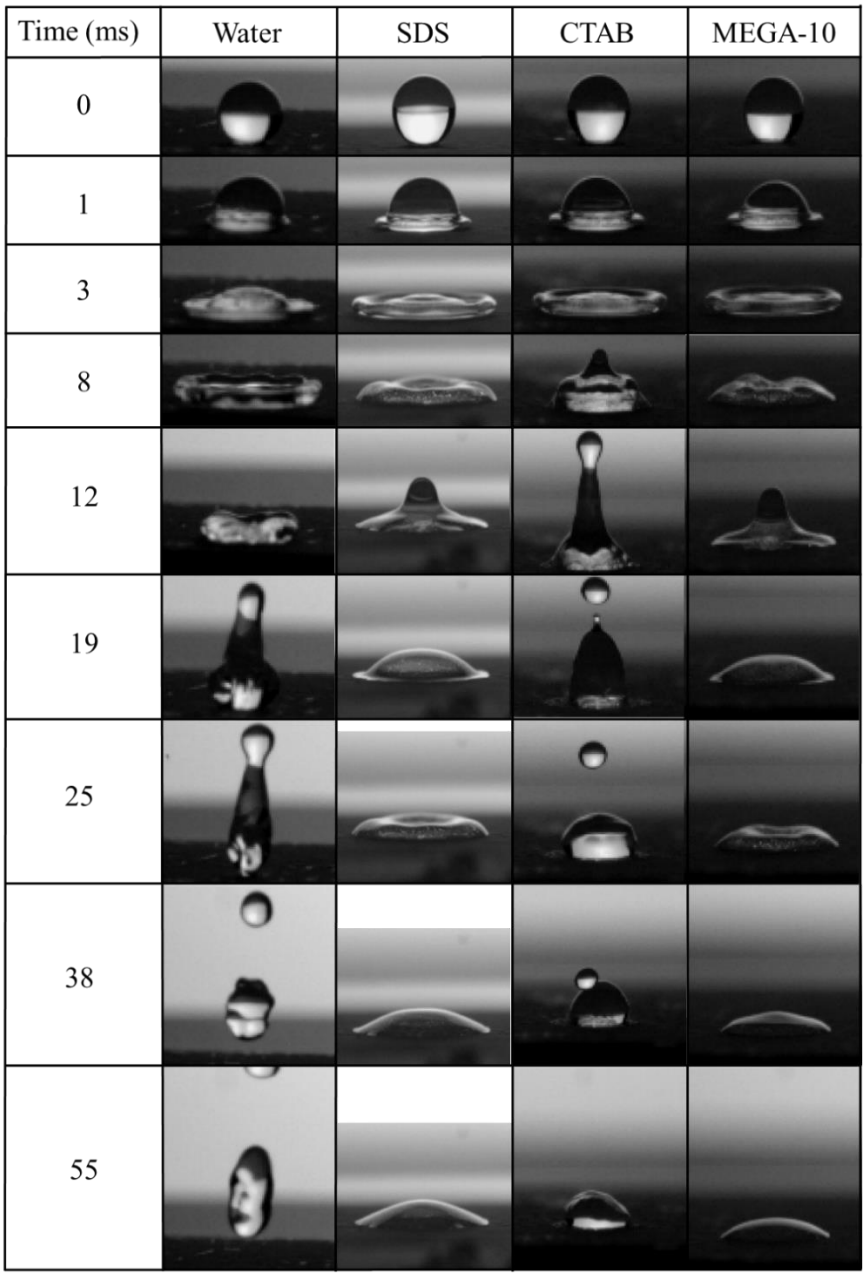

Figure 3.5. Comparison of the droplet evolution of DI water and aqueous surfactant-laden droplets containing 8 mM SDS, 0.9 mM CTAB and 7 mM MEGA-10 with an equilibrium surface tension in the range of 35.12-37.28 mN/m during the first 55 ms after impact on the superhydrophobic AKD substrates at *We*=46.07±1.38. The initial diameters of surfactant-laden and water droplets are 2.05±0.05 and 4.09 mm, respectively. The scale bar is the same for the entire column.

As observed at t = 12 ms, droplets containing 8 mM SDS and 7 mM MEGA-10 slightly deposit on the substrate and do not show considerable oscillation. However, the CTAB-laden droplet is fully elongated in an unstable condition and trying to rebound. It is seen that at t = 19 ms, while the main droplet deposits on the surface and has a vertical oscillation, a small one is ejected from it, which later coalesces with the big one, forming a single droplet (t = 38 ms). In the case of DI water, at t = 8 ms, the droplet drastically recedes after reaching its maximum spreading diameter. Moreover, at t = 25 ms, the water droplet is in an unstable condition, followed by the ejection of a small droplet from the main one after a few milliseconds. It should be noted that unlike the solutions, a complete rebound is observed for the water droplet at t = 38 ms.

When we compare the spreading and retraction of CTAB and MEGA-10 (c = CMC) with a similar equilibrium surface tension and initial kinetic and capillary energies (state 1) as well as the comparable molecular weights (364.5 and 349.5 g/mol, respectively), it is seen that their dynamic behavior is not the same during the retraction phase. This phenomenon clearly reveals that besides the molecular weight, the ionic nature of the surfactants has a remarkable influence on the impact dynamics of the surfactant-laden droplets.

It is to be noted that the chemical structure of the surfactants includes a polar hydrophilic head group with high interaction with water and a non-polar hydrophobic tail. When the surfactants are dissolved in water, their non-polar tails are exposed to air and orientated at the free air/water interface. In terms of the polar head of the surfactants, cationic, anionic and non-ionic surfactants carry positive, negative and neutral charges, respectively. It is well documented that the zeta potential of all the substrates in the current work is negative [102,131,132]. Consequently, in the analysis of the impact dynamics of surfactant-laden droplets, the interaction of the surfactants polar heads with negatively charged sites on the substrates must be taken into account.

As such, when the impact dynamics of cationic CTAB and non-ionic MEGA-10 on AKD (Figure 3.5) are compared, it can be said that during the spreading and retraction phases, the positive charges on the air/water interface of the CTAB-laden droplet are able to bind with the negatively charged sites of the substrate. This leads to exposure of the hydrophobic tails of the solution toward air, which improves the non-wettability of the surface. This phenomenon explains the reason why the dynamic behavior of the droplet containing 0.9 mM CTAB 0.9 solution with the highest molecular weight compared to the other solutions and a positively charged polar head is close to that of DI water.

By comparing Figures 3.3, 3.4 and 3.5, it is evident that regardless of the wetting properties of the substrates as well as ionic nature and molecular weight of the solutions, surfactant addition enhances the wetting area and weakens the vertical oscillation of DI water. In addition, as the spreading time on the hydrophobic and superhydrophobic substrates decreases, the influence of the molecular weight and ionic nature of the surfactants are less noticeable in this phase. However, the retraction phase is obviously influenced by these parameters.

To obtain a clear idea of the influence of each parameter on the impact dynamics, we conducted a series of systematic experiments on all four groups of the solutions (Table 3.3), by varying the impact velocity and Weber number in the range of 0.4-2.4 m/s and ~6-353, respectively. Then, all the videos were quantitatively analyzed with a commercial image-processing software (Tracker 5.1.5) in order to extract the maximum spreading diameter, maximum flattening factor and impact outcomes of each case.

First, we varied the impact velocity of each droplet at a fixed initial diameter (2.05±0.05 mm) and concentration, the results of which are given in Tables A3-5. It is seen that at a constant concentration, as the Weber number increases, the maximum spreading factor also increases in all

cases, which is well aligned with prior studies [122]. Moreover, as expected, the maximum spreading diameter of droplets is the highest for the hydrophilic substrates compared to the other two. Our results also reveal that although increasing the concentration of the solutions might enhance the chance of the molecules to repopulate on the new interfaces, this phenomenon has not contributed to an increase in the maximum spreading diameter.

Figure 3.6a shows the maximum spreading diameter of DI water and surfactant-laden droplets with different concentrations on the glass substrates with respect to the Weber number. As can be seen, all data points of each solution, irrespective of their concentration, follow a power law. Next, a power regression was fitted on each series, including DI water and solutions of SDS, CTAB and MEGA-10. It is indicated that the maximum spreading factor of the aqueous surfactant-laden droplets is proportional to ~$We^{0.21}$, $We^{0.24}$ and $We^{0.21}$, for SDS, CTAB and MEGA-10, respectively.

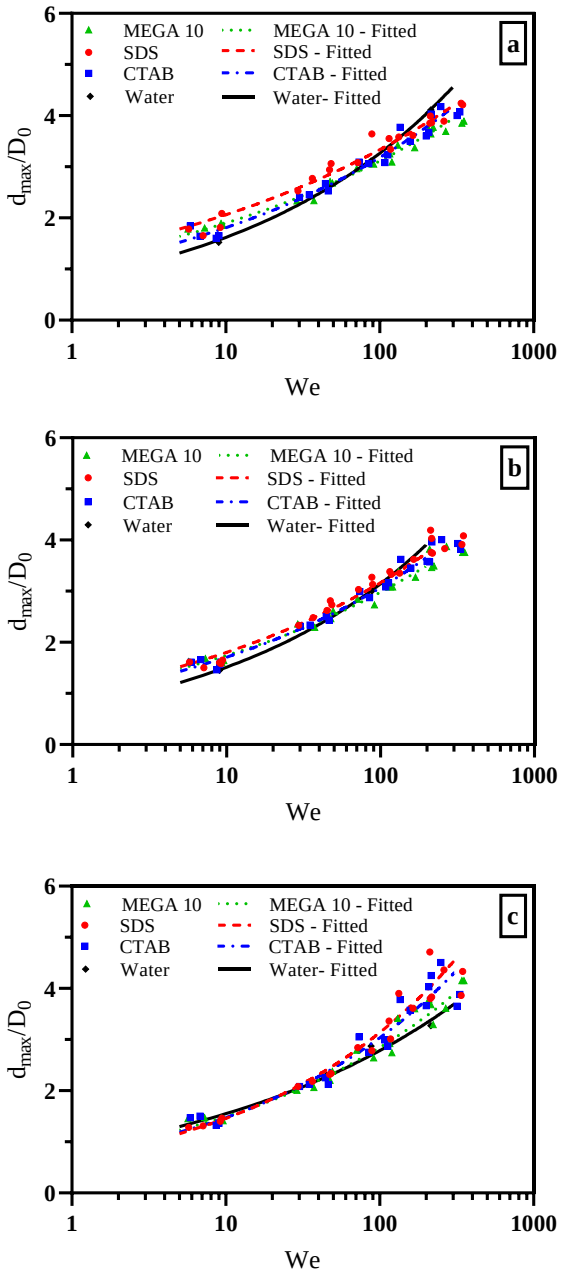

Figure 3.6. Maximum spreading factor of DI water and surfactant-laden droplets on (a) glass, (b) PTFE and (c) AKD substrates with respect to the Weber number.

Although all the solutions are almost similarly sensitive to a change in the Weber number with an average power of 0.22±0.01, SDS-laden droplets have the largest maximum spreading diameter

with a prefactor of 1.27 compared to 1.02 and 1.15 for CTAB and MEGA-10, respectively. These results confirm our observations in the previous sections, where the spreading diameter of SDS-laden droplets was greater than that of the other solutions at c = CMC, suggesting that the prefactor of this power law is a function of both molecular weight and ionic nature of the surfactants.

Figure 3.6b shows the maximum spreading factor of all the surfactant solutions on the PTFE substrates regardless of their concentration, with respect to the Weber number only. Based on the results, it is seen that the surfactant addition has contributed to an increase in the maximum spreading diameter of the droplets compared to the DI water, especially for We<100. In addition, by comparing the results of Figure 3.6a and b, it is seen that when the spreading time decreases by using the PTFE substrate instead of the hydrophilic glass slides, the influence of molecular weight and ionic nature of the surfactants are less noticeable. This might be attributed to the fact that with a shorter contact time during the spreading phase, the surfactants do not have enough time to reach their equilibrium state. The maximum spreading diameter of SDS, CTAB and MEGA-10 solutions is proportional to $\sim We^{0.24}$, $We^{0.25}$ and $We^{0.23}$ with a prefactor of 1.03, 0.95 and 1.02, respectively.

Next, we measured the maximum spreading factor of the droplets on the superhydrophobic AKD substrates (Figure 3.6c). It is observed that at low Weber numbers, surfactant addition has not enhanced the maximum spreading diameter of the droplets. According to the results, for We<100, the data points collapse onto a master curve ($0.74We^{0.30}$), which confirms our previous observations regarding the surface characteristics. We hypothesize that the difference in the results for $\sim We$>100 might be due to the splashing phenomenon that results in an asymmetric spreading and must be investigated further.

By comparing Figure 3.6a, b and c, it is concluded that the surfactant addition becomes more effective as the spreading contact time increases. This means that by improving the non-wettability

of the substrates, the influence of the studied parameters becomes less noticeable to the point that in the case of superhydrophobic AKD, all the data points align on a master curve. Also, by surfactant addition to DI water, the maximum spreading diameter of the droplets, similar to pure liquids [118], follows a power law, in which the prefactor is a function of the molecular weight and ionic nature of the surfactant and non-wettability of the surface.

According to Figures 3.3-3.5, it is obvious that during the retraction phase, the droplet oscillates on the substrate for a certain period of time. Using a single-degree-of-freedom oscillating model consisting of a mass, spring and damper is common in modeling the oscillation of small droplets on the substrates [31,32,133]. Based on the oscillation theory [134], the energy dissipation of the oscillating system can be determined via the damping coefficient. Consequently, to investigate the influence of the molecular weight, concentration and ionic nature of the surfactants on the energy dissipation during the retraction phase, we measured the maximum flattening factor of each case as a representative of the damping coefficient of the system. Since no noticeable elongation is seen for the droplet impact on the hydrophilic and hydrophobic substrates, this section is devoted to the droplet impact on the superhydrophobic AKD substrates only.

Figure 3.7 shows the maximum flattening of the droplets on AKD with respect to the concentration and type of the surfactant as well as the Weber number. Based on Figure 3.7a for the results of the SDS-laden droplets, it is evident that the vertical oscillation markedly decreases with an increase in the SDS concentration. The closest retraction behavior among the SDS solutions to DI water belongs to the one having a concentration and equilibrium surface tension of 2 mM and 56.19±1.54 mN/m, respectively. In both cases (DI water and SDS solution), the maximum flattening factor increases with an increase in the Weber number up to ~100. Then, by increasing the Weber number, while the maximum flattening factor of the droplets containing 2 mM SDS solution

drastically decreases from 2.88 to 1.56, that of DI water reaches 1.99 with a slightly decreasing slope.

Moreover, by increasing the SDS concentration to 4, 8 and 16 mM, this decreasing trend continues to the point that for the last two concentrations, which are equivalent to CMC and 2×CMC, the maximum flattening factor of the droplets is approximately equal to 1 in all Weber numbers. Figure 3.7a clearly shows the significant role of concentration on the retraction phase. We hypothesize that as the concentration increases, the surfactant molecules are more widely distributed in the liquid droplet, which results in a remarkable increase in the energy dissipation of the oscillating system due to having a more powerful damper.

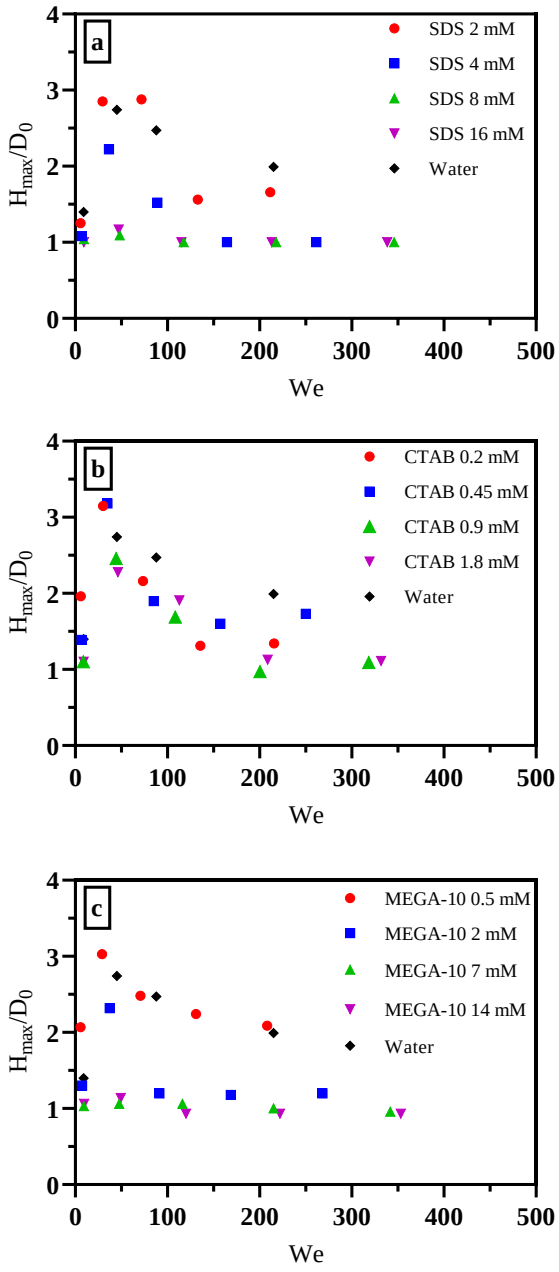

Figure 3.7. Comparison of the maximum flattening factor of DI water and surfactant-laden droplets containing (a) SDS, (b) CTAB and (c) MEGA-10 on the superhydrophobic AKD substrates with respect to the concentration (~0.2 to 2×CMC).

The results for the maximum flattening factor of the CTAB-laden droplets (Figure 3.7b) reveal that the retraction dynamic of this solution, compared to the SDS (Figure 3.7a), is less sensitive to the concentration. This means that even at high concentrations (CMC and 2×CMC), the impinging droplet is able to experience the vertical elongation. Moreover, similar to the previous section, the maximum flattening factor decreases with an increase in the concentration.

The same analysis was repeated for the droplets containing MEGA-10 (Figure 3.7c). It is seen that for the first two concentrations (0.5 and 2 mM), the corresponding droplets have an almost similar dynamic behavior as CTAB-laden droplets with the same equilibrium surface tension (groups 1 and 2). However, when the concentration increases to 7 mM (CMC) and 14 mM (2×CMC), the droplets fully deposit on the substrate and no vertical elongation is observed.

By comparing Figure 3.7a, b and c, it is apparent that the molecular weight of surfactants plays a crucial role in the retraction of the droplets. As can be seen, although the maximum flattening factor of all the surfactant-laden droplets has decreased with concentration, the addition of SDS with the lowest molecular weight (288.4 g/mol) compared to MEGA-10 and CTAB with a molecular weight of 364.50 and 349.46 g/mol, respectively, has more contribution in this decreasing trend.

Moreover, the role of the ionic nature of surfactants on their retraction is more noticeable at $c \geq$ CMC (Figure 3.7b and c). This might be attributed to the fact that at higher concentrations, for cationic surfactants, more surfactant molecules with positively charged heads are available at the droplet surface, which are readily accessible to attract to the negatively charged surface of AKD, resulting in an improvement in the non-wettability of the substrate. The higher numbers of cationic charges on the droplet surface can possibly overcome the hydrophobic force created by the tails of the air-exposed surfactants, which are detached from the droplet and are sitting on the substrate.

This phenomenon explains the reason why at c = CMC, the dynamic behavior of CTAB (cationic) is more similar to DI water compared to MEGA-10 (non-ionic).

To study the impact outcomes of the droplets on the superhydrophobic AKD substrates, the videos were analyzed and similar to the previous studies on pure liquids [124,135–138], complete rebound, deposition, partial rebound and splashing were identified by an increase in the impact velocity, the results of which are shown in Figure 3.8.

The complete rebound of an impinging droplet is one of the remarkable characteristics of the superhydrophobic substrates due to their low energy and presence of micro/nano patterns on their surface, acting similar to air cushions [12,25]. The complete rebound happens when the kinetic energy of the impinging droplet is sufficient enough to overcome the energy dissipated during the impact. If the impact velocity of the impinging droplet is not sufficiently high, the droplets deposit on the surface and form a pearl-like shape [139]. Note that for solutions having a viscosity close to the DI water, mainly pinning/depinning of the contact line hinders the droplets rebound.

Based on the results (Figure 3.8), for DI water, a complete rebound is observed at $We \sim 9$, which aligns well with the threshold of approximately $0.3 < We < 20$ for a complete rebound defined in previous reports [139]. Furthermore, it is observed that the surfactant addition has reduced the upper limit threshold of the complete rebound from $We \sim 20$ to 7. The smaller threshold of a complete rebound for the aqueous surfactant-laden droplets might be attributed to the damping behavior of the surfactants that enhances the pinning effect and energy loss in the retraction phase.

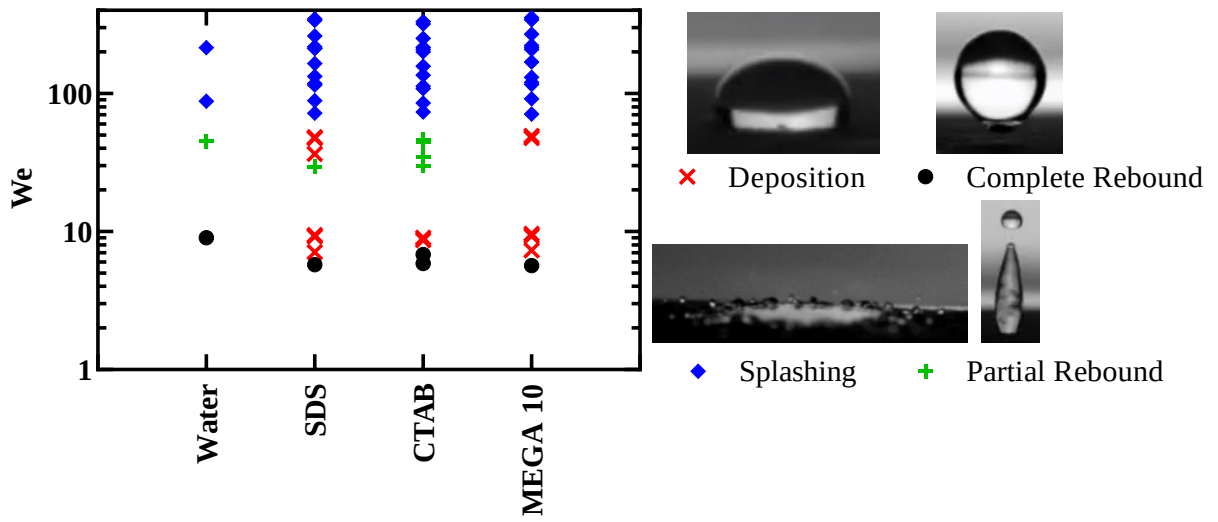

Figure 3.8. Impact outcomes of the DI water and surfactant-laden droplets on the superhydrophobic AKD substrates.

When the impact velocity of pure liquids is higher than the threshold, they cannot get depinned from the superhydrophobic substrate; consequently, no complete rebound will be observed. It is reported for the DI water droplet having a *We*<59 that due to its high Weber number, the droplet is vertically elongated, in an unstable thermodynamic condition. At this moment, the elongated droplet minimizes its free energy, known as the Rayleigh-Plateau instability [140]. In this range of Weber numbers, instead of a complete rebound, a partial rebound is observed. The recoiling phase of a partial rebound is accompanied by two droplets: (1) the main droplet which pins on the surface and (2) the smaller droplet, which detaches from the initial one (Figure 3.8). Compared to the DI water, aqueous surfactant-laden droplets have a smaller threshold for a partial rebound due to their higher energy loss in the retraction phase.

By comparing the impact outcomes of all the droplets, it is seen that the CTAB-laden droplets show almost a similar dynamic behavior to that of the DI water. We hypothesize that the main

reason behind this phenomenon is the high molecular weight and cationic nature of the CTAB solutions discussed earlier. In the other cases (SDS and MEGA-10), there is no such interaction likely due to their different ionic natures.

By further increasing the Weber number, it is seen that several small droplets form at the rim of the impinging droplet on the surface, known as splashing [5,46,108,141]. Based on the previous studies, this phenomenon can be described by a dimensionless number, $K=We^{0.50}\,Re^{0.25}$, where *Re* is the Reynolds number ($Re = \rho V D_0/\mu$). One of the major shortcomings of this method is that it is not able to consider all the physical aspects affecting the splashing (e.g., the ambient pressure) [142]. However, in the present study, the experiments were conducted at atmospheric pressure and this dimensionless number can be used to describe this phenomenon [46]. Our results show that when the DI water droplet, having a Weber number of ~88, reaches the maximum spreading diameter, several smaller droplets are formed on its periphery, which resembles the splashing. Existing literature has introduced a threshold of $We \gtrsim 59$ for splashing of the DI water droplets confirming that our results are well fitted in this range [143]. A few milliseconds after the formation of those small droplets, they coalesce and result in a partial asymmetric rebound. For all aqueous surfactant-laden droplets, the splashing occurs at $We \gtrsim 70$, corresponding to $K \gtrsim 63$, which is almost similar to what is obtained for DI water droplets. This shows that the splashing is mainly a function of the initial kinetic energy rather than the surface tension of the liquid. As a result, to control the impact dynamics of the droplets, especially in the applications that the probability of environmental pollution is high, it is indispensable to primarily control the initial kinetic energy.

3.4 Conclusions

We comprehensively investigated the influence of surfactant addition with different ionic natures and molecular weights on the impact dynamics of DI water droplets. To achieve this goal, three impact surfaces (hydrophilic, hydrophobic and superhydrophobic) were used and the experiments were conducted at Weber numbers ranging from ~6-353. Our results revealed that the efficiency of the surfactant additions in enhancing the maximum spreading diameter is proportional to the surface non-wettability. As the impact surface becomes more hydrophobic, the influence of the surfactant addition becomes less noticeable. Furthermore, the maximum flattening factor analysis of the impinging droplets on the superhydrophobic substrates showed the significant role of the molecular weight, concentration and ionic nature of the surfactants in the retraction dynamic. As the molecular weight or concentration increases, the damping ability of the oscillating system significantly improves, which results in a greater energy dissipation. On the other hand, by binding to the negatively charged sites of the substrate, positive charges of the cationic solutions make the impact dynamics more similar to DI water. Finally, it was shown that surfactant addition does not noticeably change the splashing behavior of the droplets. According to our results, splashing is mainly a function of the initial kinetic energy of the impinging droplets before the impact. Thus, it is essential to control their initial kinetic energy to prevent this phenomenon, mainly when droplets cause environmental pollution (e.g., pesticides, detergents, etc.) due to the undesired bouncing. Controlling the size and initial velocity of the impinging droplets are two common methods to address this issue.

Chapter 4. Impact Dynamics and Freezing Behavior of Surfactant-Laden Droplets on Non-Wettable Coatings at Subzero Temperatures

4.1 Introduction

In the past decade, icephobic coatings have found broad applications in high-tech industrial fields, including powerlines [18], wind turbines [19], aircrafts [20] and heat exchangers [21]. The focus of studies in this field can be divided into several main categories, including surface chemistry and morphology of icephobic coatings [52,144,145], ice nucleation and adhesion of sessile droplets [146,147], droplet impact [148–151] and fabrication of superhydrophobic coatings as a passive method for anti-icing [16,26,152].

Extensive studies have been conducted on the impact dynamics of water droplets on superhydrophobic surfaces at freezing temperatures [153,154]. In one of the recent reports, Maitra *et al.* investigated the influence of viscosity on the impact of supercooled water droplets on non-wettable coatings at –17 °C. They showed that at freezing temperatures, higher viscosity results in a smaller spreading diameter, a larger wetting area and a slower retraction velocity compared to the same parameters obtained at room temperature [148]. In another study, Mishchenko *et al.* presented an experimental and theoretical investigation of water droplet dynamics at freezing temperatures. They investigated a broad range of parameters influencing the impact dynamics to analyze how supercooling alters the wetting properties of hydrophilic, hydrophobic and superhydrophobic substrates. According to their results, due to the unique properties of highly-ordered superhydrophobic surfaces, the ice formation was prevented above the transition temperature of ~ –25 to –30 °C [20].

Additives in water result in significant changes in its properties (i.e., surface tension, density, viscosity, etc.) Not only have these changes remarkable effects on the dynamic behavior of the

droplets at freezing temperatures, but they might also alter the chemistry and morphology of the substrates. Based on the previous studies, due to the stretching of molecules, addition of flexible polymers similar to poly(ethylene oxide) to water results in a significant increase in energy dissipation. This phenomenon improves the stability of the surface of the droplets and suppresses the scattering of secondary droplets from the liquid [155]. Moreover, Carpenter *et al.* studied the effect of surface chemistry on ice nucleation of saltwater at subzero temperatures as low as –40 °C. They used two sodium chloride solutions with different concentrations to represent the salinity of seawater and briny water. It was shown that salt addition improves the bouncing of the water droplets and also delays the ice nucleation [156]. Additionally, Emelyanenko *et al.* [157] studied the ice nucleation kinetics of the droplets of alkali metal chlorides deposited on a superhydrophobic coating. They observed an extraordinary freezing delay for droplets containing additives due to their higher energetic barrier compared to deionized water for the ice nucleation.

Surfactants, which are commonly used as additives, lubricants and cleaning agents in numerous industrial processes [158,159], can influence the dynamic behavior of water and the wettability of the substrates. It is well documented that surfactants solutions have a time-dependent surface tension at room temperature, significantly affecting their spreading, retraction and impact outcomes [118,120,122,160]. For example, it has been shown that sodium dodecyl sulfate solutions enhance the heat transfer efficiency in spray cooling processes by promoting foaming in the droplets [161]. However, to the best of our knowledge, the dynamics and freezing behavior of surfactants solutions at subzero temperatures have not been studied. Understanding this behavior is crucial since surfactants could be used in some applications where surfaces are essential to avoid ice formation. Some examples are solar panels, wind turbines, heat pumps and power lines. For instance, some studies suggest that application of surfactants for cleaning the photovoltaic panels

could retain their solar conversion efficiency over time [34,35]. In another report, a surfactant added nanofluid was suggested for improving the thermal performance of wickless heat pipe solar collectors [36]. Therefore, as surfactants and other similar fluids are becoming part of the many subzero applications [162], it is important to study their dynamic behavior on superhydrophobic surfaces at freezing temperatures.

The present work aims at investigating the dynamic behavior and freezing of surfactant-laden droplets impacting a superhydrophobic coating at the temperatures range of –10 to –30 °C. To achieve this goal, a series of systematic experiments were devised to understand the role of concentration, molecular weight and ionic nature of the surfactants on the spreading, retraction, freezing time and ice buildup growth rate of the droplets. We used three surfactants of different ionic nature, anionic, cationic and non-ionic, with concentrations ranging from 0 to 2 times of their critical micelle concentration (CMC). We believe that our results can contribute to a better understanding of the dynamic behavior of aqueous solutions at low temperatures to control and manipulate the impact dynamics and freezing behavior of droplets.

4.2 Experimental Procedure

Figure 4.1 shows the experimental apparatus of this study. To conduct the experiments at subzero temperatures of –10 to –30 °C with –10 °C increments, a medical upright freezer (VLT650, Accucold, USA) was used. To capture the front view of the impacting/freezing droplets, its door was replaced with a 50 mm thick insulating polystyrene foam, in which a 150 × 150 mm viewing window of polished acrylic plate was embedded. A 20 cm cylindrical stage made of plastics was used as the sample holder. This freezer was equipped with an infrared thermal sensor (TMP007, Texas Instruments, USA) aimed at the substrate within 2 cm. Also, a DHT22 digital temperature

and humidity sensor was placed next to the substrate to ensure that its temperature remains equal to that of the environment.

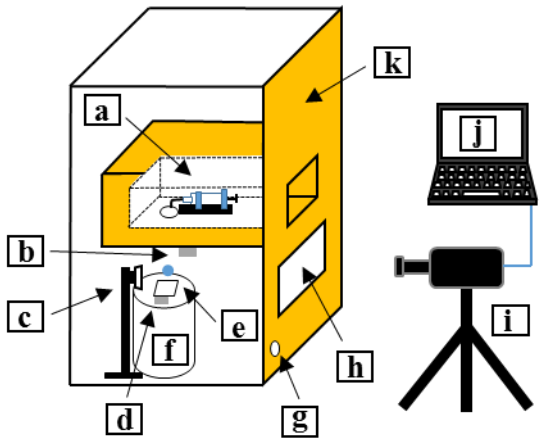

Figure 4.1. Schematic of the experimental apparatus. The components of the experimental apparatus include: (a) droplet generator, (b) infrared thermal sensor, (c) light source, (d) humidity and temperature sensor, (e) substrate, (f) stage, (g) argon supply entry, (h) viewing window, (i) high-speed camera, (j) PC and (k) insulating door.

Since the icephobicity of superhydrophobic coatings could be compromised by formation of a plausible frost layer on their surface, the relative humidity of the freezer atmosphere was kept under 15% by flowing high-purity argon (Airgas, USA) to the freezer prior to conducting each experiment (Figure 4.1). A syringe, equipped with a nonstick needle for droplet generation, was mounted on the insulating door of the freezer. Due to the significant difference in surface tension of the solutions compared to water, three needles with diameters of 0.008, 0.013 and 0.023 in. were used to generate droplets with a diameter of 2.05±0.05 mm. It is to be noted that each needle was rinsed with deionized water (resistivity = 18.2 MΩ.cm, from Milli-Q, Millipore, USA) and dried with compressed room-temperature air prior to conducting each experiment. According to $V = \sqrt{2gh}$, where V is impact velocity and g and h are the gravitational constant (9.81 m/s^2) and

release height, respectively, we designed the experimental apparatus to have a release height of 60 mm. Consequently, the impact velocity of all the conducted experiments was 1.08 m/s.

A high-speed camera (MicroLab 340, Phantom, USA) was used to capture the impact dynamics of the impinging droplets and their consequent freezing at 5000 frames per second (fps). The high-speed camera was aligned at 0° with respect to the sample for capturing the frontal shape evolution of the droplets. In order to avoid any heat generation or vibration produced by powerful light sources during the experiments, only three rows of 24 volts led strips were used as the light source. Since the light source was controllable from outside of the freezer, to minimize any effects on the environment temperature, it was turned on only a second before the droplet release.

The next step was to obtain the critical parameters related to the spreading, retraction and freezing of the droplets. The captured videos were cut into two parts of impact dynamics and freezing. These two parts were analyzed using Tracker 5.1.5 and Phantom Camera Control (PCC 3.5) image-processing software, respectively. It is to be noted that the measurements done using the high-speed camera were repeated three to five times for each experiment and the average and standard deviations are reported. We used superhydrophobic alkyl ketene dimer (AKD) as the impact substrates. To fabricate these coatings, first, we melted the AKD pellets (Solenis, USA) on a hot plate at 70 °C. Then, a glass slide (AmScope, USA) was dipped in the molten AKD for a few seconds. The freshly solidified AKD was cured over 4-6 days in a desiccator at room temperature to become superhydrophobic. The advancing and receding contact angles of the fabricated substrates with deionized water were measured using a goniometer (DSA25E, Krüss, Germany), at least at 5 randomly-chosen spots, which were equal to 158.6±0.84 and 152.7±0.64°, respectively. To ensure that the surface chemistry of the substrates does not change due to the droplet impact, a freshly produced superhydrophobic sample was used in each experiment. More

details regarding surface characterization of the samples used in the current work, including the surface free energy, roughness and morphology, can be found in our recent comprehensive studies on non-wettable AKD coatings [12,160,163].

To study the influence of concentration, molecular weight and ionic nature of surfactants on the impact dynamics and freezing behavior of the solutions, three well-known surfactants, sodium dodecyl sulfate (SDS, anionic), hexadecyltrimethylammonium bromide (CTAB, cationic) and n-decanoyl-n-methylglucamine (MEGA-10, non-ionic) were used (Sigma-Aldrich, USA). To prepare the solutions, a specific amount of each surfactant was dissolved in deionized water at room temperature to reach the desired concentration. The physicochemical properties, including the chemical formula, ionic nature, molecular weight and CMC as well as the concentrations of the surfactants used in the current work are given in Table 4.1. Then, the equilibrium surface tension values of the solutions were measured at least 5 times using a goniometer (DSA25E, Krüss, Germany) with the pendant drop method. To ensure the accuracy of the results, the instrument was calibrated by measuring the surface tension of deionized water (72.8 mN/m).

Table 4.1. Physicochemical properties and the concentrations of SDS, CTAB and MEGA-10 solutions used in the present study

Surfactant name	SDS	CTAB	MEGA-10
Chemical formula	$C_{12}H_{15}SO_4$	$C_{19}H_{42}BrN$	$C_{17}H_{35}NO_6$
Ionic nature	Anionic	Cationic	Non-ionic
Molecular weight (g/mol)	288.4	364.5	349.5
CMC (mM)	7–10	0.92	6–7
Concentration (mM)	4	0.45	2
	8	0.9	7
	16	1.8	14

To quantitatively analyze the dynamic behavior of water droplets and solutions, three dimensionless parameters of maximum spreading factor (d_{max}/d_0), retraction ratio (d_{final}/d_{max}) and dimensionless final wetting diameter (d_{final}/d_0, hereafter called relaxing diameter) were extracted from the high-speed frames. Note that d_0, d_{max} and d_{final} are the initial, the maximum (at the end of the spreading phase) and the final (at the end of the retraction phase) diameters of the droplets, respectively.

4.3 Results and Discussion

4.3.1 Equilibrium Surface Tension

According to the literature, the gas-liquid interfacial tension mainly depends on the concentration of the solutions when surfactants are present [122]. Thus, it is essential to study the role of concentration on the impact and freezing dynamics of surfactant-laden droplets. Figure 4.2 shows the equilibrium surface tension of the solutions with respect to the type and concentration of the surfactants. The concentrations of SDS, CTAB and MEGA-10 solutions altered in the range of 4–16, 0.45–1.8 and 2–14 mM, respectively, equivalent to ca. 0.5×CMC to 2×CMC. As it is observed, at low concentrations, the equilibrium surface tension of all the solutions is equal to ~44.73±0.51 mN/m. In all cases, as the concentration increases to CMC, the equilibrium surface tension markedly drops and reaches the minimum of ~34–35 mN/m. At this point, by increasing the concentration of the solutions further to 2×CMC, no notable change is observed in the surface tension values, which is in agreement with the previous studies on these solutions [160,164]. This phenomenon is interpreted as the formation of micellar bilayers on the surface, which prohibits any further changes in the surface tension of the solutions with increase in the concentration [165,166].

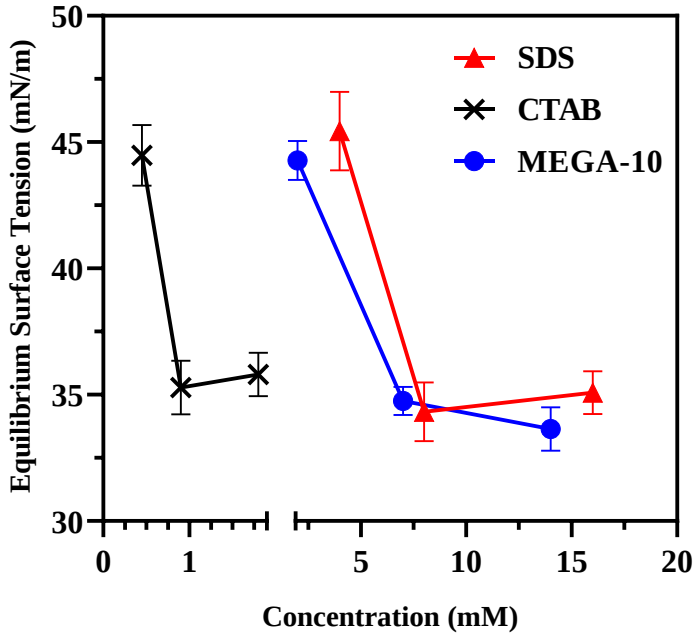

Figure 4.2. Equilibrium surface tension of the SDS, CTAB and MEGA-10 solutions with respect to their concentration.

Based on the data of Figure 4.2, we divided the solutions into three groups with each having an almost similar equilibrium surface tension to separately study the influence of molecular weight and ionic nature of the surfactants on the droplet dynamics at subzero temperatures. The first group includes 4 mM SDS, 0.45 mM CTAB and 2 mM MEGA-10 surfactants solutions with an average equilibrium surface tension of 45.44±1.56, 44.47±1.20 and 44.27±0.78 mN/m, respectively. The second and third groups include SDS, CTAB and MEGA-10 at CMC and 2×CMC with an average equilibrium surface tension of ~34–35 mN/m. It has previously been shown that the viscosity and density of surfactants solutions are slightly different from those of water and are negligible compared to the remarkable changes in the time-dependent surface tension [122,127]. Hence, the Weber number ($\rho V^2 d_0/\gamma$), which is a function of density (ρ), impact velocity (V), initial diameter (d_0) and surface tension (γ) of the droplets was in the range of 53–71 for the solutions and ~33 for

the water droplets having the same impact velocity and density of 1.08 m/s and 997 kg/m^3, respectively.

4.3.2 Impact Dynamics of Droplets

In this section, we study the influence of concentration, molecular weight and ionic nature of the surfactants in the solutions on the impact dynamics of the droplets at freezing temperatures of –10, –20 and –30 °C and compare our results with the dynamic behavior of water droplets. For example, Figure 4.3 presents the results of the first 45 milliseconds (ms) of water as well as 4 mM SDS, 0.45 mM CTAB and 2 mM MEGA-10 solutions with the same equilibrium surface tension of 44.73±0.51 mN/m after impacting the superhydrophobic coatings at –20 °C. Generally, due to the conservation of energy during the impact, the total energy of the droplets at state 1 (just before the impact), including the initial kinetic and capillary energies, transform to the capillary energy at state 2, where the droplets have reached their maximum diameter (~t = 3–5 ms). Then, the equilibrium of the stored capillary energy (at the end of the spreading phase) and the dissipated energy during the spreading determine the ability of the droplets to retract [128].

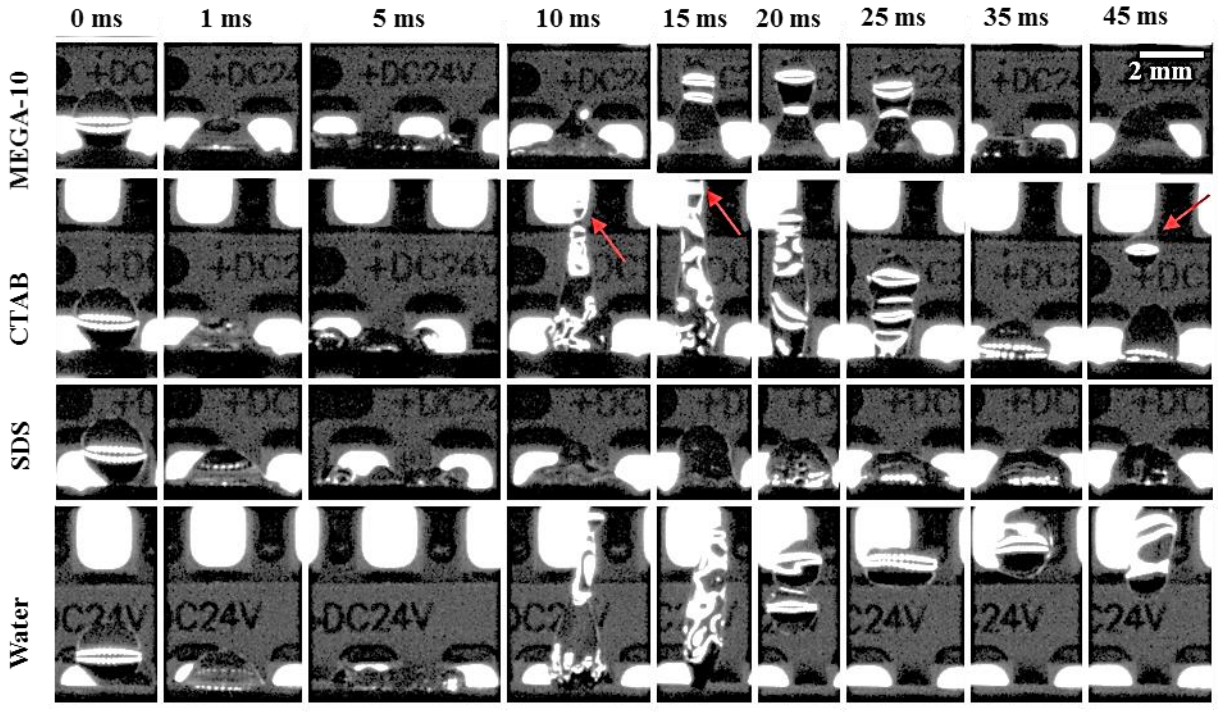

Figure 4.3. High-speed frames of the impact dynamics of water droplets as well as the droplets of surfactants solutions on the superhydrophobic AKD at –20 ºC. The solutions used in this experiment include 4 mM SDS, 0.45 mM CTAB and 2 mM MEGA-10 with an equilibrium surface tension of 44.73±0.51 mN/m. The impact velocity was 1.08 m/s. The scale bar is the same for all the frames.

By a close look at Figure 4.3, it is observed that the water droplet slightly spreads as soon as it hits the superhydrophobic substrate and forms a cap-shaped droplet at t = 1 ms. After a few milliseconds, it is seen that the droplet has fully spread on the substrate and reached its maximum diameter. At this point, the water droplet expeditiously recedes, shortens its wetting diameter and reaches its maximum vertical height in less than 5 ms. Next, by overcoming the dissipated energy during the impact, a complete rebound is observed for the elongated water droplet at a Weber number of ~33, which is in agreement with previous studies [143].

When we compare the dynamic behavior of water droplets with the surfactants solutions in Figure 3, it is seen that in all the cases, the surfactant-laden droplets with an equilibrium surface tension of 44.73±0.51 mN/m have an almost similar spreading behavior to water droplets in the first 5 ms. However, more quantitative analysis needs to be performed to clearly elucidate the influence of high concentration (CMC and 2×CMC) on the spreading phase of the solutions. On the other hand, in the retraction phase (t > 5 ms), while the water droplet is fully elongated (t = 10 ms), the SDS solution is not experiencing any vertical oscillations. Meanwhile, MEGA-10 and CTAB solutions show a more similar dynamic behavior to that of pure water by having an elongation perpendicular to the substrate. In terms of the impact outcomes, while SDS and MEGA-10 solutions completely deposit on the substrates (t = 15-45 ms), CTAB solution experiences a partial rebound, in which a secondary droplet ejects from the liquid (pointed by red arrows in Figure 4.3), showing the instability of the droplet. Consequently, it can be said that at almost a similar equilibrium surface tension, the noticeable retraction phase observed in water droplet was inhibited in the surfactant-laden droplets in the following order: SDS>MEGA-10>CTAB, where SDS wards off the vertical oscillations more than the other surfactants.

Next, the effects of substrate temperature, as well as the concentration and molecular weight of the surfactants solutions, on the impact dynamics of droplets were further investigated by running the experiments at the three different temperatures (–10, –20 and –30 °C) and four different surfactant concentrations (0, ~0.5×CMC, CMC and 2×CMC). Additionally, the interactions between the surfactant molecules and the impact substrate were thoroughly studied. The maximum spreading factor, retraction ratio and relaxing diameter of the droplets were measured for water and the solutions against their type and concentration at different temperatures, the results of which are shown in Figures 4.4–4.6, respectively.

Figure 4.4a shows the results obtained for the maximum spreading factor of SDS solutions and water droplets against the substrate temperature. According to the results, in all concentrations, SDS-laden droplets have a larger maximum spreading factor than water droplets. This higher maximum spreading factor becomes more noticeable at higher concentrations, where surfactants can significantly reduce the equilibrium surface tension of the solutions to approximately 34-35 mN/m (Figure 4.2). Based on these results, for the SDS concentration of 4, 8 and 16 mM, at –20 °C for example, the maximum spreading factor of droplets are 2.36±0.02, 2.49±0.03 and 2.53±0.07, respectively, which are noticeably higher than 2.16±0.04 for water droplets. This trend agrees well with the corresponding surface tension values reported in Figure 4.2.

Furthermore, the maximum spreading factor of water droplets decreases from 2.25±0.04 to 2.16±0.04 and 2.15±0.04 as the temperature drops from –10 to –20 and –30 °C, respectively. A similar trend is also seen in the maximum spreading factor of SDS solutions regardless of their concentration. This behavior can be attributed to the fact that the viscosity of the droplets is a function of temperature. It is well documented that the viscosity of water droplets increases with a power of 1.64 with a decrease in the temperature [148,167]. Consequently, energy dissipation, which is a function of viscosity, increases with a decrease in the temperature and results in a reduction in the maximum spreading factor. Although the viscosity of the SDS solutions and water droplets are not entirely identical, it is a reasonable assumption to expect a similar trend in both cases.

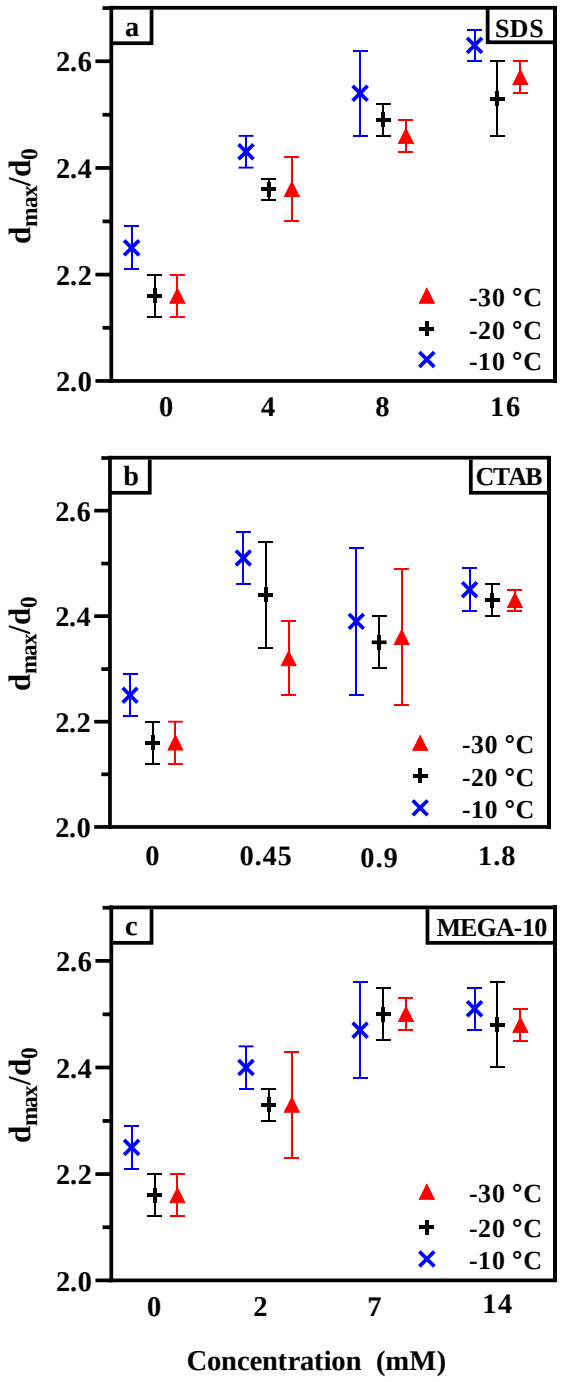

Figure 4.4. Maximum spreading factor of water droplets as well as the droplets of SDS, CTAB and MEGA-10 solutions of various concentrations at –10, –20 and –30 °C. The impact velocity was 1.08 m/s.

Energy dissipation (E) is a function of viscosity (μ), the initial droplet diameter (d_0), impact velocity (V) and the lamella height (h) of the droplets, where $E \propto \mu {d_0}^2 V^2/h$ [148]. The lamella height is defined as the smallest height of the droplet in the impact, which occurs due to the mass conservation when the droplet reaches the maximum diameter. In Figure 4.4a, we show that the maximum spreading factor increases with concentration, resulting in a reduction in the lamella height. To combine both influences of concentration and viscosity on the energy dissipation, it can be said that any increase in either the concentration or the viscosity of the solutions enhances the energy dissipation in the spreading phase.

Figure 4.4b shows the maximum spreading factor of water and CTAB-laden droplets versus concentration of the solutions and temperature of the substrate. It is seen that similar to Figure 4.4a, CTAB-laden droplets have a higher maximum spreading factor than water droplets. However, they do not follow a similar trend to that of SDS solutions with concentration. These results suggest that in addition to the equilibrium surface tension, which is a determining parameter in spreading of the droplets, there are other elements influencing the maximum spreading factor. Similar to SDS, it is seen in Figure 4.4b that decreasing the temperature of substrates results in a reduction in the maximum spreading factor of the solutions and water droplets due to the enhanced viscous effects. Based on Figure 4.4c, the maximum spreading factor of the MEGA-10 solutions follows a similar trend to that of SDS solutions; it increases with concentration and decreases with reducing the temperature.

Overall, regardless of the concentration, molecular weight and ionic nature, it can be concluded that surfactant-laden droplets have a higher maximum spreading factor compared to water droplets at subzero temperatures. For example, while water droplets at –30 °C have the smallest maximum spreading factor of 2.15±0.04, this parameter has increased to 2.57±0.03 for 16 mM SDS solution.

In addition to the concentration and type of surfactants, we showed that temperature also alters the dynamic behavior of the droplets; however, our results are contrary to the previous studies conducted at room temperature, which have introduced only Weber number as the governing element in the determination of the maximum spreading factor [118,168].

In the next step, we compared the contact time of droplets at different temperatures to investigate the role of viscosity and energy dissipation in this parameter. Contact time is defined as the time that a droplet is in contact with the substrate before its complete rebound. Since we did not observe a complete rebound for surfactant-laden droplets, the results of this section are limited to the contact time of water droplets. When the temperature of the substrate decreases from –10 to –20 and –30 °C, the contact time of water droplets increases from 13 to 15.2 and 16.8 ms, respectively. Here, two competing factors determine the dissipation energy, namely viscosity and lamella height. As mentioned before, viscosity increases with decreasing the temperature and on the other hand, lamella height increases since the maximum droplet diameter decreases. The increase in droplet contact time is an evidence showing that the viscosity effect is dominant and results in an enhancement in energy dissipation [135,156].

In order to reveal the influence of the studied parameters on the retraction phase of the solutions at subzero temperatures, we analyzed the retraction ratio of the solutions and compared the results with those of water droplets (Figure 4.5). This parameter, which is the ratio of the diameter of the droplets at the end of the retraction phase to their maximum spreading diameter, can have a value between 0 to 1. A value of 1 means that the droplet is not able to retract to its initial condition and fully spreads on the substrate. Conversely, a value of 0 corresponds to the ideal retraction and complete expulsion of the droplets from the substrate.

Figure 4.5a shows the retraction ratios of SDS solutions and water droplets with respect to the substrate temperature. As it is evident, regardless of the concentration, SDS-laden droplets have a higher retraction ratio compared to water droplets. For example, 4 mM SDS solution has a retraction ratio of 0.62±0.02 at –10 °C, which is three time as large as that of water droplets. At this temperature, when the SDS concentration increases from 4 to 8 and 16 mM, the retraction ratio also increases from 0.62±0.02 to 0.88±0.01 and 0.93±0.01, respectively, showing the key role of concentration in this phase. As the concentration increases, the ability of the droplets to retract and reach their initial conditions decreases. For example, regardless of the temperature, the retraction ratio of SDS solutions with a concentration of 8 and 16 mM is close to 1, meaning that the droplets fully spread on the substrate with no noticeable retraction. Additionally, when the temperature of the substrate decreases from –10 to –20 and –30 °C, at a low surfactant concentration (0.5×CMC), enhanced viscosity has no noticeable effect on this parameter. This shows the more pronounced effects of surface tension compared to viscosity.

The retraction ratios of CTAB solutions are shown in Figure 4.5b. It is seen that CTAB-laden droplets, similar to SDS solutions, have a higher retraction ratio than water droplets. The retraction ratio of 0.45 mM CTAB solution at –20 °C is 0.43±0.01, which is almost two times as large as that of water droplets. CTAB-laden droplets have a smaller retraction ratio compared with SDS solutions and it is almost independent of the concentration. This means that CTAB-laden droplets, even at high concentrations, have a more similar dynamic behavior to water droplets compared to SDS solutions at almost a similar equilibrium surface tension. Interestingly, the retraction ratio of CTAB-laden droplets does not follow a specific trend with the temperature either. The reason is that for CTAB solutions, we observed a partial rebound, resulting in the ejection of a secondary droplet. If the secondary droplet coalesces with the main one, the retraction ratio increases;

otherwise, due to the reduction in the final wetting diameter of the droplets, the retraction ratio decreases.

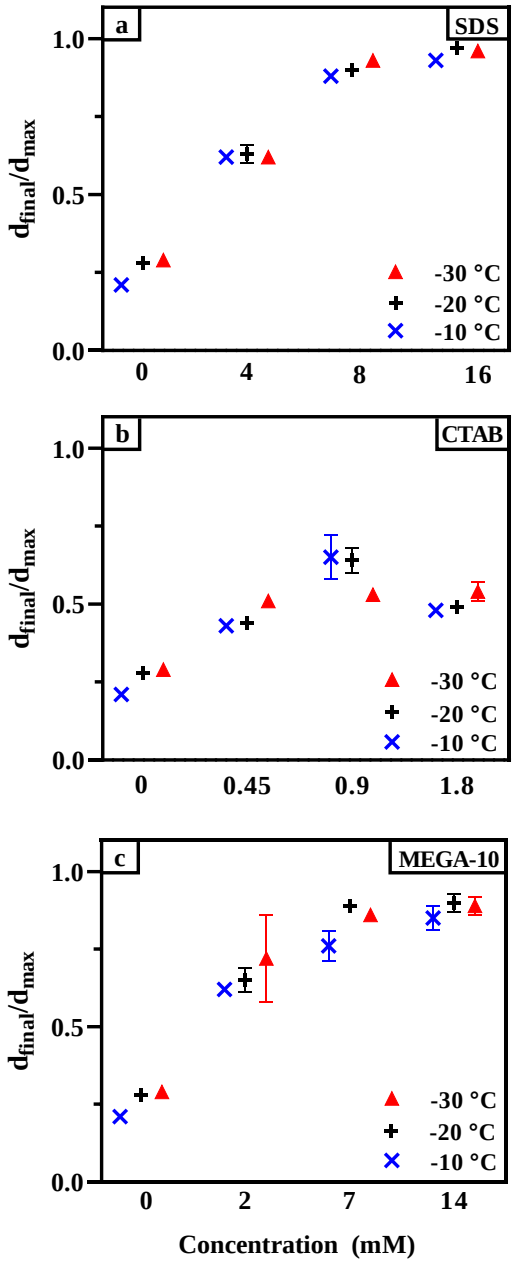

Figure 4.5. Retraction ratio of water droplets as well as the droplets of SDS, CTAB and MEGA-10 solutions of various concentrations at –10, –20 and –30 °C. The impact velocity was 1.08 m/s.

MEGA-10 solutions (Figure 4.5c) behave similar to SDS, where the retraction ratio increases with concentration and it is always larger than that of water droplets. For example, the retraction ratio of the droplets at –10 °C increases from 0.62±0.02 to 0.75±0.05 and 0.85±0.04 for the solutions having a concentration of 2, 7 and 14 mM, respectively. Moreover, due to the increased viscosity effects, the retraction ratio increases by lowering the temperature. For instance, the retraction ratio of 2 mM MEGA-10 increases from 0.62±0.02 to 0.65±0.04 and 0.72±0.14 by reducing the temperature from –10 to –20 and –30 °C.

By comparing Figure 4.5a-c, it is evident that the retraction ratio of SDS solutions is larger than that of the other solutions at a similar equilibrium surface tension, especially at high concentrations of CMC and 2×CMC. Since the initial kinetic and capillary energies of all the droplets at the releasing point are almost the same, there must be other parameters governing the impact dynamics of the droplets. To reach a solid conclusion, therefore, the specific role of molecular weight and ionic nature of the solutions must be separately investigated.

Surfactant-laden droplets have a lower capillary energy than water droplets during the spreading phase due to the diffusion of the surfactant molecules toward gas-liquid and solid-liquid interfaces, created during spreading and their replacement with the water molecules at those interfaces. This phenomenon weakens the hydrogen bonds existing among the water molecules and makes the surface tension of the solutions time-dependent, always having a value lower than pure water. The diffusion rate was shown to be a function of the mobility of the surfactant molecules [122,160,161,169]. By comparing the results of Figure 4.5a-c, one can conclude that SDS molecules with a smaller molecular weight (288.4 g/mol) compared to CTAB (364.5 g/mol) and MEGA-10 (349.5 g/mol) are able to diffuse toward the freshly created interfaces quicker than the other surfactants. Then, at a similar equilibrium surface tension, the SDS solutions reach their

equilibrium value (Figure 4.2) at a shorter time compared to the other solutions. Note that the equilibrium surface tension is the equilibrium state between the concentration of the surfactants at the interface and inside the droplet.

So far, we showed that solutions containing surfactants with a smaller molecular weight reach their equilibrium surface tension faster and they have a weaker retraction. However, when the retraction ratios of CTAB and MEGA-10 solutions at a similar equilibrium surface tension are compared, a significant difference is observed, especially at high concentrations of CMC and 2×CMC. Since these two surfactants have a close molecular weight (~4% difference), this noticeable difference in retraction ratios could be due to the ionic nature of the solutions. Surfactants consist of two components: a hydrophobic nonpolar tail and a hydrophilic polar head. When they are dissolved in water, their molecules arrange on the interfaces. We hypothesize that the orientation of the surfactant molecules on the superhydrophobic AKD and the type of bonding between the droplet and substrate are the parameters differentiating the dynamic behavior of CTAB and MEGA-10 solutions.

It has previously been shown that the zeta potential of AKD coatings is negative [170], providing the surface with numerous negatively charged sites. In MEGA-10, which is non-ionic, the hydrocarbon chains of the surfactant molecules can have hydrophobic interactions with the coating. Consequently, surfactant molecules arrange on the substrate with their heads up, which results in hydrophilization of the coating. On the other hand, the polar heads of the CTAB molecules can attract to the negatively charged sites of the coating resulting in exposure of the hydrophobic tails of surfactant molecules toward air and hydrophobization of the substrates [171]. Additionally, by increasing the concentration of CTAB solutions, a second layer of surfactant molecules, due to the hydrophobic interactions, can interact with the existing layer on the solid-

liquid interface and increase the accumulation of surfactant molecules at those areas. This type of distribution could be another reason for the significant difference between the dynamic behavior of CTAB-laden droplets, which seems to act very similar to water droplets and the other solutions.

To sum up, it can be said that CTAB solutions have a significantly different dynamic behavior compared to MEGA-10 solutions with only ~4% difference in their molecular weights due to three main reasons: (1) the polar heads of the CTAB molecules can attract to the substrate and restrict the mobility of the molecules resulting in a delay in reaching the equilibrium surface tension, (2) improving the non-wettability of the coatings by hydrophobization and (3) formation of a second layer of surfactants on the solid-liquid interface.

Since the final wetting area of the droplets at the end of the retraction phase has a critical role in the probability of ice nucleation, we analyzed the relaxing diameter based on the captured high-speed frames. This dimensionless number is the ratio of the final diameter at the end of the retraction phase (~t = 50-60 ms) to the initial diameter of the droplets at the time of the impact. The results of this analysis for the droplets of water and surfactants solutions are given in Figure 4.6a-c at different temperatures.

Figure 4.6a shows the droplets relaxing diameter for water and SDS solutions. It is seen that even at a low concentration of 0.5×CMC at –10 °C, the SDS solution has a significantly higher relaxing diameter of 1.51±0.05 compared to water (0.45±0.03). Moreover, increasing the SDS concentration from 4 to 8 and 16 mM, at this temperature, has resulted in an increase in the relaxing diameter from 1.51±0.05 to 2.22±0.08 and 2.44±0.04, respectively. Although the enhanced viscosity at low temperatures has not influenced the relaxing diameter of SDS solutions, it has increased this parameter for water droplets from 0.45±0.03 to 0.64±0.02 with a decrease in the substrate temperature from –10 to –30 °C.

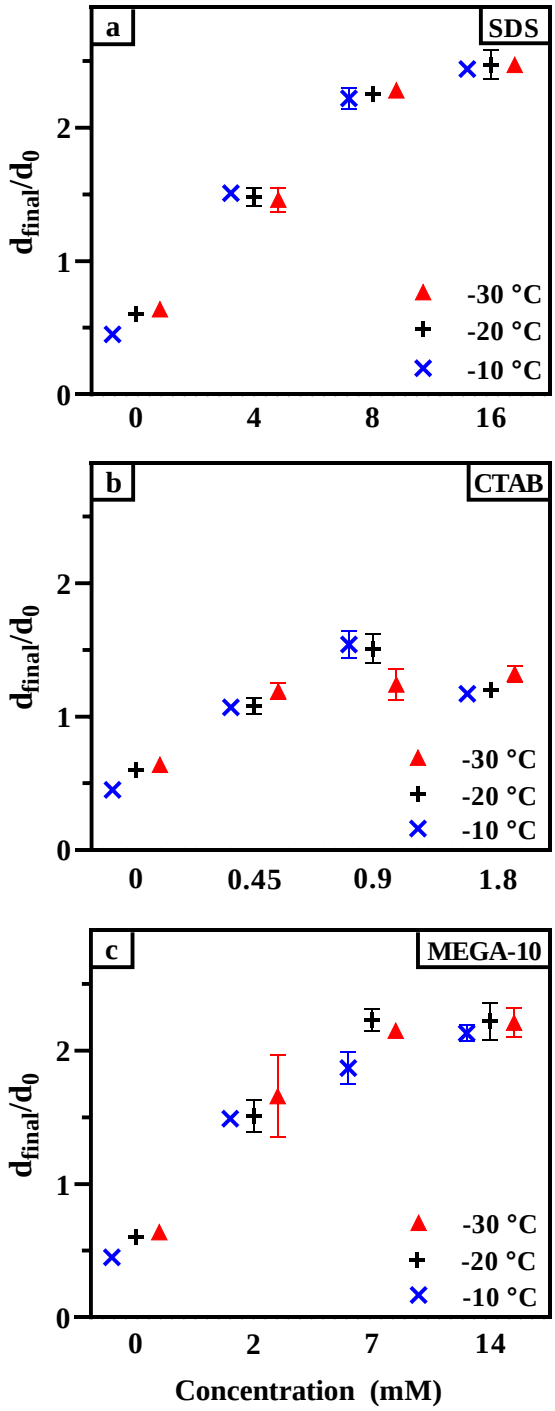

Figure 4.6. Relaxing diameter of water droplets as well as the droplets of SDS, CTAB and MEGA-10 solutions of various concentrations at –10, –20 and –30 °C. The impact velocity was 1.08 m/s.

Figure 4.6b shows the same parameter for CTAB-laden and water droplets. It is evident that CTAB-laden droplets, regardless of the concentration, have a higher relaxing diameter compared to the water droplets. For example, 0.45 mM CTAB has a relaxing diameter of 1.07±0.01 at –10 °C, which is significantly higher than that of water (0.45±0.03). It is to be noted that similar to the previous sections, the ability of CTAB solutions in promoting a larger wetting diameter is almost independent of the concentration and not as high as that of SDS solutions.

According to Figure 4.6c, the MEGA-10 solutions, similar to SDS solutions, have a higher relaxing diameter than water droplets. As a proof, the relaxing diameters of MEGA-10 solution droplets, having concentrations of 2, 7 and 14 mM, at –10 °C, are 1.49±0.03, 1.87±0.12 and 2.13±0.06, respectively, which are all higher than that of water (0.45±0.03). The enhanced viscosity effect is also clearly seen for MEGA-10 solutions, where the relaxing diameter of 2 mM MEGA-10 solution increases from 1.49±0.03 to 1.51±0.51 and 1.66±0.31 with a decrease in the temperature from –10 to –20 and –30 °C, respectively.

By comparing the relaxing diameters of SDS, CTAB and MEGA-10 solutions at CMC, with an equilibrium surface tension of ~34-35 mN/m, it is seen that CTAB solutions are more capable of preserving retraction properties of water droplets at freezing temperatures. This is most likely attributed to the larger molecular weight of CTAB compared to SDS and the attraction of its molecules to the negatively charged sites of the substrate with their heads down, which is not feasible in MEGA-10 solutions (non-ionic). This bonding of CTAB molecules with the coating makes the impact surface more hydrophobic and restricts the repopulation of the molecules on the gas-liquid interface.

4.3.3 Freezing of Droplets

According to the literature, the freezing time of the droplets at a specific temperature is a good indicator of the energetic barrier for ice nucleation [157]. In order to study the freezing time of water and surfactants solutions, we continued capturing the shape evolution of the droplets with the high-speed camera at 5000 fps in the first 6 min after the impact. Since the freezing time of all the droplets at –10 °C was extremely prolonged $t_{freezing}$ > 6 min, to better understand the role of surfactants in this phenomenon, we only report the freezing time of the droplets at –20 and –30 °C (Figure 4.7). It must be noted that the freezing time was determined by capturing the changes in the optical transparency of the droplets. However, for the solutions with a retraction ratio close to 1 (i.e., SDS and MEGA-10 solutions at CMC and 2×CMC), the ice buildup was not clearly traceable since the droplets were in the Wenzel state. In these cases, we determined the freezing time based on the volume change, which occurs during freezing of the solutions.

The freezing rate is mainly governed by the rate of heat conduction between the droplet and substrate as well as the heat convection between the droplet and ambient atmosphere [37,38]. The heat conduction rate through the substrate is described as $dQ/dt = -kA\Delta T$, where k, A and ΔT are the heat conduction coefficient, interfacial area and the temperature difference between the droplet and substrate, respectively. As shown in Figure 4.7, at –20 °C, for 4 mM SDS solution, the freezing time is 4391±943 ms, which is significantly lower than that of water droplets (14472±4607 ms). As the concentration increases to 16 mM, the freezing time decreases further to 1917±250 ms. One of the reasons for the observed acceleration in freezing is clearly attributed to the heat transfer rate between the droplet and the substrate.

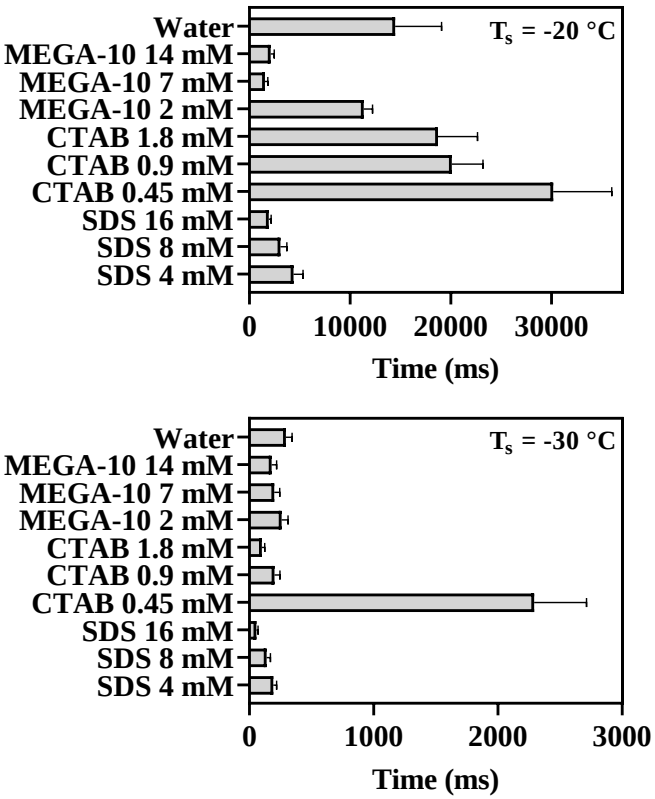

Figure 4.7. Freezing time of water droplets as well as the droplets of SDS, CTAB and MEGA-10 solutions. T_s represents the temperature of the substrates which is equal to –20 and –30 °C.

In the previous sections, it was shown that regardless of the concentration, SDS droplets easily spread on the substrate, inhibit the retraction and enhance the droplets relaxing diameter (Figure 4.6). This significant increase in the wetting area leads to the dissolve of the insulating air pockets existing on the superhydrophobic coatings [12], which leads to an increase in the heat conduction coefficient. Consequently, by transition of the wetting state of the droplet from Cassie-Baxter to Wenzel, the contact area between the liquid and solid phase increases [172]. As a result, freezing is accelerated in the SDS solutions and the energetic barrier for ice nucleation on the superhydrophobic coatings is reduced at subzero temperatures of –20 and –30 °C.

For the 2 mM MEGA-10 solution, the presence of MEGA-10 molecules has slightly accelerated the freezing time of the solution compared to water droplets from 14472±4607 to 11362±857 ms at –20 °C. This slight decrease in the freezing time considerably increases with concentration to the point that it reaches 2108±359 ms at 14 mM. Note that the same trend is also observed for the freezing behavior of MEGA-10 solutions at –30 °C. By comparing the droplet impact results of 4 mM SDS and 2 mM MEGA-10 solutions at –20 °C (Figures 4.6 and 4.7), it is seen that although there is no significant difference between the relaxing diameters of these solutions (1.48±0.07 and 1.51±0.12 for SDS and MEGA-10, respectively), SDS-laden droplets freeze more rapidly. This might be attributed to the smaller molecular weight of SDS compared to MEGA-10, resulting in a higher diffusion rate of its molecules toward the interfaces to reduce the surface tension and possibly filling up more air pockets of the surface.

Unlike SDS and MEGA-10, compared to water droplets, it takes more time for the CTAB-laden droplets to freeze at –20 °C regardless of the concentration. The freezing times of CTAB solutions with concentrations of 0.45, 0.9 and 1.8 mM were measured to be 30168±5811, 20102±3083 and 18718±3932 ms, respectively (Figure 4.7-top). Similar to the previous cases, freezing time decreases with an increase in the surfactant concentration, which could be attributed to the smaller surface tension at higher concentrations.

At –30 °C, an extraordinary delay in the freezing time from 295±49 for pure water to 2293±420 ms for 0.45 mM CTAB is observed. To better understand this behavior, the freezing time and relaxing diameter of water droplets were compared with those of the 0.45 mM CTAB solution at –30 °C (Figures 4.6 and 4.7). It can be seen that the presence of surfactant molecules has resulted in a higher relaxing diameter of 1.19±0.06 compared to that of pure water with a value of 0.64±0.02. Despite this higher relaxing diameter, it seems that heat conduction is not accelerated

and therefore, the ice nucleation in the solid-liquid interface of the CTAB solutions probably has a larger energetic barrier. We hypothesize that the unique interactions between CTAB molecules and AKD substrates could be the reason for the delay in freezing. The negatively charged sites of the AKD coatings attract the positive charges of the CTAB heads. The heads-down arrangement of the CTAB molecules provides the possibility of forming a second layer of molecules, tails to tails, on top of the first layer by hydrophobic interactions. The CTAB double molecular layer could act as an insulating layer against heat transfer between the droplet and the substrate and enhance the energetic barrier for ice nucleation. This may explain the extraordinary delay seen for CTAB-laden droplets at freezing temperatures of –20 and –30 °C. Since the freezing time decreases at higher concentrations, one can conclude that after a critical concentration, where a bilayer is formed on the surface, any further increase in this parameter accelerates freezing.

The influence of molecular weight, concentration and ionic nature of surfactants was also investigated on the ice front propagation inside the droplets. The freezing dynamics of all droplets were captured on superhydrophobic AKD coatings at –20 and –30 °C. For example, Figure 4.8 shows the droplet freezing dynamics of water and the solutions in the first 30000 ms after the start of freezing at –20 °C. In all cases, the first freezing stage starts with a rapid kinetic crystal growth at t = 0 ms (pointed with red arrow). This stage, which is identified by a change in the transparency of the droplets, starts from one contact point of the droplet with the solid-liquid interface and progresses throughout the whole droplet in less than 50 ms.

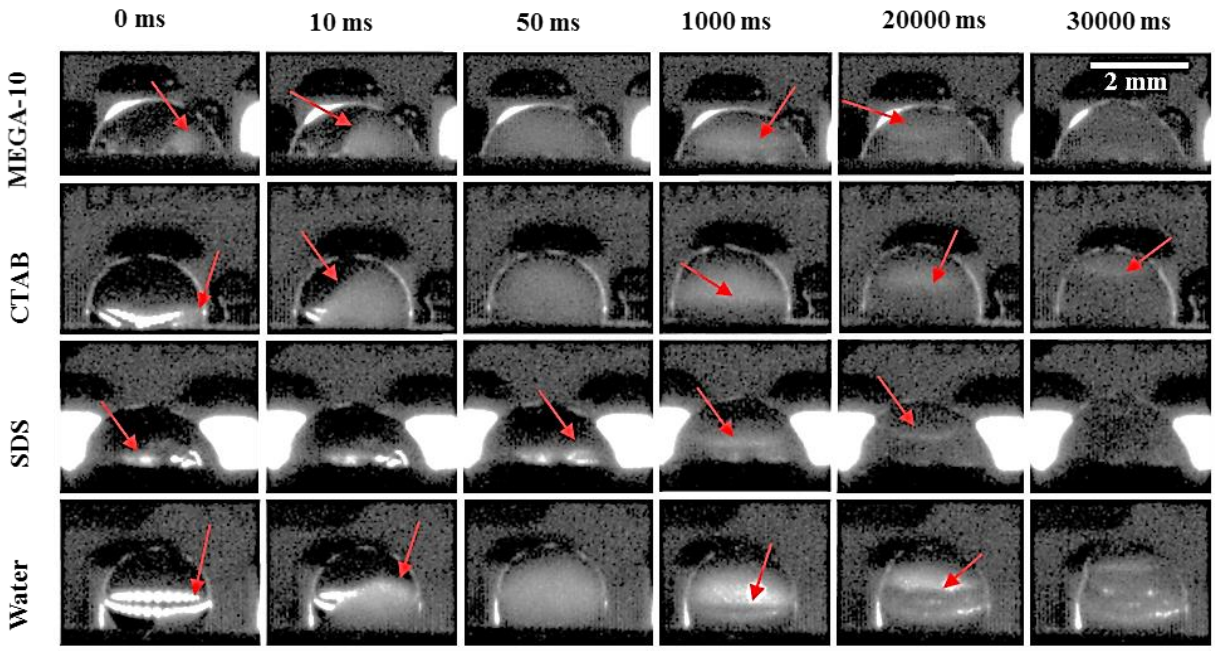

Figure 4.8. Freezing stages of water droplets as well as the droplets of SDS, CTAB and MEGA-10 solutions with concentrations of 4, 0.45 and 2 mM, respectively, having an equilibrium surface tension of 44.73±0.51 mN/m. The temperature of the substrate is equal to –20 °C. The scale bar is the same for all the frames.

Since the freezing starts from the solid-liquid interface, it can be said that the ice nucleation for the droplets of water and solutions is heterogeneous. It is to be noted that previous reports have introduced this type of ice nucleation as the main mode of crystallization for water droplets at the freezing temperatures of –20 and –30 °C [157,173]. In the next stage of freezing, when the droplet becomes fully opaque, it remains at the equilibrium temperature of 0 °C and an ice front is observed progressing vertically toward its tip (~ t = 1000 ms). The second stage happens isothermally and is a function of the heat transfer through conduction and convection among three phases [37,38].

We measured the time required for the ice front to progress from the solid-liquid interface until it finally contains the whole droplet, the results of which are given in Table 4.2. These results show

that in all cases, lowering the temperature of the substrate from –20 to –30 °C decreases the required time for ice front propagation. For example, by decreasing the temperature from –20 to –30 °C, the required time for ice front progress of water droplets is approximately reduced by 9 seconds, which is due to the higher heat transfer rate at lower temperatures. Additionally, it is seen that in almost all cases, as the concentration of the surfactant increases, the ice buildup process is accelerated.

Table 4.2. The time required for ice front formation inside the solutions and water droplets at –20 and –30 °C

	Concentration (mM)	Temperature (°C)	Ice front formation time (s)
CTAB	0.45	–20	33.4±3.3
		–30	23.2±3.3
	0.9	–20	25.2±1.2
		–30	23.5±3.6
	1.8	–20	29.1±1.7
		–30	20.9±2.6
MEGA-10	2	–20	33.8±4.1
		–30	17.9±6.1
	7	–20	25.0±2.4
		–30	17.2±5.5
	14	–20	21.1±1.8
		–30	12.6±0.8
SDS	4	–20	30.9±1.6
		–30	18.3±3.4
	8	–20	16.5±1.1
		–30	11.2±1.6
	16	–20	15.2±0.1
		–30	9.3±0.9
Water	0	–20	36.6±4.2
		–30	27.5±6.2

By comparing the results presented in Figure 4.7 and Table 4.2, it is evident that in all cases, increasing the concentration of the solutions makes both the droplets freezing time and the ice

front progress faster, possibly due to enhanced heterogeneous nucleation assisted by surfactants [174,175]. This shows that the extraordinary freezing delay observed in the previous section for CTAB solutions is more likely due to the formation of the insulating CTAB-bilayer on the coating and slower diffusion of their molecules toward interfaces compared to the other solutions. This leads to preservation of more air pockets on the surface and a lower heat conduction coefficient between the solid and liquid phases, which can lead to a higher energetic barrier for the heterogeneous ice nucleation.

4.4 Conclusions

We investigated the influence of the physicochemical properties of surfactants, as commonly used additives in various industrial applications, on the dynamic behavior and freezing of the droplets on non-wettable coatings at low temperatures. We elucidated the roles of concentration, molecular weight and ionic nature of three well-known anionic, cationic and non-ionic surfactants on these phenomena. Our results revealed that surfactants with smaller molecular weights and higher concentrations, compared to the other solutions, promote higher maximum spreading factors. Additionally, we showed that when the surfactant molecules and substrate have opposite charges, the surface non-wettability increases and the droplet behaves more similarly to water in the spreading and retraction phases. It was also shown that as the temperature of the substrate decreases, due to the enhanced viscous effects, the ability of the droplet to spread and retract decreases. In terms of freezing time, surfactants solutions generally freeze faster than pure water due to having a higher heat transfer rate with the substrate and a larger interfacial area, which are the results of the transition of the wetting state from Cassie-Baxter to Wenzel. An extraordinary freezing delay was observed, however, for CTAB solutions at –20 and –30 °C. This freezing delay could occur due to the interaction of the positive charges in the CTAB solutions with the negatively

charged sites of the AKD substrates. This phenomenon results in (1) hydrophobization of the substrate, (2) preservation of more air pockets on the surface and (3) formation of an insulating layer on the solid-liquid interface, which increase the energetic barrier for heterogeneous ice nucleation. Furthermore, it was shown that in all cases, the presence of surfactant molecules assists the heterogeneous freezing of the droplets at both subzero temperatures of –20 and –30 °C.

Chapter 5. Applications of AKD in Micro-Electro-Mechanical Systems (MEMS)

5.1 Fabrication and Characterization of Co-Sputtered Nickel-Tungsten Thin Films

5.1.1 Introduction

Over the past few years, nickel-tungsten (Ni-W) alloy coatings have gained much attention owing to their novel mechanical [47,48], tribological [49], thermal [50] and anti-corrosion properties [51]. As such, due to their high hardness, they are considered as a potential alternative to hard chromium coatings [176]. There are two techniques for the fabrication of Ni-W alloy films, including magnetron sputtering [177,178] and electrodeposition [179].

According to literature, electrodeposition is the most common and facile method to fabricate Ni-W coatings with low W content (less than ~23 atomic percent) [177]. Consequently, several studies have been conducted on the metallic alloys prepared by this method in order to characterize the mechanical properties and microstructure of the electrodeposited coatings [179–183]. Although this method is simple and effective, it suffers from some shortcomings that make it less attractive for the synthesis of such alloys. One drawback of this wet chemistry process is its limitation to be applied to all types of substrates. Furthermore, lack of uniformity in the fabricated coatings and generation of hazardous waste products during processing are some other major concerns of this method.

In order to fabricate Ni-W films, magnetron sputtering has been utilized as an alternative approach to electrodeposition. Since magnetron sputtering, which is a physical vapor deposition (PVD) method, is conducted under vacuum and uses pure targets as starting materials. This method is significantly cleaner than electrodeposition and can precisely control the composition of coatings. To our knowledge, there have been only a few reports on the sputtered Ni-W alloy thin films with thickness under 2-3 μm [177,184,185]. In one study on sputtered ~50 nm Ni-W coatings, it was

shown that the samples containing up to 24.2 atomic percent (at.%) W were completely nanocrystalline while by increasing the W content to 30.8 and 66.3 at.%, respectively, amorphous-nanocrystalline and nanocrystalline phases appeared in the microstructure [185]. The authors demonstrated that the correlation of hardness with W content in nanocrystalline Ni-W alloys, containing up to 20 at.% W, is linear; thus, it will not be reliable to utilize the traditional models to predict the solid solution strengthening behavior of such materials [185]. It is worth noting that based on the traditional models, the hardness from alloying is correlated to the W composition in the form of a parabolic equation [186,187].

In another study, Ni-W thin films were annealed at 800 K for 1 h to investigate the impact of heat treatment on their mechanical properties and microstructure. It was shown that for samples containing less than 25 at.% W, a softening was observed after annealing due to the grain growth and drop in hardness. On the contrary, by increasing the W content from 25 to 85 at.%, although the grain size of the samples increased by approximately 10 folds (from ~10 to ~100 nm) after annealing, the hardness increased [184]. This hardness enhancement could be more attributed to the phase composition of the coating rather than the grain size and Hall-Petch effect.

The present study aims to investigate the impact of W content on the mechanical properties and surface morphology of the co-sputtered Ni-W alloy thin films. According to the literature, the majority of studies in this area have focused on the Ni-W alloys with W contents below 40 at.%. Thus, this is the first study on co-sputtered Ni-W alloy films focusing mostly on the impact of the W content and alloy phase on the mechanical properties and surface morphology of the films with thicknesses of < 2.5 μm. A series of experiments were carried out on a broad composition range of Ni-W alloy thin films from pure Ni to pure W deposited on silicon wafers using magnetron co-sputtering under vacuum at low sputtering pressure (0.27 Pa). The silicon wafer substrates were

coated with a thin (~20 nm) buffer layer of titanium (Ti) prior to co-sputtering. By controlling the sputtering power of Ni and W guns as well as the sputtering pressure and without any further heat treatment, a high hardness of 21.9±2.0 GPa was achieved for the sample containing 79 at.% W with a thickness of 2.5 µm. We believe that this study is a step forward toward enhancing the understanding of microstructure and surface morphology of Ni-W thin films as potential substrates used in a wide variety of high-tech applications including micro- and nano-electro-mechanical systems [188].

5.1.2 Experimental Procedure

To produce the Ni-W alloy thin films, we used an ATC-Orion 5 UHV magnetron sputtering system (AJA International, USA) equipped with three targets: Ni (99.999%), Ti (99.995%) and W (99.95%). All three targets had a diameter of 2 inches (50.8 mm) and were purchased from AJA International. Single-side polished silicon wafers with an orientation of (1 0 0), a diameter of 100 mm and a thickness of 500 µm (UniversityWafer, USA) were used as substrates. High-purity argon (Ar) was used as the sputtering gas. Prior to co-sputtering Ni and W, a thin layer (~20 nm) of Ti was deposited on the silicon wafers at cathode power of 50 Watts for 12 min. The purpose of this interlayer is to reduce the residual stresses of the samples [189] and have a more uniform coating with enhanced adhesion [190]. In addition, this layer acts as a barrier against Ni and W diffusion to the substrate, which generally occurs due to their relatively low energy barriers and tendencies for forming complex structures with the substrate [191]. Before the sputtering process, plasma of both Ni and W targets was running with a closed shutter for almost 1 min to ensure that no contamination is present. The target to substrate distance of the sputtering instrument was ~140 mm. It is worth noting that we conducted a standard sputtering without substrate bias. The substrates were at room temperature at the beginning of the sputtering and the experiments were

conducted without cooling/heating the substrates. No plasma etching was performed on the substrates prior to deposition. During the sputtering, the base pressure of the vacuum chamber and the sputtering pressure were set at ~1.3×10^{-6} Pa (~10^{-8} Torr) and 0.27 Pa (2.0 mTorr), respectively. To achieve the desired composition of Ni-W alloy films (i.e., W content of 0 to 100 at.% with ~20% increments) with a thickness of approximately 1-2.5 µm, the radio frequency (RF) power and direct current (DC) power of the Ni and W guns (cathodes) were varied from 100-270 and 40-250 Watts, respectively. All the details of the sputtering process including the sputtering time, the power of both Ni and W guns and the final elemental composition of the samples are given in Table 5.1. The thickness of the coatings was measured using a DEKTAK 150 surface profilometer (Veeco, USA). Note that our sputtering machine was not equipped with a crystal monitor module.

To determine the composition of the films, energy dispersive spectroscopy (EDS) was performed on the samples at a voltage of 20 kV with a scanning area of ~10 µm×10 µm using a Hitachi SU-70 (Hitachi, Japan). Moreover, in order to identify the phases in the samples, we used a PANalytical X'Pert Pro diffractometer (Malvern, UK) with Ni-filtered $Cu_{K\alpha}$ X-ray radiation having a wavelength of 0.15418 nm. The X-ray diffraction (XRD) patterns were collected with a step size of 0.01° and acquisition time of 40 s per step size in the diffraction angle range of 20 to 110°. The collected patterns of pure Ni and pure W were then compared against the International Center for Diffraction Data (ICDD) reference codes to identify the phases. It must be noted that prior to the phase characterization of the thin films, the XRD instrument was calibrated with standard reference material (1976b) from NIST (National Institute of Standards and Technology) to ensure that no peak shifting comes from the instrument. Scanning electron microscopy (SEM) was conducted on a Hitachi SU-70 system (Hitachi, Japan) to capture the surface features as well as the growth pattern of the samples. It is to be noted that in order to ensure the quality and accuracy

of the SEM results, all the images were captured several times. Furthermore, in order to construct the surface topography of the thin films and measure the surface roughness, we performed atomic force microscopy (AFM) using a Dimension Icon module (Bruker, USA). We used a silicon cantilever with a length of 110-140 μm, a spring constant of 20-80 N/m and a frequency of 312-347 kHz. During the AFM experiments, the scanning area and rate were 0.50 μm×0.50 μm and 0.3 Hz, respectively. Next, the AFM images were analyzed with commercial image-processing software (Gwyddion 2.55). Finally, the hardness of each coating was measured using a Tukon 1202 digital microhardness tester (Buehler, USA) equipped with a Vickers indenter. All the hardness measurements were performed on at least 15 randomly-chosen spots on the surface of the samples. The indentation force load and dwell time were 0.098 N and 10 s, respectively. For each run, the lengths of the diagonals of the Vickers indent were measured with the instrument's high-resolution optical microscope at 50× objective magnification (500× total). The Vickers hardness was then measured using Eq. (5.1):

$$H_V = \frac{1854.4F}{d^2} \tag{5.1}$$

where H_V is the Vickers hardness in GPa, F is the applied load on the sample during the indentation in N and d is the average length of the indent diagonals in mm.

5.1.3 Results and Discussion

The composition of the co-sputtered Ni-W coatings of different alloy compositions (0-100 at.% W) was determined by using energy dispersive spectroscopy (EDS), the results of which are shown in Table 5.1. In order to identify the phases present in the films, we collected their XRD patterns in the range of $20° < 2\theta < 110°$, which are displayed in Figure 5.1. The intense peak observed in

all the XRD patterns at 2θ ~69° belongs to the (1 0 0) plane of the silicon wafer substrates [192,193].

Figure 5.1a shows the XRD patterns of the pure Ni, which perfectly matched with reference code 04-002-1862 [194]. The most intense peak at 2θ=44.49° corresponds to the (1 1 1) plane of the face-centered cubic (FCC) Ni [195,196]. Moreover, the other peaks present at 51.82, 76.36, 92.92 and 98.44° matched with (2 0 0), (2 2 0), (3 1 1) and (2 2 2) planes of FCC Ni, respectively. By the addition of 20 at.% W to Ni host (Figure 5.1b), the intense peak of pure Ni is slightly shifted to the lower diffraction angles from 44.49 to 43.20°, which is in agreement with other studies [184]. Also, the (2 2 2) plane of Ni is shifted from 98.44 to 94.82°. The reason behind this peak shifting might be mostly due to the incorporation of the larger W atoms (r_W = 1.41 Å) [197] Ni lattice with a smaller atomic radius (r_{Ni} = 1.28 Å) [197], which leads to an increase in the average of the nearest neighbor distance (i.e., interplanar or *d*-spacing) [198]. When the W content increases to 39 and 55 at.% (Figure 5.1c and d, respectively), a weak and broad peak is observed at 2θ=42.75 and 41.53°, suggesting the presence of an amorphous (and/or nanocrystalline) phase [188].

Based on the equilibrium phase diagram of Ni-W binary system (with a solubility limit of ~12 at.% W in Ni) [199], one expects to see a mixture of intermetallic compounds, including Ni_4W, NiW and NiW_2 in these range of compositions (Figure 5.1c and d). However, due to the high quenching rates in magnetron sputtering, this method becomes a non-equilibrium synthesis process. Consequently, the intermetallic phases might get bypassed in favor of formation of metastable amorphous phases [200–202]. It is worth mentioning that the sharp peaks in Figure 5.1b suggest a solubility limit of 20 to 39 at.% of W in Ni, which is in contrary to the equilibrium

phase diagram of this system. One of the main reasons for the observed discrepancy is the non-equilibrium nature of sputter deposition that could result in supersaturation [203].

It is seen that by increasing the W content from 39 to 55 at.%, the broad peak is still present in the pattern. To better reveal this trend, two films were fabricated by enhancing the W content to 79 and 100 at.% (Figure 5.1e and f, respectively). According to Figure 5.1e, the intense peak at $2\theta=43.21°$, which most likely refers to the solid-solution of the Ni in BCC-W, suggests that the film is phase pure and the structure is nanocrystalline. Based on the 01-077-3490 reference code [192,194,204], the most intense peak appears in the XRD results of the pure W sample at $2\theta=39.97°$ and the other peak at $2\theta=86.25°$ are indexed as (1 1 0) and (2 2 0) planes of body-centered cubic (BCC) W. To identify the phases present in the Ni-79 at.% W film, Figure 5.1e and f should be compared. It is seen that with incorporation of Ni with smaller atoms into the host lattice (W), the *d*-spacing has decreased and two peaks of pure W have shifted from 39.97 and 86.25° to higher diffraction angles of 43.21 and 94.83°, respectively.

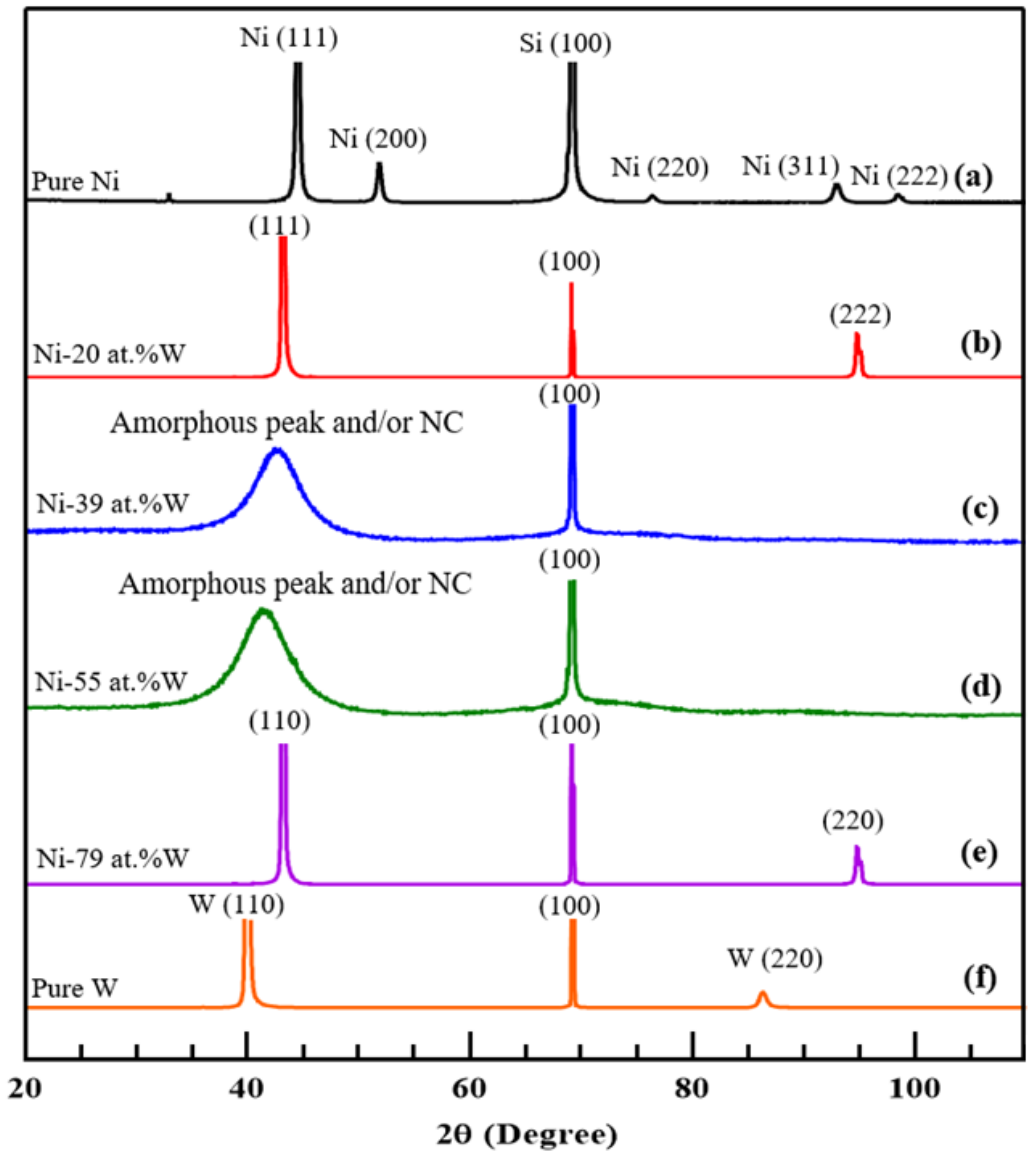

Figure 5.1. X-ray diffraction (XRD) patterns of co-sputtered Ni-W films on silicon wafer substrates with respect to the W at.% of the samples: (a) Pure Ni, (b-e) Ni-W films with 20, 39, 55 and 79 at.% W, respectively and (f) Pure W. It is to be noted that "NC" in (c) and (d) refers to nanocrystalline phase.

The XRD peaks, shown in Figure 5.1, were also used to calculate the average crystallites size of each sample. We fitted the signal intensity and diffraction angle of the patterns using a Gaussian

distribution function based on Eq. (5.2), where a is the peak height, x_0 is the peak center position, s is the standard deviation controlling the peak width and b is the vertical off-set of the peak.

$$f(x) = b + a.e^{\frac{-(x-x_0)^2}{2s^2}} \quad (5.2)$$

Then, we applied the results to the Scherrer equation defined as:

$$d = \frac{k\lambda}{\beta \cos(\theta)} \quad (5.3)$$

where *k* is a constant dimensionless shape factor equal to 0.90 in the present study, λ is the X-ray wavelength (1.54178 Å), θ is half of the diffraction angle in radian and β is the peak full width at half maximum intensity measured based on the fitted XRD peak using the Gaussian distribution function in radian. It is to be noted that the reported crystallite size values in Table 5.1 have been obtained from the most intense peak of the non-amorphous samples which was observed at 39<2θ <45°.

Table 5.1. Summary of the sputtering parameters, including the sputtering time and cathodes (guns) power as well as the thickness, elemental composition (determined by EDS) and the grain size (from the Scherrer equation) of the Ni-W alloy thin films

Sample	Sputtering Time (min)	Cathode (gun) Power (Watts)		Thickness (µm)	Ni (at.%)	W (at.%)	Crystallite Size based on the Scherrer equation (nm)
		Ni (RF)	W (DC)				
1	210	250	-	1.8	100	0	42
2	210	270	40	2.2	80	20	84
3	210	195	55	1.5	61	39	-
4	210	200	100	2.2	45	55	-
5	210	150	150	2.5	21	79	67
6	75	-	200	1.0	0	100	31

According to the results obtained from Scherrer equation, it is seen that the crystallite size of the sample containing 20 at.% W is almost twice as large as that of the pure Ni. This relation is also seen in the previous studies, where the crystallite size of Ni-20 at.% W was 24±16 nm compared to pure Ni with a crystallite size of 10±3 nm [185].

To better understand the impact of W addition on morphology of the films, the surface and cross section of each sample were thoroughly examined by using SEM and displayed in Figure 5.2 (the full-size versions of the cross-sectional SEM images are given in Figure A6 in Appendix A). It is evident from Figure 5.2a for pure Ni that the surface is uniform and mainly consists of pointy features with a mean diameter of 51.58±13.33 nm. Note that these features resemble the growth of (1 1 1) planes of FCC Ni in [1 1 0] direction. By incorporating W atoms into the Ni structure up to 20 at.%, some larger features (compared to pure Ni), with a mean diameter of 77.29±9.05 nm, are seen, which are surrounded by smaller ones with a diameter of 29.58±5.33 nm. These features are marked in Figure 5.2b by blue and red arrows, respectively. When we compare the surface morphology of this sample with its cross-sectional SEM image (inset of Figure 5.2b), a conical growth pattern is observed, resembling two different surface features previously shown. Moreover, we compared the surface morphology of the co-sputtered Ni-20 at.% W film in this work with the one previously reported for an electroplated Ni-W alloy coating with 24 at.% W [198]. The comparison revealed that in both cases the surface morphology follows the same pattern showing a mixture of differently shaped features of various sizes. However, the surface features of the films in this study are much smaller than those of the electroplated coating (2.54±1.42 μm).

When the W content increases to 39 at.% (Figure 5.2c), the features with sharp borders, previously observed in Figure 5.2b, transform to a very smooth surface with some patterns underneath. There are a few large bumps on the surface, showing a non-uniform pattern in the film. By comparing

Figure 5.1c and 5.2c, it is concluded that this sample contains amorphous and/or very fine nanocrystalline structure which is not observed in either plan or cross-sectional SEM views. Note that SEM of Ni- 39 at.% W was conducted at high magnifications; however, no surface features was captured, due to the surface being extremely smooth.

When the W content increases to 55 at.% (Figure 5.2d), it is seen that by moving from the Ni-rich coating (Figure 5.2c) to the W-rich coating (Figure 5.2d), some small features with a diameter of 36.38±10.64 nm appear on the surface. Considering the small size of these features formed on the surface, it is suggested that the coating is still in the transition phase from an amorphous/nanocrystalline to a nanocrystalline structure. By increasing the W content to 79 at. %, it is seen that two different patterns having small (25.63±6.19 nm, red arrows) and large (84.25±29.18 nm, blue arrows) features are formed on the surface (Figure 5.2e). The EDS results verified that the elemental composition of both patterns are identical and contain 21 at.% Ni and 79 at.% W. Therefore, as it is shown in the inset of Figure 5.2e, the difference in the patterns might be due to irregular directional growth of the atoms during the deposition. By comparing Figure 5.2a-e, it is evident that the mean diameter of the surface features has relatively decreased by ~50%, showing that in higher W concentrations, more grain/columnar boundaries are obtained.

The SEM image of pure W in Figure 5.2f shows that the W atoms have grown in needle-like patterns having a mean length of 65.24±19.98 nm with different orientations. Moreover, the cross-sectional SEM image of this sample presents the columnar growth of W atoms on the substrate, which represents the growth of the BCC films in the close packed [1 1 1] direction [205].

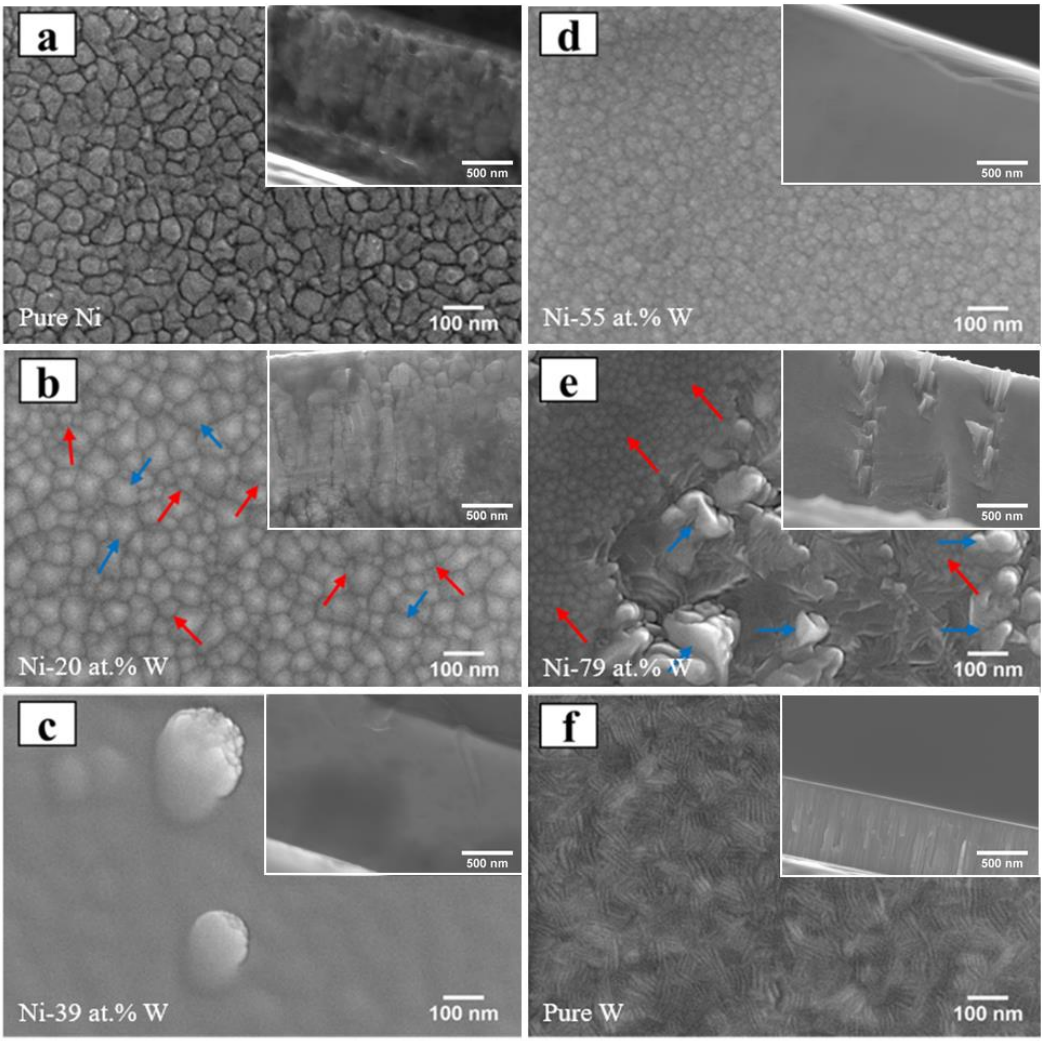

Figure 5.2. Scanning electron microscopy (SEM) images of the co-sputtered Ni-W thin films with respect to their W content: (a) pure Ni, (b-e) Ni-W coating with 20, 39, 55 and 79 at.% W, respectively and (f) pure W. The red and blue arrows in b and e, point to the two types of surface features observed in these samples. Insets: the cross-sectional SEM images of each sample. The full-size versions of the insets are given in Figure A6 of Appendix A.

To investigate the effect of W content on the surface topography and roughness of the films, we conducted a series of experiments using AFM, the results of which are shown in Figure 5.3. In Figure 5.3a, the topography of the pure Ni film shows that the surface is composed of numerous large bumps with a diameter and a maximum height of 49.23±13.05 and 9.8 nm, respectively. By

increasing the W content of the samples from 0 to 20 (Figure 5.3b), the size distribution of the features on the surface changes. The AFM result reveals that there are some round features with a diameter of 21.80±2.74 nm (pointed by red arrows) surrounded by larger ones having a diameter of 52.16±5.34 nm (pointed by blue arrows). By comparing Figure 5.3a and b, it can be concluded that the addition of W to the Ni structure has decreased the peak-to-valley difference from 17.2 nm for pure Ni to 13.3 nm for Ni-20 at.% W.

Similar to the SEM results, by increasing the W content to 39 and 55 at.% (Figure 5.3c and d, respectively), the large bumps seen in Figures 5.3a and b disappear and no distinct pattern is detectable. The 39 and 55 at.% W samples have the peak-to-valley differences of 1.8 and 1.1 nm, respectively, significantly lower compared with those of the previous samples. This could be due to the different growth pattern of these two samples than the pure nanocrystalline samples. The structure growth orientation in such amorphous/nanocrystalline mixed systems does not follow a particular direction and as a result, no distinct texture appears on the surface. The observed smooth morphologies in SEM images (Figure 5.2c and d) and the amorphous/nanocrystalline phase identified by XRD (Figure 5.1c and d) are in agreement with this hypothesis.

The 79 at.% W sample (Figure 5.3e) shows globular features on the surface with an average diameter of 27.05±6.57 nm. Among all the nanocrystalline samples, the one with Ni-79 at.% W has the finest surface features. Finally, the surface topography of sputtered pure W is shown in Figure 5.3f, demonstrating needle-like patterns that resemble the (1 1 0) planes of the BCC structure (Figure 5.2f) [205,206].

AFM was used to find the surface roughness of the samples, the results of which are reported in Table 5.2. The roughness average (R_a) and root mean square (*RMS*) values of the surface suggest that the W content plays an important role in the surface roughness of the Ni-W thin films. The

RMS of pure Ni is 2.4 nm and by increasing the W content to 20, 39 and 55 at.%, it decreases to 1.9, 0.1 and 0.1 nm, respectively. These results show that the last two samples are markedly smoother than the other ones. Furthermore, the maximum roughness average (R_a) of crystalline samples follows the same trend as *RMS* and decreases with increasing the W content from 0 to 55 atomic percent. The decreasing trend in the surface roughness with increasing W content might be attributed to the fact that surface morphology of pure Ni is pointy (Figure 5.2a), while the surface morphology of pure W is needle-like (Figure 5.2f).

Comparing the SEM and AFM results of the films illustrated in Figures 5.2 and 5.3, respectively, indicates that by increasing the W content, the size of the surface features of nanocrystalline samples decreases, which is in agreement with the findings of relevant studies in the literature [185]. Moreover, the roughness analysis of the AFM images, shows that the peak-to-valley difference values and the roughness of crystalline samples are also reduced as the W content increases, which might be due to the surface texture and growth patterns of the samples.

Table 5.2. The impact of W content on the roughness average (R_a) and root mean square (*RMS*) values of the co-sputtered Ni-W coatings with respect to the elemental composition and microstructure

Sample	*RMS* (nm)	R_a (nm)	Structure (based on the XRD patterns)
Pure Ni	2.4	1.9	Nanocrystalline
20 at.% W	1.9	1.5	Nanocrystalline
39 at.% W	0.1	0.1	Amorphous and/or Nanocrystalline
55 at.% W	0.1	0.1	Amorphous and/or Nanocrystalline
79 at.% W	1.1	0.9	Nanocrystalline
Pure W	1.0	0.8	Nanocrystalline

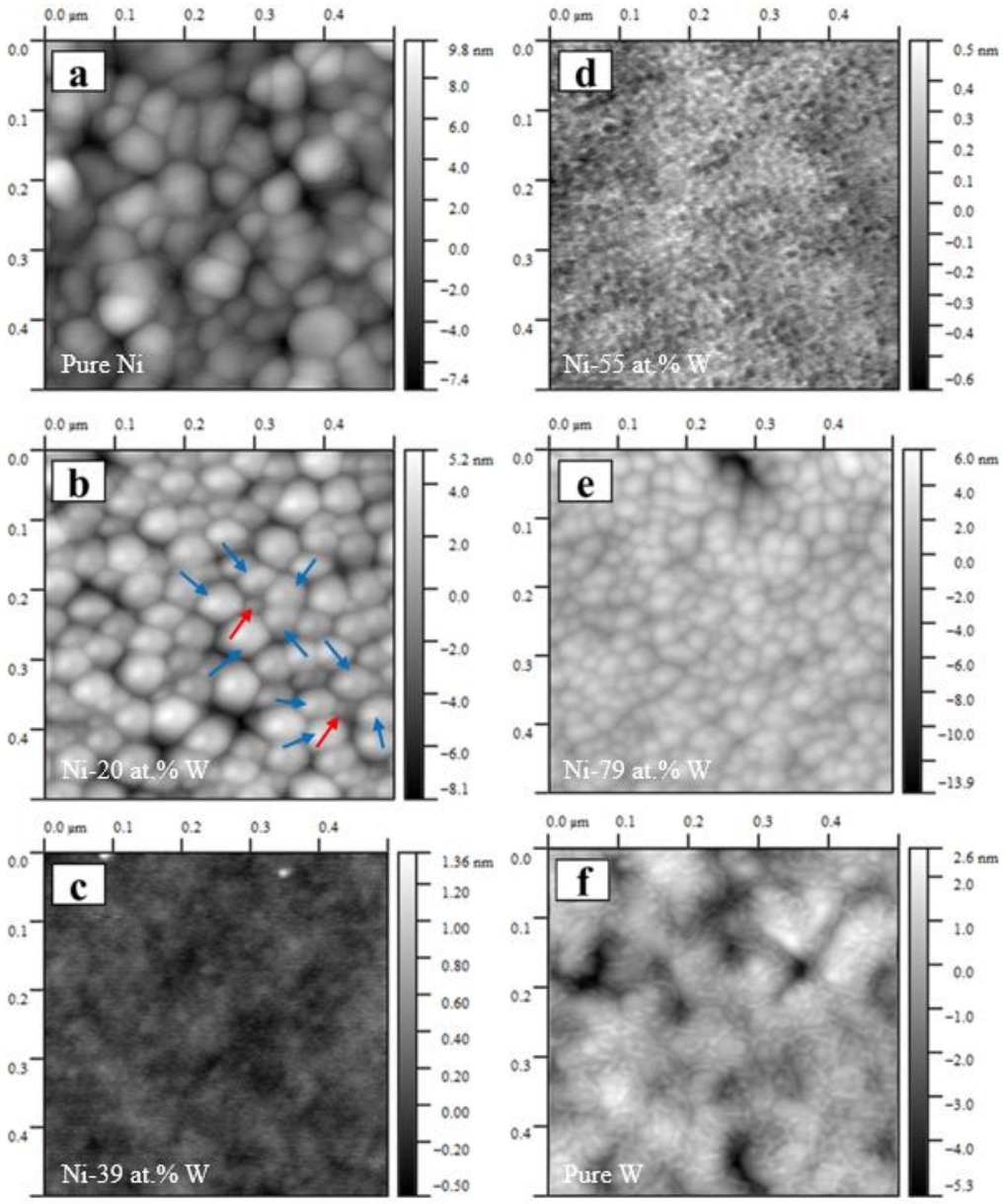

Figure 5.3. Atomic force microscopy (AFM) of the co-sputtered Ni-W thin films with respect to their elemental composition: (a) pure Ni, (b) Ni-20 at.% W, (c) Ni-39 at.% W, (d) Ni-55 at.% W, (e) Ni-79 at.% W and (f) pure W. The red and blue arrows in b point to the two types of surface features observed in the sample.

To investigate the influence of W content on the mechanical properties of the co-sputtered Ni-W thin films, we measured the hardness of the samples at 15 randomly-chosen spots using a

microindentation system equipped with a Vickers indenter. Based on the results, the relation between the hardness and elemental composition of the samples does not follow the same pattern in all W composition intervals. Thus, to get a clear idea of the influence of W content on hardness, all the data points were divided into three groups (W<40, 40<W<55 and 55<W<80 at.%) and a linear regression model was fitted to each region, the results of which are displayed in Figure 5.4.

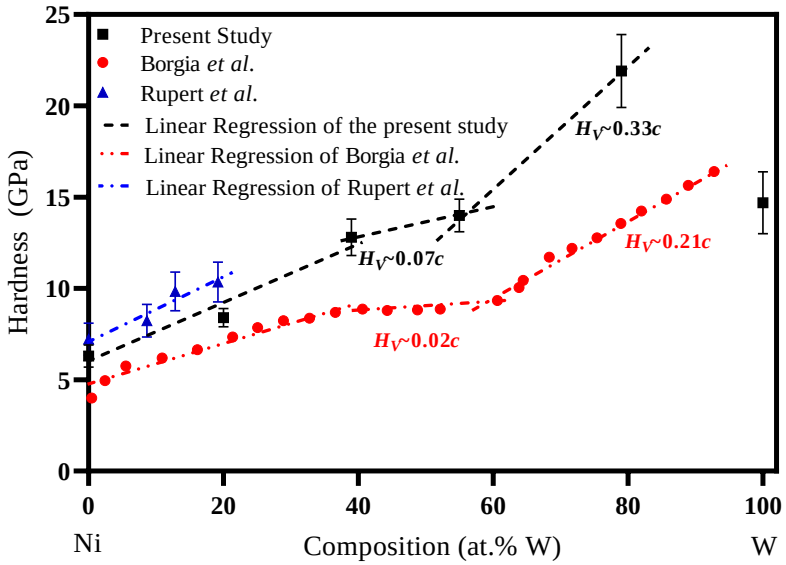

Figure 5.4. Comparison of Vickers microindentation hardness of the co-sputtered Ni-W thin films of the present work with relevant studies of the literature with respect to the W content [184,185]. The force load and dwell time of indentation in our hardness measurements were 0.098 N and 10 s, respectively. Linear regression was fitted to each series of data points to quantitatively indicate the dependency of the hardness on the W addition. *c* is the W content in the films in atomic percent.

In the first region, in which W content varies from 0 to ~40 at.%, the hardness enhances by an increase in the W content. A hardness of 6.3±0.6 GPa was measured for the nanocrystalline pure Ni film, which is in perfect agreement with relevant previous studies [184,185,207]. When the W content increased to 20 at.%, the hardness increased by ~28% and reached to 8.4±0.5 GPa. At this

point, as can be seen in Figure 5.4, the hardness values of nanocrystalline Ni-W alloys containing up to 20 at.% W are almost in the same range as those reported in other studies [184,185], which verifies the accuracy of our method and instrument. Note that here the increase in the rate of H_V with W content is ~ 0.17c (c = W content in at.%), which is close to the values of 0.11c and 0.17c reported by previous studies [184,185], respectively. This increasing trend in the hardness of Ni-W alloys continues with the addition of more W. According to Figure 5.4, the hardness of the sample with 39 at.% W is 12.8±1.0 GPa, which is considered a sharp increase for such systems. To put this into perspective, such high hardness could be achieved from a pure nanocrystalline Ni if the grain size is reduced from 200 to almost 40 nm [208].

With increasing the W content to 55 at.%, the hardness slightly increases to 14.0±0.9 GPa. However, the rate of hardness increase (H_V ~ 0.07c) is considerably lower than that of the previous hardness-composition regime (H_V ~ 0.17c), which could be attributed to the formation of the amorphous phase, previously discussed in the XRD results (Figure 5.1c and d). By increasing the W addition to 79 at.% and disappearance of the amorphous phase, the hardness increases sharply with a rate of H_V ~ 0.33c to 21.9±2.0 GPa, which is the highest value obtained in the current study. By comparing the increasing rate of hardness in the fully crystalline regions, it is seen that the hardness increases with a higher rate in the W-rich region. Mishima *et al.* [209] conducted a thorough study on role of transition metal and B-subgroups solutes on solid solution hardening of Nickel. They found that in case of transition metal elements an extra hardening is observed over what is expected from the same treatment on B-subgroup elements. This extra hardening in case of transition metals is historically attributed to their electronic interaction with the host Nickel [210]. In solid solutions, in addition to a climb-glide mechanism, which is dominant in unalloyed nickel, the solute atoms act as pinpoints and provide further resistance to dislocation motion [211].

Therefore, considering the effect of W concentration and its extra hardening as a transition metal, it is plausible that with increasing W concentration, its hardening effect adds up to the alloy in a nonlinear fashion and results in higher hardness after a certain point. The hardness is then dropped to 14.7±1.7 GPa for the nanocrystalline pure W.

To get a solid grasp of the underlying mechanisms of increasing hardness in Ni-W alloys, more in-depth literature studies was carried out. The effect of reduced grain size on the strength of materials is well known as the Hall-Petch equation proposed in the 1950s [212,213]. In the current study, we showed that based on the Scherrer equation (Table 5.1), the crystallite sizes of the samples are between 31 and 84 nm, which are very close. Thus, it is not possible to interpret the hardness results based on the crystallites size. Therefore, the contribution of solid solution strengthening from W in nanocrystalline Ni could be remarkable and considered as the main mechanism for the observed hardness improvement, which is also aligned with the findings of Rupert *et al.* on sputtered Ni-W thin films with 0-20 at.% W [185]. Here, the obtained hardness values for the films up to 20 at.% W are very comparable to those reported by Ref [185], who only studied the mechanical properties of the films containing 0–20 at.% W with a single-phase solid solution. Note that the authors observed an amorphous phase for the W content of 30.8 to 66.3 at.%, but did not discuss their mechanical properties in details.

By comparing the hardness results of the present study with those reported in Ref [184], it is evident that both studies follow the same increasing hardness trend up to 80 at.% W. The only considerable difference is related to the rate of hardness increase. The higher hardness obtained in our study might be due to the fact that the W-rich samples are hard BCC, as confirmed by the XRD and SEM results (Figures 5.1f and 5.2f). However, in Ref [184], instead of BCC W, a metastable phase of W, namely β-W, which is less hard than BCC W [205], was present in the sample

containing 75 at.% W. It is well documented that formation of these two phases is a function of the sputtering pressure [205]. With a lower sputtering pressure, it is more likely to have BCC W. In this work, we were able to form harder BCC W by having a lower sputtering pressure (0.27 Pa compared to the 1.3 Pa of Ref [184]). The transition of metastable β-W to BCC W can also be done by heat treatment of the thin films at high temperatures (~800 K) for more than one hour, which is a time and energy consuming process [184].

5.1.4 Conclusions

In the present study, the correlation between the elemental composition, microstructure and mechanical properties of the co-sputtered Ni-W thin films was thoroughly investigated. A series of Ni-W alloy films with a thickness of ≤2.5 μm were co-deposited on silicon wafers with a thin layer of Ti (~20 nm). To study a wide range of Ni-W alloys, the sputtering time and power of Ni and W guns were optimized to fabricate thin films with desired thickness and composition (the W content varied from 0 to 100 at.% with ~20% increments). The prepared samples were characterized by energy dispersive spectroscopy (EDS), X-ray diffraction (XRD), scanning electron microscopy (SEM) to determine the elemental composition, solid phases and surface morphologies, respectively. Moreover, the atomic force microscopy (AFM) was performed to study the surface roughness of the samples, reported here for the first time. The hardness of the fabricated coatings was also measured using a microhardness tester by the Vickers method. Our results showed that the nanocrystalline structure, surface morphology, surface roughness and hardness of the Ni-W thin films are dominated by the W content. Based on the results, samples containing up to 20 at.% W had a nanocrystalline structure, for which the hardness would increase with a slope of 0.17 by the addition of W. Furthermore, samples having 39 to 55 at.% W composed an amorphous phase of Ni-W. Although the hardness was less sensitive to the W content

(H_V~0.07c) due to the presence of the amorphous phase in this region, it still increased by adding more W. The lowest surface roughness, *RMS* of 0.1 nm, belonged to two samples in this group having 39 and 55 at.% W. When the W content increased to 79-100 at.%, the nanocrystalline phase re-formed, the surface features were refined and the hardness also increased significantly. Finally, a high hardness of 21.9±2.0 GPa (Ni-79 at.%W) was achieved by controlling the sputtering power and pressure, without further heat treatment.

5.2 Improving the Non-Wettability of Ni-W Thin Films Using AKD

5.2.1 Introduction

The presence of moisture or water droplets is one of the most challenging issues in micro-electro-mechanical systems (MEMS). Due to the high wettability of the components used in MEMS, when a water droplet is introduced into the system, it completely spreads through the whole device and sticks to the components. This phenomenon can significantly affect the performance of electronic devices and reduce their lifespan by causing severe damages. One efficient way to solve this issue is coating the components with a thin hydrophobic layer to repel the water droplets and reduce the moisture [214]. In the present work, we used alkyl ketene dimer (AKD) to fabricate a thin layer of non-wettable material on nickel-tungsten thin films, as one of the potential components used in this industry [215]. To do so, we coated the Ni-79 at.% W thin film, which was the hardest sample according to the results of section 5.1.3, with a very thin layer of alkyl ketene dimer (AKD).

5.2.2 Experimental Procedure

In order to fabricate a very thin layer of AKD, we used a solution of 5 weight percent (wt. %) AKD in n-hexane (>95.0%, Sigma-Aldrich, USA). First, 0.328 gr of AKD pellets (the same AKD pellets from Chapter 2) were dissolved in a specific amount of solvent at room temperature. Then, the solution was stirred with a magnetic stirrer for 2 min to become completely homogeneous. Finally,

we immersed the Ni-W thin film, containing 79 at.% W, in the solution for a few seconds. The AKD solution on the substrate got dried at room temperature after one minute. Note that we reduced the thickness of the AKD layer as much as possible to avoid any interferes with the surface hardness of the substrates. In order to study the influence of the AKD coatings on the wetting properties of the Ni-W thin film, the static, advancing and receding contact angles were measured at 9 randomly-chosen points of both treated and untreated substrates using a goniometer (DSA25E, Krüss, Germany).

5.2.3 Results

Figure 5.5 shows a sessile water droplet having a volume of 5 µl on the treated (left) and untreated (right) Ni-W thin film. It is seen that the thin layer of AKD has improved the static contact angle of the surface from 89.5 to 108.5°. The reason for not reaching higher contact angles similar to Chapter 2 is attributed to the fact that the wetting properties of the AKD coatings are functions of the surface roughness and morphology. When the thickness of the AKD layer decreases, it is less likely to develop enough micro-textures on the surface to trap air pockets. Consequently, having fewer surface air pockets results in an increase in the solid-liquid interfacial area. As it was previously shown in Chapter 1, contact angle decreases with an increase in the solid-liquid interfacial area.

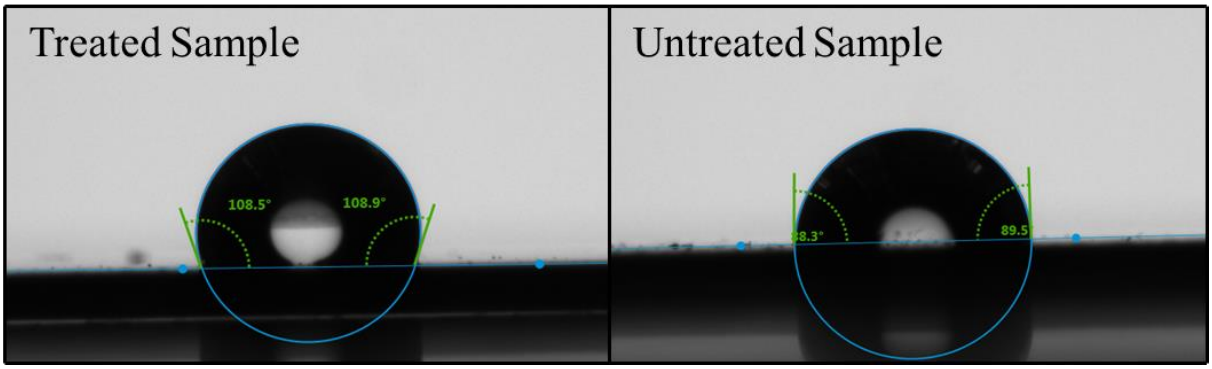

Figure 5.5. Static contact of a water droplet having a volume of 5 µl on the untreated Ni-79 at.% W thin film (right) and treated sample with 5 wt.% AKD solution in n-hexane (left).

Table 5.3 shows the average values of the static, advancing and receding contact angles of the untreated silicon wafer as the reference sample and Ni-79 at.% W sample, before and after treatment with the 5 wt.% solution of AKD in n-hexane. It is seen that not only has the AKD coating enhanced the static and dynamic contact angles of the Ni-W thin film, but it has also improved the uniformity of the samples. For example, by coating the Ni-W thin film with this solution, the receding contact angle of the sample has increased from 81.26 to 100.53°. Additionally, the standard deviation of the same case has decreased from 5.10 to 1.35°. This shows that by coating the surface with a very thin layer of AKD, the surface of the treated substrate becomes more uniform than the untreated one.

Table 5.3. Static, advancing and receding contact angles of untreated silicon wafer, untreated Ni-79 at.% W and treated Ni-79 at.% W with the 5 wt.% solution of AKD in n-hexane

Sample	Static contact angle (°)	Advancing contact angle (°)	Receding contact angle (°)
Untreated Silicon	98.60±2.75	99.59±2.20	90.05±6.09
Ni-79 at.% W (untreated)	92.56±3.72	93.55±3.57	81.26±5.10
Ni-79 at.% W (treated)	108.68±3.39	110.72±2.32	100.53±1.35

Chapter 6. Concluding Remarks and Future Directions

6.1 Conclusions

A facile method has been presented in this work to reduce the curing time of alkyl ketene dimer (AKD) from 4-6 days to less than 10 min. Other studies have addressed this issue by utilizing expensive materials, complex methods, non-eco-friendly compounds and highly toxic solvents (see Table A1). However, our method is straightforward, inexpensive and basic, where only a green chemical is used to address this issue without any post-curing steps. It has been shown that the surface morphology of the freshly solidified AKD, prepared from molten AKD at 40 °C, is completely smooth with no distinguished micro-textures. When the same sample is treated with ethanol, its surface morphology transforms to a porous structure with numerous micro-textures, resembling air pockets on the surface. This results in a reduction in the solid-liquid interfacial area, a significant increase in the contact angle and superhydrophobicity of the substrate. Additionally, the influence of the melt time and temperature on the wetting properties of the fabricated coatings was investigated. According to the results, as the melt time and temperature increased to 6 hr and 70°C, respectively, the advancing and receding contact angles reached their maximum value of 160.5 and 158.5°. This method was also shown to be working with other organic solvents, including methanol and isopropanol. As a proof of concept, this technique was applied to various materials, including glass slides, standard paper and co-sputtered nickel-tungsten thin films. It was seen that in all cases, the contact angle increased by 20 to 80%.

In the next step, a detailed investigation on the influence of physicochemical properties of surfactants, as commonly used additives in the industry, on the dynamic behavior of droplets impinging on surfaces of various wettabilities was given in Chapter 3. The Weber number of the impinging droplets was altered in the range of ~6 to 353. Our results showed that the presence of

surfactant molecules in the solutions always promotes a larger wetting area. As the non-wettability of the substrates decreases (from superhydrophobic to hydrophilic substrates), the enlarged wetting area caused by the surfactants becomes more noticeable. Additionally, the dynamic behavior of the surfactant-laden droplets is notably dependent on the concentration, molecular weight and ionic nature of the surfactants. When the concentration increases or molecular weight decreases, due to the increase in the energy dissipation of the system, the surfactant-laden droplets show weaker oscillations in the retraction phase. However, there was an exception for the cationic solution, which might be due to the interaction between the positive heads of the surfactant molecules with the negatively charged sites of the superhydrophobic AKD. This type of interaction leads to exposure of the hydrophobic tails of surfactants toward the air, resulting in an enhancement in the non-wettability of the coatings. Furthermore, it was shown that surfactants molecules hinder the ability of the droplets to minimize their wetting area and detach from the substrate in the retraction phase by dissolving the air pockets beneath the droplet and increasing the solid-liquid interfacial area.

Ultimately, the impact dynamics and freezing of these solutions were comprehensively studied at subzero temperatures of –10 to –30 °C using superhydrophobic AKD substrates. Our results showed that the temperature-dependent viscosity of the solutions plays a vital role in the dynamic behavior of the droplets. As the temperature decreases, the maximum spreading factor decreases and the final wetting area of the droplet increases due to the enhanced viscous effects. Regarding the influence of physicochemical properties of surfactants on the freezing behavior of the droplets, it was shown that surfactant-laden droplets generally freeze faster than pure water. This faster freezing is due to the higher heat transfer rate of the surfactant-laden droplets with the substrates due to having a larger solid-liquid interfacial area than pure water droplets and dissolving the

insulating air pockets existing on the superhydrophobic surface. It is worth mentioning that an extraordinary freezing delay was seen for the cationic solutions at –20 and –30 °C. This might be due to the different orientations of their molecules compared to the other surfactants. This type of orientation, where the molecules are arranged on the surface with their heads down, leads to an increase in the energetic barrier of the heterogeneous ice nucleation. This phenomenon might happen due to the hydrophobization of the substrate, preservation of more air pockets on the surface and formation of an insulating layer on the solid-liquid interface. Furthermore, regardless of the physicochemical properties of the surfactants, the presence of the surfactants molecules assists the heterogeneous freezing of the droplets at all subzero temperatures.

6.2 Future Works

In Chapter 2, we reduced the curing time of AKD from 4-6 days to lower than 10 min by treating the freshly solidified AKD, prepared from molten AKD at 40 °C, with ethanol. We were able to increase the contact angle of the coatings by approximately 80%. Following the work we presented here, it would be scientifically very interesting to further investigate the mechanism of this reaction by testing the effect of ethanol on the colloidal properties of AKD in the solution. Since this approach is very simple and viable for scale up, it would also be interesting to study other polymers and substrates with this method to tailor desirable morphologies for specific applications.

We also studied the influence of physicochemical properties of surfactants on the impact dynamics of the droplets. It was shown that the molecular weight of the surfactants has a key role in determining the impact outcomes and impact dynamics of the droplets. In the following of the presented work in Chapter 3, it would be interesting to eliminate the other governing parameters, including the ionic nature and chemical structure of the surfactants from the experiments and only focus on the molecular weight as a critical parameter affecting this phenomenon. To do so, one

can prepare the surfactants solutions of the same family with a similar chemical structure and ionic nature but different molecular weights. Then, by conducting a series of systematic experiments, it is possible to accurately understand the relationship between the molecular weight and impact parameters (e.g., maximum spreading factor) of surfactant-laden droplets.

Furthermore, in all our cases, the impact substrate was flat. It has been shown in previous studies [8] that decorating the superhydrophobic surfaces with cylindrical macrotextures influences the retraction behavior of water droplets. Since surfactant-laden droplets have a time-dependent surface tension, any acceleration or delay in the contact time or spreading and retraction time of the droplets might have remarkable effects on their impact dynamics. As a result, it would be interesting to study the dynamic behavior of surfactant-laden droplets impinging on flat and curved surfaces having different textures.

In Chapter 4, we studied the influence of the physicochemical properties of the surfactants on the impact dynamics and freezing behavior of the droplets at subzero temperatures. In our case, due to the limitations we had with the experimental apparatus, we were not able to adjust the falling height of the droplets to alter the impact velocity. It also has been shown in Chapter 3 that impact dynamics and impact outcomes of the surfactant-laden droplets at room temperature are a function of their initial kinetic energies. Consequently, it would be interesting to study the influences of this parameter on the impact dynamics, impact outcomes and freezing behavior of surfactant-laden droplets at subzero temperatures.

Chapter 7. References

[1] T. Young, III. An essay on the cohesion of fluids, Philos. Trans. R. Soc. London. (1805) 65–87.

[2] A. Marmur, The lotus effect: superhydrophobicity and metastability, Langmuir. 20 (2004) 3517–3519.

[3] A. Cassle, B.S. B D, Wettability of porous surfaces, Trans. Faraday Soc. 40 (1944) 546–551.

[4] S. Mettu, M.K. Chaudhury, Stochastic relaxation of the contact line of a water drop on a solid substrate subjected to white noise vibration: Roles of hysteresis, Langmuir. 26 (2010) 8131–8140. https://doi.org/10.1021/la9044094.

[5] A. Lafuma, D. Quéré, Superhydrophobic states, Nat. Mater. 2 (2003) 457–460. https://doi.org/10.1038/nmat924.

[6] R. Mohammadi, J. Wassink, A. Amirfazli, Effect of surfactants on wetting of super-hydrophobic surfaces, Langmuir. (2004). https://doi.org/10.1021/la049268k.

[7] D. Quéré, Non-sticking drops, Reports Prog. Phys. 68 (2005) 2495–2532. https://doi.org/10.1088/0034-4885/68/11/R01.

[8] M. Abolghasemibizaki, R. Mohammadi, Journal of Colloid and Interface Science Droplet impact on superhydrophobic surfaces fully decorated with cylindrical macrotextures, J. Colloid Interface Sci. 509 (2018) 422–431. https://doi.org/10.1016/j.jcis.2017.09.030.

[9] X. Deng, L. Mammen, H.-J. Butt, D. Vollmer, Candle Soot as a Template for a Transparent Robust Superamphiphobic Coating, Science (80-.). 335 (2012) 67–70. https://doi.org/10.1126/science.1207115.

[10] R. Fürstner, W. Barthlott, C. Neinhuis, P. Walzel, Wetting and self-cleaning properties of artificial superhydrophobic surfaces, Langmuir. 21 (2005) 956–961. https://doi.org/10.1021/la0401011.

[11] R. Blossey, C. Scientifique, Self-cleaning surfaces — virtual realities, (2003) 301–306.

[12] A.R. Esmaeili, N. Mir, R. Mohammadi, A Facile, Fast, and Low-Cost Method for Fabrication of Micro/Nano-Textured Superhydrophobic Surfaces, J. Colloid Interface Sci. 573 (2020) 317–327. https://doi.org/https://doi.org/10.1016/j.jcis.2020.04.027.

[13] P. Wang, D. Zhang, R. Qiu, B. Hou, Super-hydrophobic film prepared on zinc as corrosion barrier, Corros. Sci. 53 (2011) 2080–2086. https://doi.org/10.1016/j.corsci.2011.02.025.

[14] Y. Wei, L. Hongtao, Z. Wei, Preparation of anti-corrosion superhydrophobic coatings by an Fe-based micro/nano composite electro-brush plating and blackening process, RSC Adv. 5 (2015) 103000–103012. https://doi.org/10.1039/c5ra15640h.

[15] S. Farhadi, M. Farzaneh, S.A. Kulinich, Anti-icing performance of superhydrophobic surfaces, Appl. Surf. Sci. 257 (2011) 6264–6269. https://doi.org/10.1016/j.apsusc.2011.02.057.

[16] K.D. Esmeryan, A.H. Bressler, C.E. Castano, C.P. Fergusson, R. Mohammadi, Applied Surface Science Rational strategy for the atmospheric icing prevention based on chemically functionalized carbon soot coatings, Appl. Surf. Sci. 390 (2016) 452–460. https://doi.org/10.1016/j.apsusc.2016.08.101.

[17] D.G. Venkateshan, M.M. Amrei, A.A. Hemeda, Z. Cullingsworth, J. Corbett, H. Vahedi Tafreshi, Failure pressures and drag reduction benefits of superhydrophobic wire screens, Colloids Surfaces A Physicochem. Eng. Asp. 511 (2016) 247–254. https://doi.org/10.1016/j.colsurfa.2016.09.087.

[18] J.L. Laforte, M.A. Allaire, J. Laflamme, State-of-the-art on power line de-icing, Atmos. Res. 46 (1998) 143–158. https://doi.org/10.1016/S0169-8095(97)00057-4.

[19] O. Parent, A. Ilinca, Anti-icing and de-icing techniques for wind turbines: Critical review, Cold Reg. Sci. Technol. 65 (2011) 88–96. https://doi.org/10.1016/j.coldregions.2010.01.005.

[20] L. Mishchenko, B. Hatton, V. Bahadur, J.A. Taylor, T. Krupenkin, J. Aizenberg, Design of ice-free nanostructured surfaces based on repulsion of impacting water droplets, ACS Nano. 4 (2010) 7699–7707. https://doi.org/10.1021/nn102557p.

[21] M.I. Jamil, X. Zhan, F. Chen, D. Cheng, Q. Zhang, Durable and Scalable Candle Soot Icephobic Coating with Nucleation and Fracture Mechanism, ACS Appl. Mater. Interfaces. 11 (2019) 31532–31542. https://doi.org/10.1021/acsami.9b09819.

[22] Y. Kwon, N. Patankar, J. Choi, J. Lee, Design of surface hierarchy for extreme hydrophobicity, Langmuir. 25 (2009) 6129–6136. https://doi.org/10.1021/la803249t.

[23] J. Zimmermann, F.A. Reifler, G. Fortunato, L.C. Gerhardt, S. Seeger, A simple, one-step approach to durable and robust superhydrophobic textiles, Adv. Funct. Mater. 18 (2008) 3662–3669. https://doi.org/10.1002/adfm.200800755.

[24] S.S. Latthe, H. Imai, V. Ganesan, A.V. Rao, Superhydrophobic silica films by sol-gel co-precursor method, Appl. Surf. Sci. 256 (2009) 217–222. https://doi.org/10.1016/j.apsusc.2009.07.113.

[25] A. Moghadam, H. Vahedi Tafreshi, On liquid bridge adhesion to fibrous surfaces under normal and shear forces, Colloids Surfaces A Physicochem. Eng. Asp. 589 (2020) 124473. https://doi.org/10.1016/j.colsurfa.2020.124473.

[26] M. Jamali, A. Moghadam, H.V. Tafreshi, B. Pourdeyhimi, Droplet adhesion to hydrophobic fibrous surfaces, Appl. Surf. Sci. 456 (2018) 626–636. https://doi.org/10.1016/j.apsusc.2018.06.136.

[27] A. Moghadam, N. Ojaghlou, D. Bratko, H. V Tafreshi, A molecular dynamics approach to modeling effects of detaching force on the compound droplet residue on spherical surfaces, in: APS Div. Fluid Dyn. Meet. Abstr., 2020: pp. Z01-009.

[28] A. Moghadam, M. Jamali, D.G. Venkateshan, H.V. Tafreshi, B. Pourdeyhimi, A new approach to modeling liquid intrusion in hydrophobic fibrous membranes with heterogeneous wettabilities, Colloids Surfaces A Physicochem. Eng. Asp. 558 (2018)

154–163.

[29] A. Moghadam, S.H. Yousefi, H.V. Tafreshi, B. Pourdeyhimi, Characterizing nonwoven materials via realistic microstructural modeling, Sep. Purif. Technol. 211 (2019) 602–609.

[30] N. Ojaghlou, A. Moghadam, D. Bratko, H. V Tafreshi, A. Luzar, Physics behind the droplet detachment from a surface, in: APS Div. Fluid Dyn. Meet. Abstr., 2020: pp. Z01-007.

[31] K. Okumura, F. Chevy, D. Richard, D. Quéré, C. Clanet, Water spring: A model for bouncing drops, Europhys. Lett. 62 (2003) 237–243. https://doi.org/10.1209/epl/i2003-00340-1.

[32] D. Banks, C. Ajawara, R. Sanchez, H. Surti, G. Aguilar, Effects of liquid and surface characteristics on oscillation behavior of droplets upon impact, At. Sprays. 24 (2014) 895–913.

[33] R.M. Manglik, M.A. Jog, S.K. Gande, V. Ravi, Damped harmonic system modeling of post-impact drop-spread dynamics on a hydrophobic surface, Phys. Fluids. 25 (2013). https://doi.org/10.1063/1.4819243.

[34] D. Deb, N.L. Brahmbhatt, Review of yield increase of solar panels through soiling prevention, and a proposed water-free automated cleaning solution, Renew. Sustain. Energy Rev. 82 (2018) 3306–3313.

[35] K.A. Moharram, M.S. Abd-Elhady, H.A. Kandil, H. El-Sherif, Influence of cleaning using water and surfactants on the performance of photovoltaic panels, Energy Convers. Manag. 68 (2013) 266–272.

[36] A.A. Pawar, V. V Bhosale, V.S. Jagadale, Enhancement of thermal performance of wickless heat pipe solar collector with surfactant added nanofluid, in: Techno-Societal 2018, Springer, 2020: pp. 397–406.

[37] L. Oberli, D. Caruso, C. Hall, M. Fabretto, P.J. Murphy, D. Evans, Condensation and freezing of droplets on superhydrophobic surfaces, Adv. Colloid Interface Sci. 210 (2014) 47–57. https://doi.org/10.1016/j.cis.2013.10.018.

[38] J.P. Hindmarsh, A.B. Russell, X.D. Chen, Experimental and numerical analysis of the temperature transition of a suspended freezing water droplet, Int. J. Heat Mass Transf. 46 (2003) 1199–1213. https://doi.org/10.1016/S0017-9310(02)00399-X.

[39] S. Shibuichi, T. Onda, N. Satoh, K. Tsujii, Super water-repellent surfaces resulting from fractal structure, J. Phys. Chem. 100 (1996) 19512–19517. https://doi.org/10.1021/jp9616728.

[40] T. Minami, H. Mayama, S. Nakamura, S. Yokojima, J.W. Shen, K. Tsujii, Formation mechanism of fractal structures on wax surfaces with reference to their super water-repellency, Soft Matter. 4 (2007) 140–144. https://doi.org/10.1039/b712938f.

[41] W. Jia, H.-H. Qiu, Experimental investigation of droplet dynamics and heat transfer in spray cooling, Exp. Therm. Fluid Sci. 27 (2003) 829–838.

[42] Y. Son, C. Kim, D.H. Yang, D.J. Ahn, Spreading of an inkjet droplet on a solid surface with a controlled contact angle at low Weber and Reynolds numbers, Langmuir. 24 (2008) 2900–2907.

[43] A.R. Esmaeili, B. Sajadi, M. Akbarzadeh, Numerical simulation of ellipsoidal particles deposition in the human nasal cavity under cyclic inspiratory flow, J. Brazilian Soc. Mech. Sci. Eng. 42 (2020) 243. https://doi.org/10.1007/s40430-020-02345-y.

[44] M.D. Manniello, S. Hosseini, A. Alfaifi, A.R. Esmaeili, A. V. Kolanjiyil, R. Walenga, A. Babiskin, D. Sandell, R. Mohammadi, T. Schuman, M. Hindle, L. Golshahi, In vitro evaluation of regional nasal drug delivery using multiple anatomical nasal replicas of adult human subjects and two nasal sprays, Int. J. Pharm. 593 (2021) 120103. https://doi.org/10.1016/j.ijpharm.2020.120103.

[45] J. Rakowska, K. Radwan, B. Porycka, K. Prochaska, Experimental study on surface activity of surfactants on their ability to cleaning oil contaminations, J. Clean. Prod. 144 (2017) 437–447.

[46] A.L. Yarin, Drop impact dynamics: splashing, spreading, receding, bouncing…, Annu. Rev. Fluid Mech. 38 (2006) 159–192.

[47] N. Imaz, J.A. Diez, E. Pellicer, J. Sort, H. Grande, E. Garcia-Lecina, Thermal treatment effect on the mechanical, tribological and corrosion properties of Ni–W alloy obtained by direct and pulse plating electrodeposition, Trans. IMF. 95 (2017) 31–38.

[48] L.M. Chang, Z.T. Wang, S.Y. Shi, W. Liu, Study on microstructure and properties of electrodeposited Ni–W alloy coating with glycolic acid system, J. Alloys Compd. 509 (2011) 1501–1504.

[49] J. Druga, M. Kašiarová, E. Dobročka, M. Zemanová, Corrosion and tribological properties of nanocrystalline pulse electrodeposited Ni–W alloy coatings, Trans. IMF. 95 (2017) 39–45. https://doi.org/10.1080/00202967.2017.1262117.

[50] M.H. Allahyarzadeh, M. Aliofkhazraei, A.R. Rezvanian, V. Torabinejad, A.R. Sabour Rouhaghdam, Ni-W electrodeposited coatings: Characterization, properties and applications, Surf. Coatings Technol. 307 (2016) 978–1010. https://doi.org/10.1016/j.surfcoat.2016.09.052.

[51] H. Alimadadi, M. Ahmadi, M. Aliofkhazraei, S.R. Younesi, Corrosion properties of electrodeposited nanocrystalline and amorphous patterned Ni – W alloy, Mater. Des. 30 (2009) 1356–1361. https://doi.org/10.1016/j.matdes.2008.06.036.

[52] K.D. Esmeryan, C.E. Castano, A.H. Bressler, M. Abolghasemibizaki, R. Mohammadi, Applied Surface Science Rapid synthesis of inherently robust and stable superhydrophobic carbon soot coatings, Appl. Surf. Sci. 369 (2016) 341–347. https://doi.org/10.1016/j.apsusc.2016.02.089.

[53] T.T. Isimjan, T. Wang, S. Rohani, A novel method to prepare superhydrophobic, UV resistance and anti-corrosion steel surface, Chem. Eng. J. 210 (2012) 182–187. https://doi.org/10.1016/j.cej.2012.08.090.

[54] A. Criscione, I. V. Roisman, S. Jakirlić, C. Tropea, Towards modelling of initial and final stages of supercooled water solidification, Int. J. Therm. Sci. 92 (2015) 150–161. https://doi.org/10.1038/ncomms1630.

[55] K.D. Esmeryan, A.H. Bressler, C.E. Castano, C.P. Fergusson, R. Mohammadi, Rational strategy for the atmospheric icing prevention based on chemically functionalized carbon soot coatings, Appl. Surf. Sci. 390 (2016) 452–460. https://doi.org/10.1016/j.apsusc.2016.08.101.

[56] L. Zhang, H. Li, L.H. Weng, G.X. Jin, Isomers of cyclometalated macrocycles constructed through olefinic C-H activation, Organometallics. 33 (2014) 587–593. https://doi.org/10.1021/om4011559.

[57] D. Quéré, Rough ideas on wetting, Phys. A Stat. Mech. Its Appl. 313 (2002) 32–46. https://doi.org/10.1016/S0378-4371(02)01033-6.

[58] S.C. Cho, Y.C. Hong, H.S. Uhm, Hydrophobic coating of carbon nanotubes by CH4 glow plasma at low pressure, and their resulting wettability, J. Mater. Chem. 17 (2007) 232–237. https://doi.org/10.1039/b611368k.

[59] G. Zhang, D. Wang, Z.Z. Gu, H. Mchwald, Fabrication of superhydrophobic surfaces from binary colloidal assembly, Langmuir. 21 (2005) 9143–9148. https://doi.org/10.1021/la0511945.

[60] Z. Guo, F. Zhou, J. Hao, W. Liu, Stable biomimetic super-hydrophobic engineering materials, J. Am. Chem. Soc. 127 (2005) 15670–15671. https://doi.org/10.1021/ja0547836.

[61] I.A. Larmour, S.E.J. Bell, G.C. Saunders, Remarkably simple fabrication of superhydrophobic surfaces using electroless galvanic deposition, Angew. Chemie - Int. Ed. 46 (2007) 1710–1712. https://doi.org/10.1002/anie.200604596.

[62] M. Ma, Y. Mao, M. Gupta, K.K. Gleason, G.C. Rutledge, Superhydrophobic fabrics produced by electrospinning and chemical vapor deposition, Macromolecules. 38 (2005) 9742–9748. https://doi.org/10.1021/ma0511189.

[63] H. Wang, J. Ding, Y. Xue, X. Wang, T. Lin, Superhydrophobic fabrics from hybrid silica sol-gel coatings: Structural effect of precursors on wettability and washing durability, J. Mater. Res. 25 (2010) 1336–1343. https://doi.org/10.1557/jmr.2010.0169.

[64] H. Wang, J. Fang, T. Cheng, J. Ding, L. Qu, L. Dai, X. Wang, T. Lin, One-step coating of fluoro-containing silica nanoparticles for universal generation of surface superhydrophobicity, Chem. Commun. (2008) 877–879. https://doi.org/10.1039/b714352d.

[65] H. Yang, Y. Deng, Preparation and physical properties of superhydrophobic papers, J. Colloid Interface Sci. 325 (2008) 588–593. https://doi.org/10.1016/j.jcis.2008.06.034.

[66] W. Zhang, P. Lu, L. Qian, H. Xiao, Fabrication of superhydrophobic paper surface via wax mixture coating, Chem. Eng. J. 250 (2014) 431–436. https://doi.org/10.1016/j.cej.2014.04.050.

[67] X. Zhang, W. Batchelor, W. Shen, Building Dual-Scale Roughness Using Inorganic Pigments for Fabrication of Superhydrophobic Paper, Ind. Eng. Chem. Res. 56 (2017) 3618–3628. https://doi.org/10.1021/acs.iecr.7b00225.

[68] N.N. Hamidon, Y. Hong, G.I. Salentijn, E. Verpoorte, Water-based alkyl ketene dimer ink for user-friendly patterning in paper microfluidics, Anal. Chim. Acta. 1000 (2018) 180–190. https://doi.org/10.1016/j.aca.2017.10.040.

[69] L. Yang, S. Lu, J. Li, F. Zhang, R. Cha, Nanocrystalline cellulose-dispersed AKD emulsion for enhancing the mechanical and multiple barrier properties of surface-sized paper, Carbohydr. Polym. 136 (2015) 1035–1040. https://doi.org/10.1016/j.carbpol.2015.10.011.

[70] Q. Zhao, W. Liu, G. Li, L.A. Lucia, H. Wang, D. Yu, Unique alkyl ketene dimer Pickering-based dispersions: Preparation and application to paper sizing, J. Appl. Polym. Sci. 135 (2018) 1–9. https://doi.org/10.1002/app.45730.

[71] L.Q. Huang, X.M. Song, L.Q. Cui, S.S. Gao, F.S. Chen, S.L. Wang, J.L. Liu, Preparation and characterization of AKD sizing agent by "one-pot cooking," Nord. Pulp Pap. Res. J. 33 (2018) 317–326. https://doi.org/10.1515/npprj-2018-3021.

[72] L. Li, D.J. Neivandt, The mechanism of alkyl ketene dimer (AKD) sizing on cellulose model films studied by sum frequency generation vibrational spectroscopy, Cellulose. 26 (2019) 3415–3435. https://doi.org/10.1007/s10570-019-02295-2.

[73] C.-H. Xue, S.-T. Jia, J. Zhang, J.-Z. Ma, Large-area fabrication of superhydrophobic surfaces for practical applications: an overview, Sci. Technol. Adv. Mater. 11 (2010) 033002. https://doi.org/10.1088/1468-6996/11/3/033002.

[74] N.F. Himma, N. Prasetya, S. Anisah, I.G. Wenten, Superhydrophobic membrane: Progress in preparation and its separation properties, Rev. Chem. Eng. 35 (2019) 211–238. https://doi.org/10.1515/revce-2017-0030.

[75] S. Wang, K. Liu, X. Yao, L. Jiang, Bioinspired surfaces with superwettability: New insight on theory, design, and applications, Chem. Rev. 115 (2015) 8230–8293. https://doi.org/10.1021/cr400083y.

[76] C. Quan, O. Werner, L. Wågberg, C. Turner, Generation of superhydrophobic paper surfaces by a rapidly expanding supercritical carbon dioxide-alkyl ketene dimer solution, J. Supercrit. Fluids. 49 (2009) 117–124. https://doi.org/10.1016/j.supflu.2008.11.015.

[77] O. Werner, C. Quan, C. Turner, B. Pettersson, L. Wågberg, Properties of superhydrophobic paper treated with rapid expansion of supercritical CO2 containing a crystallizing wax, Cellulose. 17 (2010) 187–198. https://doi.org/10.1007/s10570-009-9374-1.

[78] P. Olin, P. Ollin, C. Hyll, L. Ovaskainen, M. Ruda, O. Schmidt, C. Turner, L. Wågberg, Development of a semicontinuous spray process for the production of superhydrophobic coatings from supercritical carbon dioxide solutions, Ind. Eng. Chem. Res. 54 (2015) 1059–1067. https://doi.org/10.1021/ie503798k.

[79] P. Olin, S.B. Lindström, T. Pettersson, L. Wågberg, Water drop friction on superhydrophobic surfaces, Langmuir. 29 (2013) 9079–9089. https://doi.org/10.1021/la401152b.

[80] B.H. Hutton, I.H. Parker, A surface study of cellulose fibres impregnated with alkyl ketene dimers via subcritical and supercritical carbon dioxide, Colloids Surfaces A Physicochem. Eng. Asp. 334 (2009) 59–65. https://doi.org/10.1016/j.colsurfa.2008.10.001.

[81] X. Han, M. Poliakoff, Continuous reactions in supercritical carbon dioxide: Problems, solutions and possible ways forward, Chem. Soc. Rev. 41 (2012) 1428–1436. https://doi.org/10.1039/c2cs15314a.

[82] T. Onda, S. Shibuichi, N. Satoh, K. Tsujii, Super-Water-Repellent Fractal Surfaces, Langmuir. 12 (1996) 2125–2127. https://doi.org/10.1021/la950418o.

[83] W. Fang, H. Mayama, K. Tsujii, Formation mechanism of super water-repellent fractal surfaces of alkylketene dimer, Colloids Surfaces A Physicochem. Eng. Asp. 316 (2008) 258–265. https://doi.org/10.1016/j.colsurfa.2007.09.010.

[84] W. Shen, I.H. Parker, A preliminary study of the spreading of AKD in the presence of capillary structures, J. Colloid Interface Sci. 240 (2001) 172–181. https://doi.org/10.1006/jcis.2001.7593.

[85] K.D. Esmeryan, C.E. Castano, A.H. Bressler, C.P. Fergusson, R. Mohammadi, Single-step flame synthesis of carbon nanoparticles with tunable structure and chemical reactivity, RSC Adv. 6 (2016) 61620–61629. https://doi.org/10.1039/c6ra06436a.

[86] K.D. Esmeryan, C.E. Castano, R. Mohammadi, Interactions of superhydrophobic carbon soot coatings with short alkyl chain alcohols and fluorocarbon solutions, Colloids Surfaces A. 529 (2017) 715–724. https://doi.org/10.1016/j.colsurfa.2017.06.067.

[87] M. Abolghasemibizaki, R.L. Mcmasters, R. Mohammadi, Journal of Colloid and Interface Science Towards the shortest possible contact time : Droplet impact on cylindrical superhydrophobic surfaces structured with macro-scale features, J. Colloid Interface Sci. 521 (2018) 17–23. https://doi.org/10.1016/j.jcis.2018.03.005.

[88] P.A. Levkin, F. Svec, J.M.J. Fréchet, Porous polymer coatings: a versatile approach to superhydrophobic surfaces, Adv. Funct. Mater. 19 (2009) 1993–1998.

[89] S. Kato, A. Sato, Micro/nanotextured polymer coatings fabricated by UV curing-induced phase separation: creation of superhydrophobic surfaces, J. Mater. Chem. 22 (2012) 8613–8621.

[90] J. Park, S.A. Saba, M.A. Hillmyer, D.-C. Kang, M. Seo, Effect of homopolymer in polymerization-induced microphase separation process, Polymer (Guildf). 126 (2017) 338–351.

[91] S.A. Saba, M.P.S. Mousavi, P. Bühlmann, M.A. Hillmyer, Hierarchically porous polymer monoliths by combining controlled macro-and microphase separation, J. Am. Chem. Soc. 137 (2015) 8896–8899.

[92] S. Lee, M. Choi, S. Park, H. Jung, B. Yoo, Mechanical properties of electrodeposited Ni-W ThinFilms with alternate W-rich and W-poor multilayers, Electrochim. Acta. 153 (2015) 225–231. https://doi.org/10.1016/j.electacta.2014.11.190.

[93] C.R. Crick, I.P. Parkin, Preparation and characterisation of super-hydrophobic surfaces, Chem. - A Eur. J. 16 (2010) 3568–3588. https://doi.org/10.1002/chem.200903335.

[94] L. Barbieri, E. Wagner, P. Hoffmann, Water wetting transition parameters of perfluorinated substrates with periodically distributed flat-top microscale obstacles, Langmuir. 23 (2007) 1723–1734. https://doi.org/10.1021/la0617964.

[95] W. Fang, H. Mayama, K. Tsujii, Spontaneous formation of fractal structures on triglyceride surfaces with reference to their super water-repellent properties, J. Phys. Chem. B. 111 (2007) 564–571. https://doi.org/10.1021/jp065589o.

[96] K. Tsujii, Fractal Materials and Their Functional Properties, Polym. J. 40 (2008) 785–799. https://doi.org/10.1295/polymj.pj2008053.

[97] L. Ejenstam, L. Ovaskainen, I. Rodriguez-Meizoso, L. Wågberg, J. Pan, A. Swerin, P.M. Claesson, The effect of superhydrophobic wetting state on corrosion protection - The AKD example, J. Colloid Interface Sci. 412 (2013) 56–64. https://doi.org/10.1016/j.jcis.2013.09.006.

[98] W. Shen, H. Zhang, R. Ettl, Chemical composition of “AKD vapour” and its implication to AKD vapour sizing, Cellulose. 12 (2005) 641–652. https://doi.org/10.1007/s10570-005-9010-7.

[99] A. Russler, M. Wieland, M. Bacher, U. Henniges, P. Miethe, F. Liebner, A. Potthast, T. Rosenau, AKD-Modification of bacterial cellulose aerogels in supercritical CO 2, Cellulose. 19 (2012) 1337–1349. https://doi.org/10.1007/s10570-012-9728-y.

[100] Y. Rahmawan, L. Xu, S. Yang, Self-assembly of nanostructures towards transparent, superhydrophobic surfaces, J. Mater. Chem. A. 1 (2013) 2955–2969.

[101] S. Yu, F.L. Ng, K.C.C. Ma, A.A. Mon, F.L. Ng, Y.Y. Ng, Effect of porogenic solvent on the porous properties of polymer monoliths, J. Appl. Polym. Sci. 127 (2013) 2641–2647.

[102] L. Peng, Y. Meng, H. Li, Facile fabrication of superhydrophobic paper with improved physical strength by a novel layer-by-layer assembly of polyelectrolytes and lignosulfonates-amine, Cellulose. 23 (2016) 2073–2085. https://doi.org/10.1007/s10570-016-0910-5.

[103] B. Balu, V. Breedveld, D.W. Hess, Fabrication of “roll-off” and “sticky” superhydrophobic cellulose surfaces-via plasma processing, Langmuir. 24 (2008) 4785–4790. https://doi.org/10.1021/la703766c.

[104] W. Wirth, S. Storp, W. Jacobsen, Mechanisms controlling leaf retention of agricultural spray solutions, Pestic. Sci. 33 (1991) 411–420.

[105] J.C. Bird, R. Dhiman, H.M. Kwon, K.K. Varanasi, Reducing the contact time of a bouncing drop, Nature. 503 (2013) 385–388. https://doi.org/10.1038/nature12740.

[106] A. Gauthier, S. Symon, C. Clanet, D. Quéré, Water impacting on superhydrophobic macrotextures, Nat. Commun. 6 (2015) 2–7. https://doi.org/10.1038/ncomms9001.

[107] C.J. Patterson, S. Shiri, J.C. Bird, Macrotextured spoked surfaces reduce the residence time of a bouncing Leidenfrost drop, J. Phys. Condens. Matter. 29 (2017). https://doi.org/10.1088/1361-648X/aa4e8a.

[108] C. Josserand, S.T. Thoroddsen, Drop impact on a solid surface, Annu. Rev. Fluid Mech. 48 (2016) 365–391.

[109] I. V Roisman, R. Rioboo, C. Tropea, Normal impact of a liquid drop on a dry surface: model for spreading and receding, Proc. R. Soc. London. Ser. A Math. Phys. Eng. Sci. 458 (2002) 1411–1430.

[110] T. Mao, D.C.S. Kuhn, H. Tran, Spread and rebound of liquid droplets upon impact on flat surfaces, AIChE J. 43 (1997) 2169–2179.

[111] C. Ukiwe, D.Y. Kwok, On the maximum spreading diameter of impacting droplets on well-prepared solid surfaces, Langmuir. 21 (2005) 666–673.

[112] S. Chandra, C.T. Avedisian, On the collision of a droplet with a solid surface, Proc. R. Soc. London. Ser. A Math. Phys. Sci. 432 (1991) 13–41.

[113] Š. Šikalo, H.-D. Wilhelm, I. V Roisman, S. Jakirlić, C. Tropea, Dynamic contact angle of spreading droplets: Experiments and simulations, Phys. Fluids. 17 (2005) 62103.

[114] M. Bussmann, J. Mostaghimi, S. Chandra, On a three-dimensional volume tracking model of droplet impact, Phys. Fluids. 11 (1999) 1406–1417.

[115] N. Mourougou-Candoni, B. Prunet-Foch, F. Legay, M. Vignes-Adler, K. Wong, Retraction phenomena of surfactant solution drops upon impact on a solid substrate of low surface energy, Langmuir. 15 (1999) 6563–6574. https://doi.org/10.1021/la9901074.

[116] N. Mourougou-Candoni, B. Prunet-Foch, F. Legay, M. Vignes-Adler, K. Wong, Influence of dynamic surface tension on the spreading of surfactant solution droplets impacting onto a low-surface-energy solid substrate, J. Colloid Interface Sci. 192 (1997) 129–141. https://doi.org/10.1006/jcis.1997.4989.

[117] X. Zhang, O.A. Basaran, Dynamic surface tension effects in impact of a drop with a solid surface, J. Colloid Interface Sci. 187 (1997) 166–178. https://doi.org/10.1006/jcis.1996.4668.

[118] R. Crooks, J. Cooper-White, D. V. Boger, The role of dynamic surface tension and elasticity on the dynamics of drop impact, Chem. Eng. Sci. 56 (2001) 5575–5592. https://doi.org/10.1016/S0009-2509(01)00175-0.

[119] D. Bartolo, C. Josserand, D. Bonn, Retraction dynamics of aqueous drops upon impact on non-wetting surfaces, J. Fluid Mech. 545 (2005) 329–338. https://doi.org/10.1017/S0022112005007184.

[120] M. Pasandideh-Fard, Y.M. Qiao, S. Chandra, J. Mostaghimi, Capillary effects during droplet impact on a solid surface, Phys. Fluids. 8 (1996) 650–659.

https://doi.org/10.1063/1.868850.

[121] M. Aytouna, D. Bartolo, G. Wegdam, D. Bonn, S. Rafaï, Impact dynamics of surfactant laden drops: Dynamic surface tension effects, Exp. Fluids. 48 (2010) 49–57. https://doi.org/10.1007/s00348-009-0703-9.

[122] K.P. Gatne, M.A. Jog, R.M. Manglik, Surfactant-induced modification of low weber number droplet impact dynamics, Langmuir. 25 (2009) 8122–8130. https://doi.org/10.1021/la900625a.

[123] S.Y. Lin, A. Casandra, Y.Y. Margaretha, R.Y. Tsay, Impingement of Triton X-100 solution drops on paraffin film–Relaxation of surface dilational rate, J. Taiwan Inst. Chem. Eng. 92 (2018) 36–41. https://doi.org/10.1016/j.jtice.2018.02.016.

[124] M. Abolghasemibizaki, C.J. Robertson, C.P. Fergusson, R.L. McMasters, R. Mohammadi, Rolling viscous drops on a non-wettable surface containing both micro-and macro-scale roughness, Phys. Fluids. 30 (2018) 23105.

[125] R. Mohammadi, J. Wassink, A. Amirfazli, Effect of Surfactants on Wetting of Super-Hydrophobic Surfaces, (2004) 19512–19517.

[126] S.S. Dukhin, G. Kretzschmar, R. Miller, Dynamics of adsorption at liquid interfaces: theory, experiment, application, Elsevier, 1995.

[127] A.M. Poskanzer, F.C. Goodrich, Surface viscosity of sodium dodecyl sulfate solutions with and without added dodecanol, J. Phys. Chem. 79 (1975) 2122–2126. https://doi.org/10.1021/j100587a012.

[128] C. Huh, L.E. Scriven, Hydrodynamic model of steady movement of a solid/liquid/fluid contact line, J. Colloid Interface Sci. 35 (1971) 85–101.

[129] X. Wang, L. Chen, E. Bonaccurso, Comparison of spontaneous wetting and drop impact dynamics of aqueous surfactant solutions on hydrophobic polypropylene surfaces: scaling of the contact radius, Colloid Polym. Sci. 293 (2014) 257–265. https://doi.org/10.1007/s00396-014-3410-x.

[130] J.B. Lee, D. Derome, R. Guyer, J. Carmeliet, Modeling the Maximum Spreading of Liquid Droplets Impacting Wetting and Nonwetting Surfaces, Langmuir. 32 (2016) 1299–1308. https://doi.org/10.1021/acs.langmuir.5b04557.

[131] A. Sze, D. Erickson, L. Ren, D. Li, Zeta-potential measurement using the Smoluchowski equation and the slope of the current-time relationship in electroosmotic flow, J. Colloid Interface Sci. 261 (2003) 402–410. https://doi.org/10.1016/S0021-9797(03)00142-5.

[132] J.C.W. Corbett, F. McNeil-Watson, R.O. Jack, M. Howarth, Measuring surface zeta potential using phase analysis light scattering in a simple dip cell arrangement, Colloids Surfaces A Physicochem. Eng. Asp. 396 (2012) 169–176. https://doi.org/10.1016/j.colsurfa.2011.12.065.

[133] L. Chen, E. Bonaccurso, P. Deng, H. Zhang, Droplet impact on soft viscoelastic surfaces, Phys. Rev. E. 94 (2016) 63117.

[134] W. Thomson, Theory of vibration with applications, CrC Press, 2018.

[135] M. Abolghasemibizaki, N. Dilmaghani, R. Mohammadi, C.E. Castano, Viscous Droplet Impact on Nonwettable Textured Surfaces, Langmuir. 35 (2019) 10752–10761. https://doi.org/10.1021/acs.langmuir.9b01109.

[136] C. Antonini, A. Amirfazli, M. Marengo, Drop impact and wettability: From hydrophilic to superhydrophobic surfaces, Phys. Fluids. 24 (2012) 102104.

[137] Y.C. Jung, B. Bhushan, Dynamic effects of bouncing water droplets on superhydrophobic surfaces, Langmuir. 24 (2008) 6262–6269.

[138] P. Tsai, S. Pacheco, C. Pirat, L. Lefferts, D. Lohse, Drop impact upon micro-and nanostructured superhydrophobic surfaces, Langmuir. 25 (2009) 12293–12298.

[139] L. Chen, Y. Wang, X. Peng, Q. Zhu, K. Zhang, Impact Dynamics of Aqueous Polymer Droplets on Superhydrophobic Surfaces, Macromolecules. 51 (2018) 7817–7827. https://doi.org/10.1021/acs.macromol.8b01589.

[140] J.W. Strutt, Lord Rayleigh, On the instability of jets, Proc. London Math. Soc. 10 (1878) 4–13.

[141] R. Rioboo, C. Tropea, M. Marengo, Outcomes from a drop impact on solid surfaces, At. Sprays. 11 (2001) 155–165.

[142] L. Xu, W.W. Zhang, S.R. Nagel, Drop splashing on a dry smooth surface, Phys. Rev. Lett. 94 (2005) 1–4. https://doi.org/10.1103/PhysRevLett.94.184505.

[143] L. Chen, Y. Wang, X. Peng, Q. Zhu, K. Zhang, Impact Dynamics of Aqueous Polymer Droplets on Superhydrophobic Surfaces, Macromolecules. 51 (2018) 7817–7827. https://doi.org/10.1021/acs.macromol.8b01589.

[144] P. Tourkine, M. Le Merrer, D. Quéré, Delayed freezing on water repellent materials, Langmuir. 25 (2009) 7214–7216. https://doi.org/10.1021/la900929u.

[145] A. Alizadeh, M. Yamada, R. Li, W. Shang, S. Otta, S. Zhong, L. Ge, A. Dhinojwala, K.R. Conway, V. Bahadur, A.J. Vinciquerra, B. Stephens, M.L. Blohm, Dynamics of ice nucleation on water repellent surfaces, Langmuir. 28 (2012) 3180–3186. https://doi.org/10.1021/la2045256.

[146] K.K. Varanasi, T. Deng, J.D. Smith, M. Hsu, N. Bhate, Frost formation and ice adhesion on superhydrophobic surfaces, Appl. Phys. Lett. 97 (2010). https://doi.org/10.1063/1.3524513.

[147] M. Zou, S. Beckford, R. Wei, C. Ellis, G. Hatton, M.A. Miller, Effects of surface roughness and energy on ice adhesion strength, Appl. Surf. Sci. 257 (2011) 3786–3792. https://doi.org/10.1016/j.apsusc.2010.11.149.

[148] T. Maitra, C. Antonini, M.K. Tiwari, A. Mularczyk, Z. Imeri, P. Schoch, D. Poulikakos, Supercooled water drops impacting superhydrophobic textures, Langmuir. 30 (2014) 10855–10861. https://doi.org/10.1021/la502675a.

[149] Z. Jin, H. Zhang, Z. Yang, The impact and freezing processes of a water droplet on a cold

surface with different inclined angles, Int. J. Heat Mass Transf. 103 (2016) 886–893. https://doi.org/10.1016/j.ijheatmasstransfer.2016.08.012.

[150] Y. Wang, J. Xue, Q. Wang, Q. Chen, J. Ding, Verification of Icephobic/Anti-icing Properties of a Superhydrophobic Surface, ACS Appl. Mater. Interfaces. 5 (2013) 3370–3381.

[151] J. Blake, D. Thompson, D. Raps, T. Strobl, Simulating the freezing of supercooled water droplets impacting a cooled substrate, AIAA J. 53 (2015) 1725–1739.

[152] S. Jung, M. Dorrestijn, D. Raps, A. Das, C.M. Megaridis, D. Poulikakos, Are superhydrophobic surfaces best for icephobicity?, Langmuir. 27 (2011) 3059–3066. https://doi.org/10.1021/la104762g.

[153] M. Tembely, A. Dolatabadi, A comprehensive model for predicting droplet freezing features on a cold substrate, J. Fluid Mech. 859 (2019) 566–585. https://doi.org/10.1017/jfm.2018.839.

[154] Y. Yao, C. Li, H. Zhang, R. Yang, Modelling the impact, spreading and freezing of a water droplet on horizontal and inclined superhydrophobic cooled surfaces, Appl. Surf. Sci. 419 (2017) 52–62. https://doi.org/10.1016/j.apsusc.2017.04.085.

[155] V. Bertola, K. Sefiane, Controlling secondary atomization during drop impact on hot surfaces by polymer additives, Phys. Fluids. 17 (2005) 108104. https://doi.org/10.1063/1.2112667.

[156] K. Carpenter, V. Bahadur, Saltwater icephobicity: Influence of surface chemistry on saltwater icing, Sci. Rep. 5 (2015) 1–11. https://doi.org/10.1038/srep17563.

[157] A.M. Emelyanenko, K.A. Emelyanenko, L.B. Boinovich, Deep Undercooling of Aqueous Droplets on a Superhydrophobic Surface: The Specific Role of Cation Hydration, J. Phys. Chem. Lett. 11 (2020) 3058–3062. https://doi.org/10.1021/acs.jpclett.0c00609.

[158] M. Song, J. Ju, S. Luo, Y. Han, Z. Dong, Y. Wang, Z. Gu, L. Zhang, R. Hao, L. Jiang, Controlling liquid splash on superhydrophobic surfaces by a vesicle surfactant, Sci. Adv. 3 (2017) 1–8. https://doi.org/10.1126/sciadv.1602188.

[159] S.S. Mohapatra, S. V. Ravikumar, A. Verma, S.K. Pal, S. Chakraborty, Experimental investigation of effect of a surfactant to increase cooling of hot steel plates by a water jet, J. Heat Transfer. 135 (2013) 1–7. https://doi.org/10.1115/1.4007878.

[160] A.R. Esmaeili, N. Mir, R. Mohammadi, Further Step toward a Comprehensive Understanding of the Effect of Surfactant Additions on Altering the Impact Dynamics of Water Droplets, Langmuir. 37 (2021). https://doi.org/10.1021/acs.langmuir.0c03192.

[161] P. Zhang, B. Peng, X. Yang, J. Wang, L. Jiang, Regulating Droplet Dynamic Wetting Behaviors Using Surfactant Additives on High-Temperature Surfaces, Adv. Mater. Interfaces. 7 (2020) 1–8. https://doi.org/10.1002/admi.202000501.

[162] H. Yin, Y. Feng, P. Li, J. Doutch, Y. Han, Y. Mei, Cryogenic viscoelastic surfactant fluids: Fabrication and application in a subzero environment, J. Colloid Interface Sci. 551 (2019) 89–100.

[163] N. Mir, C.E. Castano, J. V. Rojas, N. Norouzi, A.R. Esmaeili, R. Mohammadi, Self-separation of the adsorbent after recovery of rare-earth metals: Designing a novel non-wettable polymer, Sep. Purif. Technol. (2020) 118152. https://doi.org/10.1016/j.seppur.2020.118152.

[164] R. Mohammadi, J. Wassink, A. Amirfazli, Effect of surfactants on wetting of super-hydrophobic surfaces, Langmuir. 20 (2004) 9657–9662. https://doi.org/10.1021/la049268k.

[165] D.W. Fuerstenau, Equilibrium and nonequilibrium phenomena associated with the adsorption of ionic surfactants at solid–water interfaces, J. Colloid Interface Sci. 256 (2002) 79–90.

[166] V. Dutschk, K.G. Sabbatovskiy, M. Stolz, K. Grundke, V.M. Rudoy, Unusual wetting dynamics of aqueous surfactant solutions on polymer surfaces, J. Colloid Interface Sci. 267 (2003) 456–462. https://doi.org/10.1016/S0021-9797(03)00723-9.

[167] T. Maitra, M.K. Tiwari, C. Antonini, P. Schoch, S. Jung, P. Eberle, D. Poulikakos, On the nanoengineering of superhydrophobic and impalement resistant surface textures below the freezing temperature, Nano Lett. 14 (2014) 172–182.

[168] C. Clanet, C. Béguin, D. Richard, D. Quéré, Maximal deformation of an impacting drop, J. Fluid Mech. 517 (2004) 199–208. https://doi.org/10.1017/S0022112004000904.

[169] H. Li, Z. Cai, Y. Wang, Impact behaviors on superhydrophobic surfaces for water droplets of asymmetric double-chain quaternary ammonium surfactants, Langmuir. 36 (2020) 14113–14122. https://doi.org/10.1021/acs.langmuir.0c02783.

[170] B. Arminger, W. Gindl-Altmutter, J. Keckes, C. Hansmann, Facile preparation of superhydrophobic wood surfaces: Via spraying of aqueous alkyl ketene dimer dispersions, RSC Adv. 9 (2019) 24357–24367. https://doi.org/10.1039/c9ra03700d.

[171] X. Shao, F. Duan, Y. Hou, X. Zhong, Role of surfactant in controlling the deposition pattern of a particle-laden droplet: Fundamentals and strategies, Adv. Colloid Interface Sci. 275 (2020) 102049. https://doi.org/10.1016/j.cis.2019.102049.

[172] N. Shardt, M.B. Bigdeli, J.A.W. Elliott, P.A. Tsai, How Surfactants Affect Droplet Wetting on Hydrophobic Microstructures, J. Phys. Chem. Lett. 10 (2019) 7510–7515. https://doi.org/10.1021/acs.jpclett.9b02802.

[173] L. Boinovich, A.M. Emelyanenko, V. V. Korolev, A.S. Pashinin, Effect of wettability on sessile drop freezing: When superhydrophobicity stimulates an extreme freezing delay, Langmuir. 30 (2014) 1659–1668. https://doi.org/10.1021/la403796g.

[174] D.A. Knopf, Y.J. Rigg, Homogeneous ice nucleation from aqueous inorganic/organic particles representative of biomass burning: Water activity, freezing temperatures, nucleation rates, J. Phys. Chem. A. 115 (2011) 762–773. https://doi.org/10.1021/jp109171g.

[175] B. Zobrist, T. Koop, B.P. Luo, C. Marcolli, T. Peter, Heterogeneous ice nucleation rate coefficient of water droplets coated by a nonadecanol monolayer, J. Phys. Chem. C. 111

(2007) 2149–2155. https://doi.org/10.1021/jp066080w.

[176] A.R. Jones, J. Hamann, A.C. Lund, C.A. Schuh, Nanocrystalline Ni-W alloy coating for engineering applications, Plat. Surf. Finish. 97 (2010) 52.

[177] M. Lagarde, A. Billard, J. Creus, X. Feaugas, J.L. Grosseau-Poussard, S. Touzain, C. Savall, Electrochemical behavior of Ni–W alloys obtained by magnetron sputtering, Surf. Coatings Technol. 352 (2018) 581–590. https://doi.org/10.1016/j.surfcoat.2018.07.071.

[178] I. Valyukh, S. V. Green, C.G. Granqvist, G.A. Niklasson, S. Valyukh, H. Arwin, Optical properties of thin films of mixed Ni-W oxide made by reactive DC magnetron sputtering, Thin Solid Films. 519 (2011) 2914–2918. https://doi.org/10.1016/j.tsf.2010.11.089.

[179] D. Yin, C.J. Marvel, F.Y. Cui, R.P. Vinci, M.P. Harmer, Microstructure and fracture toughness of electrodeposited Ni-21 at.% W alloy thick films, Acta Mater. 143 (2018) 272–280. https://doi.org/10.1016/j.actamat.2017.10.001.

[180] A.L.M. Oliveira, J.D. Costa, M.B. de Sousa, J.J.N. Alves, A.R.N. Campos, R.A.C. Santana, S. Prasad, Studies on electrodeposition and characterization of the Ni–W–Fe alloys coatings, J. Alloys Compd. 619 (2015) 697–703.

[181] M.V.N. Vamsi, N.P. Wasekar, G. Sundararajan, Influence of heat treatment on microstructure and mechanical properties of pulse electrodeposited Ni-W alloy coatings, Surf. Coatings Technol. 319 (2017) 403–414. https://doi.org/10.1016/j.surfcoat.2017.03.074.

[182] P. Indyka, E. Beltowska-Lehman, L. Tarkowski, A. Bigos, E. Garcia-Lecina, Structure characterization of nanocrystalline Ni–W alloys obtained by electrodeposition, J. Alloys Compd. 590 (2014) 75–79.

[183] B. Li, W. Zhang, W. Zhang, Y. Huan, Preparation of Ni-W/SiC nanocomposite coatings by electrochemical deposition, J. Alloys Compd. 702 (2017) 38–50.

[184] C. Borgia, T. Scharowsky, A. Furrer, C. Solenthaler, R. Spolenak, A combinatorial study on the influence of elemental composition and heat treatment on the phase composition, microstructure and mechanical properties of Ni-W alloy thin films, Acta Mater. 59 (2011) 386–399. https://doi.org/10.1016/j.actamat.2010.09.045.

[185] T.J. Rupert, J.C. Trenkle, C.A. Schuh, Enhanced solid solution effects on the strength of nanocrystalline alloys, Acta Mater. 59 (2011) 1619–1631. https://doi.org/10.1016/j.actamat.2010.11.026.

[186] R.M.N. Pelloux, N.J. Grant, Solid Solution and Second-Phase Strengthening of Nickel Alloys at High and Low Temperatures, Trans. AIME. 218 (1960) 218–232.

[187] R. Labusch, A statistical theory of solid solution hardening, Phys. Status Solidi. 41 (1970) 659–669.

[188] E. Luber, R. Mohammadi, C. Ophus, Z. Lee, N. Nelson-Fitzpatrick, K. Westra, S. Evoy, U. Dahmen, V. Radmilovic, D. Mitlin, Tailoring the microstructure and surface morphology of metal thin films for nano-electro-mechanical systems applications, Nanotechnology. 19 (2008) 125705.

[189] J.H. Huang, C.H. Ma, H. Chen, Effect of Ti interlayer on the residual stress and texture development of TiN thin films deposited by unbalanced magnetron sputtering, Surf. Coatings Technol. 201 (2006) 3199–3204. https://doi.org/10.1016/j.surfcoat.2006.06.038.

[190] G. Bassiri, Diffusion effect of intermetallic layers on adhesion and mechanical properties of electrical contacts, Fundam. Nanotechnol. (2006) 1–10.

[191] S. Tulić, T. Waitz, O. Romanyuk, M. Varga, M. Čaplovičová, G. Habler, V. Vretenár, M. Kotlár, A. Kromka, B. Rezek, V. Skákalová, Ni-mediated reactions in nanocrystalline diamond on Si substrates: The role of the oxide barrier, RSC Adv. 10 (2020) 8224–8232. https://doi.org/10.1039/d0ra00809e.

[192] I.P. Ivanov, I. Sen, P. Keswick, Electrical conductivity of high aspect ratio trenches in chemical-vapor deposition W technology, J. Vac. Sci. Technol. B Microelectron. Nanom. Struct. Process. Meas. Phenom. 24 (2006) 523–533.

[193] C.Y. Lee, T.Y. Tseng, S.Y. Li, P. Lin, Growth of zinc oxide nanowires on silicon (100), Tamkang J. Sci. Eng. 6 (2003) 127–132.

[194] S. Gates-Rector, T. Blanton, The Powder Diffraction File: a quality materials characterization database, Powder Diffr. 34 (2019) 352–360.

[195] H. Wang, X. Kou, J. Zhang, J. Li, Large scale synthesis and characterization of Ni nanoparticles by solution reduction method, Bull. Mater. Sci. 31 (2008) 97–100.

[196] N.P. Wasekar, G. Sundararajan, Sliding wear behavior of electrodeposited Ni-W alloy and hard chrome coatings, Wear. 342–343 (2015) 340–348. https://doi.org/10.1016/j.wear.2015.10.003.

[197] T. Egami, Y. Waseda, Atomic size effect on the glass forming ability of metallic alloys, J. Non. Cryst. Solids. 64 (1984) 113–134.

[198] O. Younes, L. Zhu, Y. Rosenberg, Y. Shacham-Diamand, E. Gileadi, Electroplating of amorphous thin films of tungsten/nickel alloys, Langmuir. 17 (2001) 8270–8275. https://doi.org/10.1021/la010660x.

[199] A. Gabriel, C.H. Allibert, I. Ansara, H.L. Lukas, Experimental and calculated phase diagrams of the Ni-W, Co-W and Co-Ni-W system, Zeitschrift Für Met. 76 (1985) 589–595.

[200] S. Fritze, C.M. Koller, L. von Fieandt, P. Malinovskis, K. Johansson, E. Lewin, P.H. Mayrhofer, U. Jansson, Influence of deposition temperature on the phase evolution of HfNbTiVZr high-entropy thin films, Materials (Basel). 12 (2019) 10–17. https://doi.org/10.3390/ma12040587.

[201] J.T. Gudmundsson, Physics and technology of magnetron sputtering discharges, Plasma Sources Sci. Technol. 29 (2020). https://doi.org/10.1088/1361-6595/abb7bd.

[202] M. Ohring, Materials science of thin films, Elsevier, 2001.

[203] F. Liu, Precipitation of a metastable Fe (Ag) solid solution upon annealing of supersaturated Fe (Ag) thin film prepared by pulsed laser deposition, Appl. Phys. A. 81

(2005) 1095–1098.

[204] Z. Oksiuta, K. Perkowski, M. Osuchowski, M. Zalewska, M. Andrzejczuk, Microstructure and thermal properties of mechanically alloyed W-1 % TiC powder consolidated via two-step HIPping, Fusion Eng. Des. 126 (2018) 51–58. https://doi.org/10.1016/j.fusengdes.2017.11.010.

[205] F.T.N. Vüllers, R. Spolenak, Alpha- vs. beta-W nanocrystalline thin films: A comprehensive study of sputter parameters and resulting materials' properties, Thin Solid Films. 577 (2015) 26–34. https://doi.org/10.1016/j.tsf.2015.01.030.

[206] S. Gonderman, J.K. Tripathi, T.J. Novakowski, T. Sizyuk, A. Hassanein, Effect of dual ion beam irradiation (helium and deuterium) on tungsten – tantalum alloys under fusion relevant conditions, Nucl. Mater. Energy. 12 (2017) 346–352. https://doi.org/10.1016/j.nme.2017.02.011.

[207] C.A. Schuh, T.G. Nieh, H. Iwasaki, The effect of solid solution W additions on the mechanical properties of nanocrystalline Ni, Acta Mater. 51 (2003) 431–443. https://doi.org/10.1016/S1359-6454(02)00427-5.

[208] F. Ebrahimi, G.R. Bourne, M.S. Kelly, T.E. Matthews, Mechanical properties of nanocrystalline nickel produced by electrodeposition, Nanostructured Mater. 11 (1999) 343–350.

[209] Y. Mishima, S. Ochiai, N. Hamao, M. Yodogawa, T. Suzuki, Solid solution hardening of nickel—role of transition metal and B-subgroup solutes—, Trans. Japan Inst. Met. 27 (1986) 656–664. https://doi.org/10.2320/matertrans1960.27.656.

[210] T. Shinoda, K. Masuda-Jindo, Y. Mishima, T. Suzuki, Extra contribution of transition-metal solutes to the solid-solution hardening of nickel, Phys. Rev. B. 35 (1987) 2155–2161. https://doi.org/10.1103/PhysRevB.35.2155.

[211] H. ur Rehman, K. Durst, S. Neumeier, A. Sato, R. Reed, M. Göken, On the temperature dependent strengthening of nickel by transition metal solutes, Acta Mater. 137 (2017) 54–63.

[212] N.J. Petch, The cleavage strength of polycrystals, J. Iron Steel Inst. 174 (1953) 25–28.

[213] J.D. Eshelby, F.C. Frank, F.R.N. Nabarro, XLI. The equilibrium of linear arrays of dislocations., London, Edinburgh, Dublin Philos. Mag. J. Sci. 42 (1951) 351–364.

[214] M. Doms, H. Feindt, W.J. Kuipers, D. Shewtanasoontorn, A.S. Matar, S. Brinkhues, R.H. Welton, J. Mueller, Hydrophobic coatings for MEMS applications, J. Micromechanics Microengineering. 18 (2008). https://doi.org/10.1088/0960-1317/18/5/055030.

[215] A.R. Esmaeili, N. Mir, R. Mohammadi, Influence of W content on microstructure and surface morphology of hard Ni-W films fabricated by magnetron co-sputtering, J. Vac. Sci. Technol. A Vacuum, Surfaces, Film. 39 (2021) 33405.

[216] W. Fang, H. Mayama, K. Tsujii, Formation mechanism of super water-repellent fractal surfaces of alkylketene dimer, Colloids Surfaces A Physicochem. Eng. Asp. 316 (2008) 258–265. https://doi.org/10.1016/j.colsurfa.2007.09.010.

Appendix A: Supporting Information

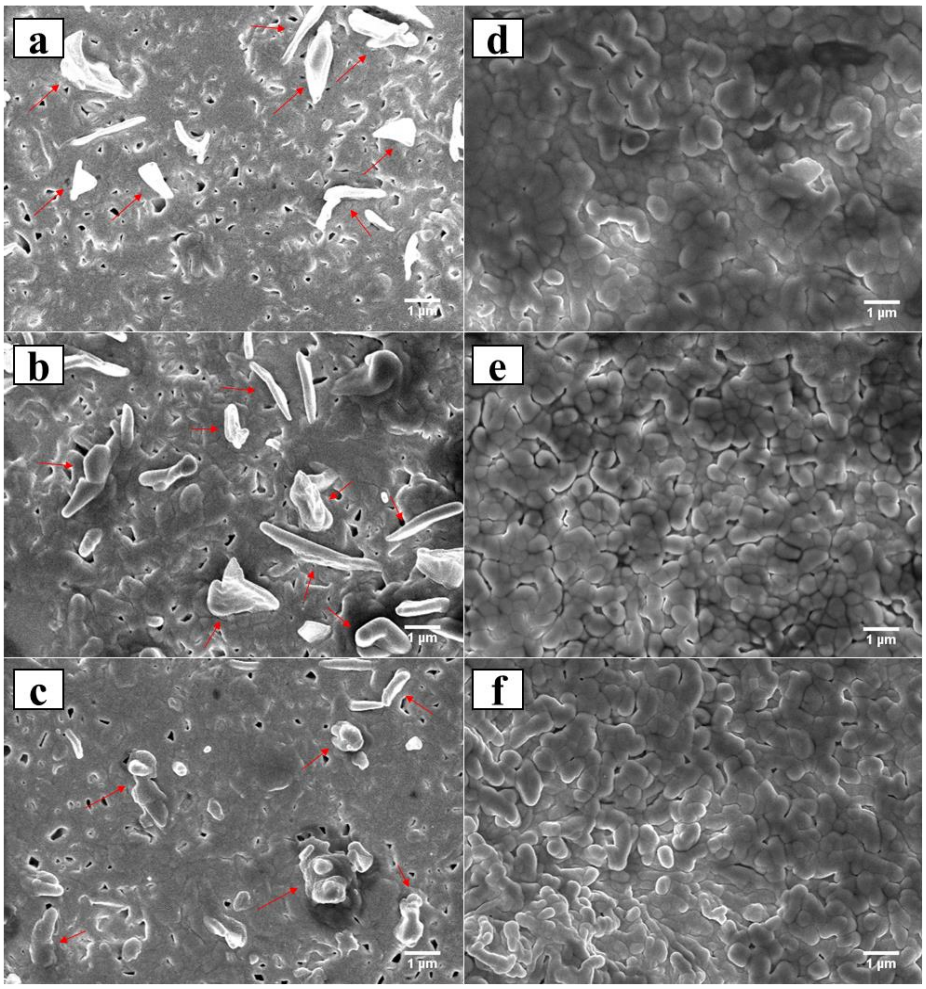

Figure A1. SEM images of AKD coatings prepared from a melt isothermally held at different times at 40°C, and undergone different post-synthesis modifications: (a) isotherm time was 3 min without any post-solidification treatments, (b) isotherm time was 3 h without any post-solidification treatments, (c) isotherm time was 6 h without any post-solidification treatments, (d) isotherm time was 3 min and the solid coating was treated with ethanol, (e) isotherm time was 3 h and the solid coating was treated with ethanol, and (f) isotherm time was 6 h and the solid coating was treated with ethanol. Red arrows show particles with irregular random morphologies on the solid coatings with no post treatment.

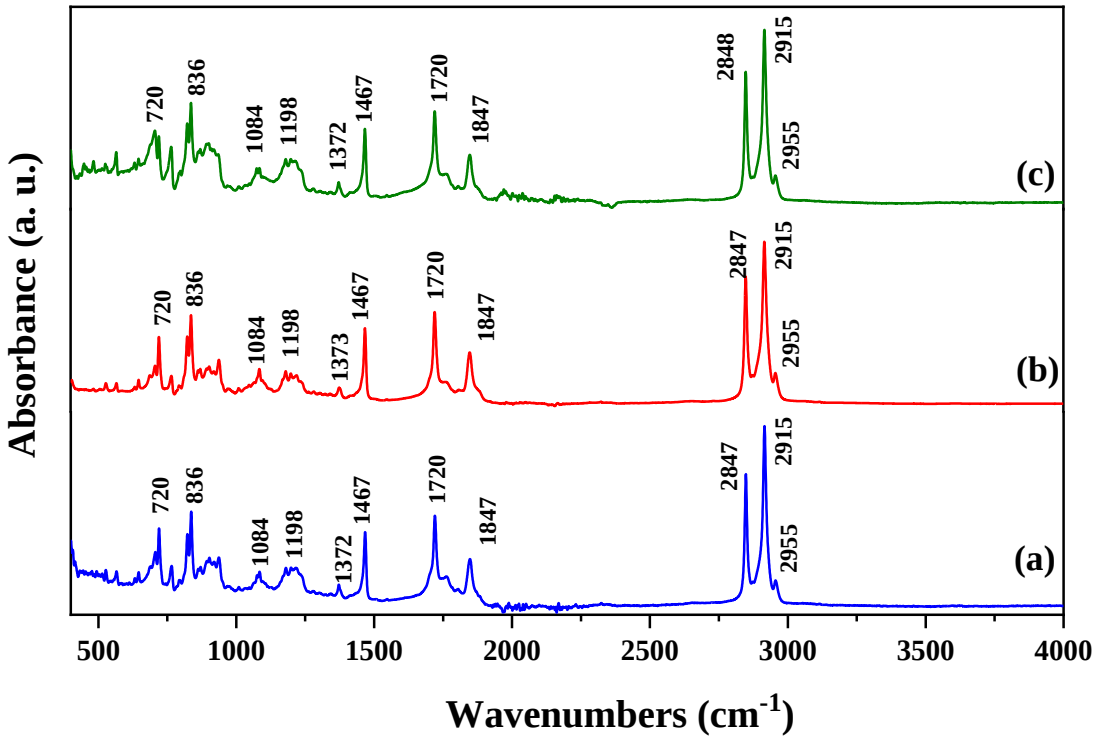

Figure A2. FT-IR spectra of solidified AKD from the isothermally heated melt at 70°C for 3min (a) as-solidified, (b) solid coating was treated with ethanol, and (c) the as-solidified sample cured over time with no extra modifications.

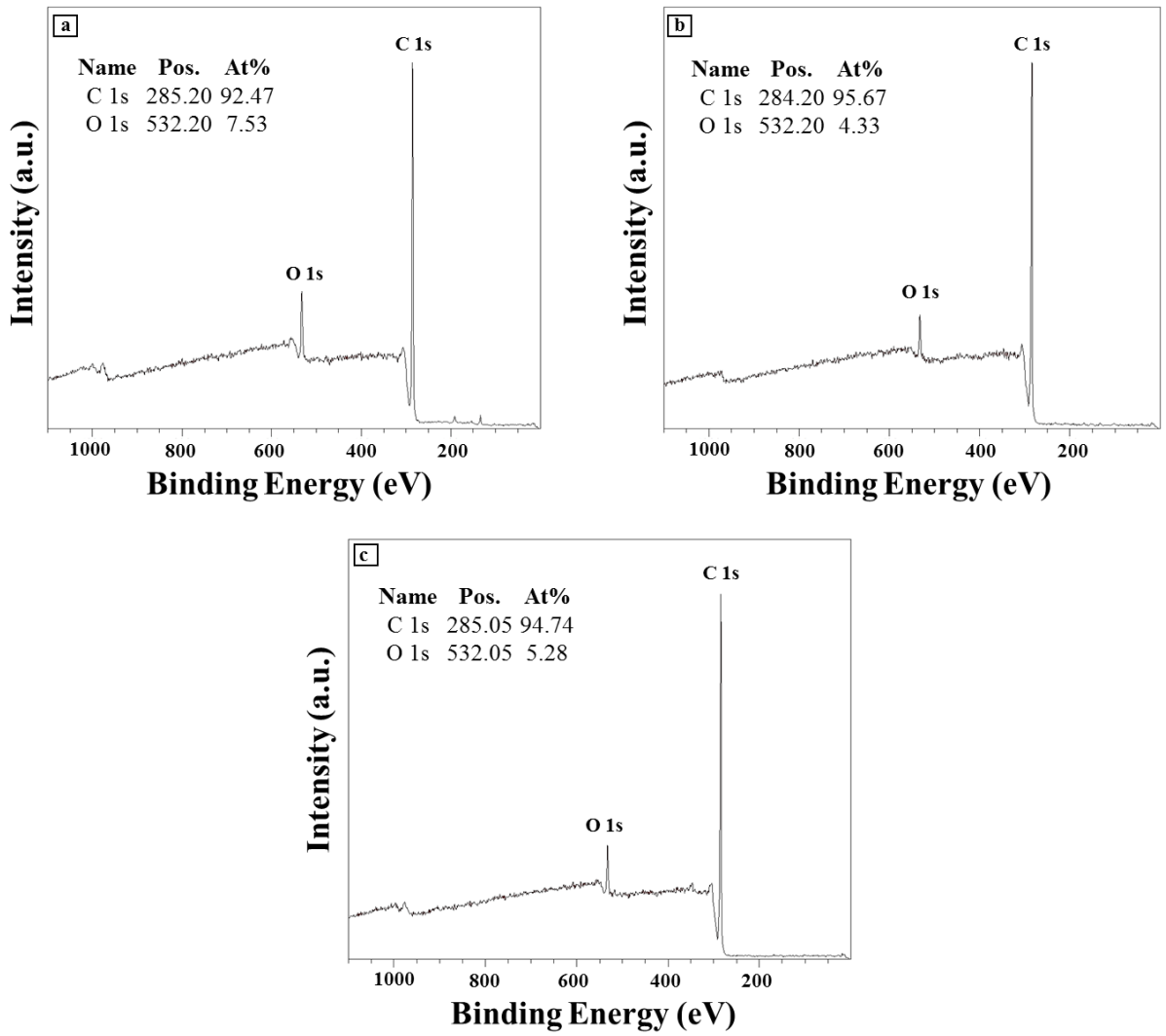

Figure A3. XPS scan surveys of AKD coating from the isothermally heated melt at 70°C for 3 min (a) as-solidified, (b) solid coating was treated with ethanol, and (c) the as-solidified sample cured over time with no extra modifications.

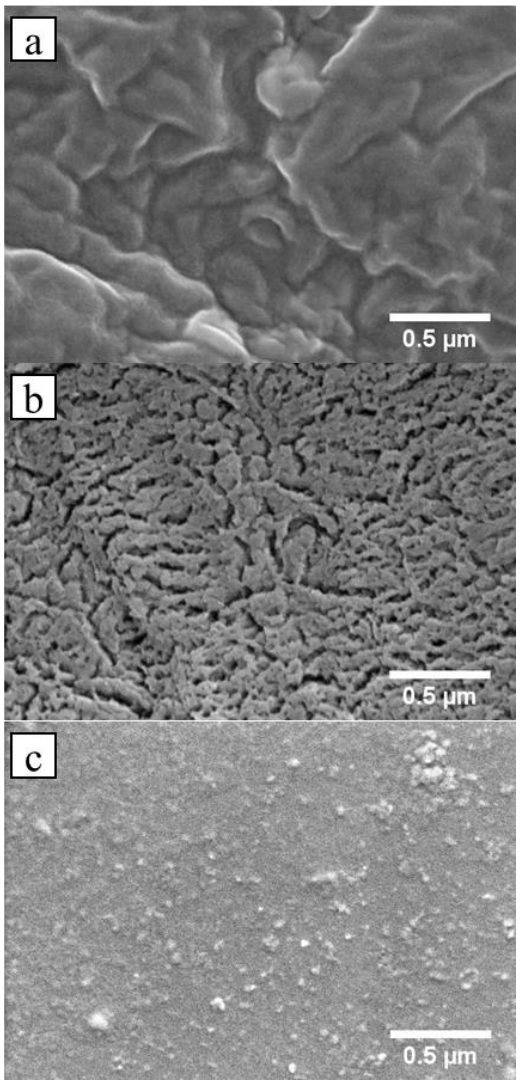

Figure A4. Scanning electron microscopy (SEM) images of the impact substrate: (a) AKD, (b) PTFE and (c) Glass. All the substrates were coated with a thin layer (~2 nm) of platinum prior to imaging for better electrical conductivity.

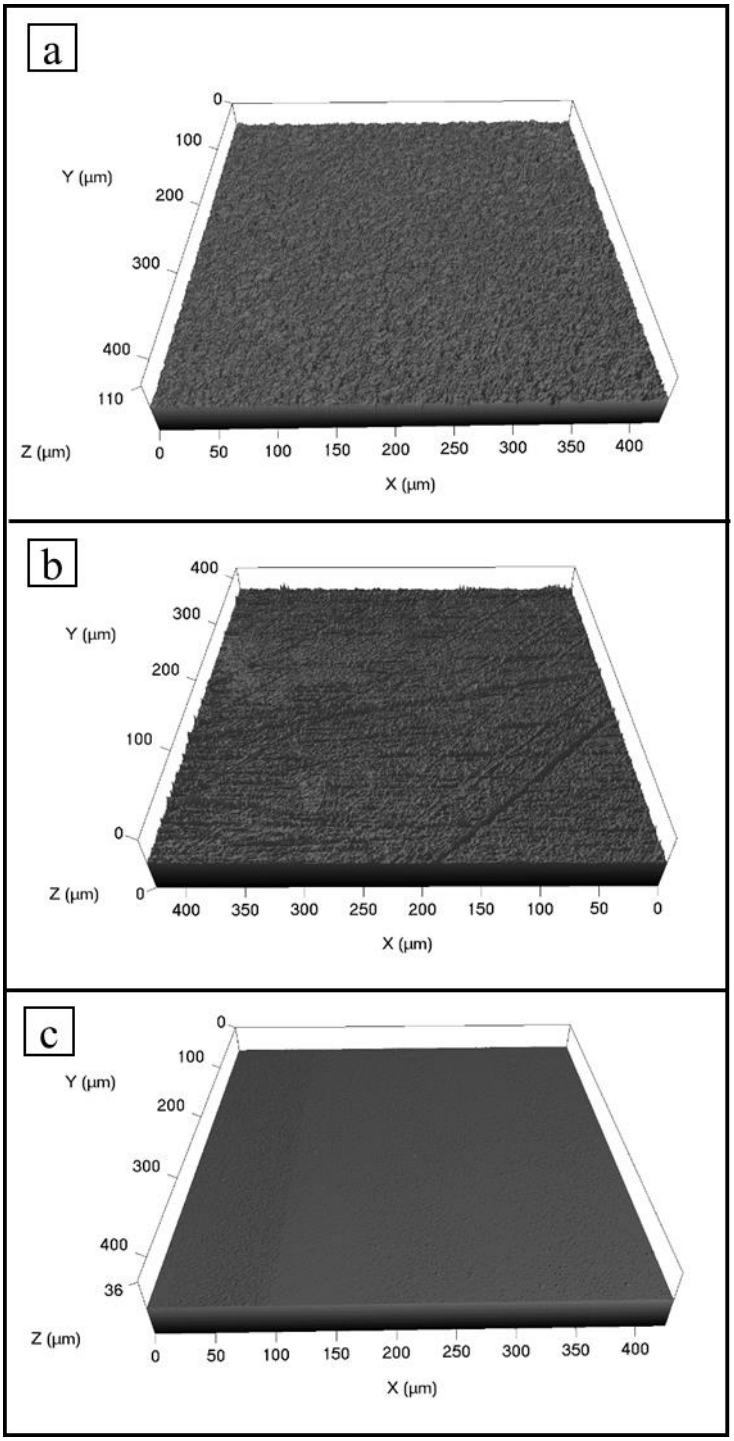

Figure A5. Surface topography of the impact substrates obtained using laser scanning confocal microscopy: (a) AKD, (b) PTFE and (c) Glass.

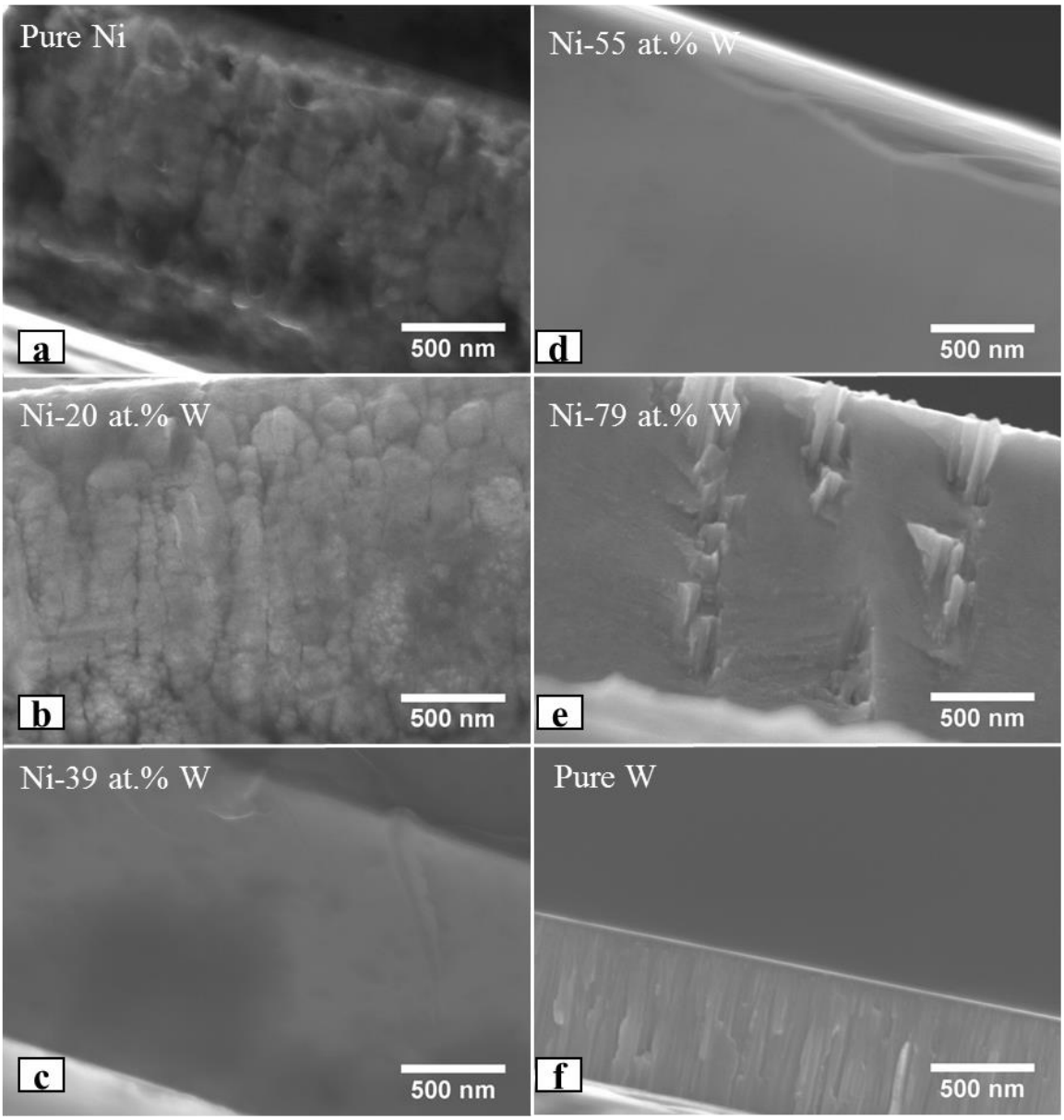

Figure A6. Cross-sectional scanning electron microscopy (SEM) images of the co-sputtered Ni-W thin films with respect to their W content: (a) pure Ni, (b-e) Ni-W coating with 20, 39, 55, and 79 at.% W, respectively, and (f) pure W.

Table A1. Comparison of the method, operation parameters, chemicals used, contact angle, and hysteresis of the present study with those of the literature

Summary of method	Reaction time (h)	Treating temperature (°C)	Equipment	Chemicals used	Contact angle (°)	Hysteresis/ Sliding angle (°)	Ref.
Dissolving the AKD powder in supercritical CO_2 at 100-300 bar	1	40, 60 and 65	Rapid Expansion of Supercritical Solutions (RESS) apparatus	Liquid nitrogen, Liquid carbon dioxide	110-160[a]	20-50	[77]
					152-173[b]	-	[76]
Co-condensation of TEOS with a fluorinated alkyl silane (FAS)	> 12	110	-	Ammonium hydroxide, Methyltriethoxysilane, Phenyl triethoxysilan, Tetraethylorthosilicate (TEOS)	140-175[b]	2-40	[63]
Chemical vapor deposition (CVD) of POTS on silica-coated paper	5	125-150	Sealed vessel and oven	1H,1H,2H,2H-perfluorooctyltriethoxysilan (POTS), TEOS	155[b]	< 5	[65]
Solid AKD Heat-treatment	1	50	Oven	None	155-160[b]	-	[216]
Ethanol treatment of the AKD solid coating	0.05	40	Hot plate	Ethanol	156-158[b]	2	Present Study
	6	70			162-163[a]	1	

[a] Dynamic contact angle

[b] Static contact angle

Table A2. The impact of treating the solid coatings, obtained from the isothermally heated melt at 70°C for 3 min, with different organic solvents on advancing and receding contact angles

Solvent	Ethanol	Methanol	Isopropanol
Advancing contact angle (°)	160.5±1.1	159.4±1.7	161.9±1.2
Receding contact angle (°)	158.5±1.5	158.2±1.7	160.5±1.3

Table A3. The relation between the maximum spreading factor of SDS-laden droplets and Weber number on the hydrophilic glass, hydrophobic PTFE and superhydrophobic AKD

		Maximum Spreading Factor		
Surfactant	Weber Number	Glass	PTFE	AKD
2 mM SDS	5.75	1.78	1.61	1.28
	29.48	2.53	2.33	2.08
	71.90	3.08	3.03	2.84
	133.02	3.58	3.35	3.90
	211.40	3.85	4.19	4.71
4 mM SDS	7.11	1.65	1.50	1.31
	36.46	2.77	2.48	2.18
	88.92	3.64	3.13	2.78
	164.49	3.61	3.62	3.61
	261.41	3.89	3.83	4.36
8 mM SDS	9.42	2.09	1.65	1.46
	48.27	3.06	2.73	2.34
	117.73	3.34	3.33	3.01
	217.79	3.86	3.74	3.83
	346.11	4.21	4.08	4.33
16 mM SDS	9.21	1.81	1.58	1.40
	47.22	2.94	2.81	2.32
	115.18	3.55	3.38	3.36
	213.07	3.99	3.76	3.80
	338.61	4.24	3.91	3.86

Table A4. The relation between the maximum spreading factor of CTAB-laden droplets and Weber number on the hydrophilic glass, hydrophobic PTFE and superhydrophobic AKD

		Maximum Spreading Factor		
Surfactant	Weber Number	Glass	PTFE	AKD
0.2 mM CTAB	5.87	1.84	1.61	1.47
	30.09	2.40	2.31	2.08
	73.39	3.09	2.99	3.05
	135.77	3.77	3.62	3.78
	215.77	4.03	3.96	4.25
0.45 mM CTAB	6.81	1.64	1.66	1.50
	34.89	2.45	2.34	2.12
	85.11	3.06	2.87	2.75
	157.45	3.50	3.45	3.57
	250.22	4.18	4.01	4.51
0.9 mM CTAB	8.67	1.60	1.46	1.32
	44.43	2.67	2.50	2.25
	108.37	3.08	3.08	2.99
	200.48	3.60	3.58	3.66
	318.61	4.00	3.93	3.65
1.8 mM CTAB	9.03	1.65	1.57	1.36
	46.27	2.53	2.43	2.12
	112.86	3.23	3.16	2.87
	208.79	3.67	3.57	4.03
	331.81	4.07	3.82	3.88

Table A5. The relation between the maximum spreading factor of MEGA 10-laden droplets and Weber number on the hydrophilic glass, hydrophobic PTFE and superhydrophobic AKD

		Maximum Spreading Factor		
Surfactant	Weber Number	Glass	PTFE	AKD
0.5 mM MEGA-10	5.67	1.78	1.62	1.44
	29.04	2.33	2.36	1.95
	70.83	2.96	2.84	2.79
	131.04	3.42	3.38	3.79
	208.25	3.73	3.82	3.78
2 mM MEGA-10	7.30	1.80	1.68	1.39
	37.42	2.34	2.29	1.98
	91.27	3.05	2.73	2.64
	168.84	3.37	3.27	3.47
	268.32	3.69	3.87	3.61
7 mM MEGA-10	9.30	1.89	1.60	1.54
	47.66	2.71	2.46	2.20
	116.24	3.25	3.08	3.07
	215.05	3.64	3.46	3.43
	341.76	3.85	3.76	3.49
14 mM MEGA-10	9.61	1.85	1.64	1.42
	49.25	2.68	2.61	2.24
	120.12	3.09	3.08	2.74
	222.21	3.77	3.49	3.30
	353.14	3.89	3.76	3.44

Appendix B: Vita

Amir R. Esmaeili

Richmond, VA, USA; Email: amir.esmaeili93@gmail.com; Phone: +1 (804)-402-4627
https://www.linkedin.com/in/amir-esmaeili-628ba984/

Summary:
A self-motivated, innovative and versatile engineer doing his Ph.D. in mechanical engineering. Demonstrated strong analytical and problem-solving skills over 2+ years of working at Advanced Functional Materials Laboratory.

- Experienced with various surface characterization techniques including SEM, EDS, XRD, AFM, XPS, FTIR and CLSM.
- 2+ years of research experience in design and fabrication of advanced functional coatings.
- CAD/Simulation ANSYS Workbench, AutoCAD, Solidworks, Matlab.
- Published 7 papers in high-quality peer-reviewed journals.

EDUCATION

- **PhD, Mechanical Engineering (GPA 4.0/4.0)** (2019–2021)
  Virginia Commonwealth University, Richmond, VA
- **MS, Mechanical Engineering (GPA 3.8/4.0)** (2015–2018)
  University of Tehran, Tehran
- **BS, Mechanical Engineering (GPA 3.7/4.0)** (2011–2015)
  K.N. Toosi University of Technology, Tehran

PROFESSIONAL EXPERIENCE AND ACCOMPLISHMENTS

Graduate Research Assistant, Advanced Functional Materials Laboratory
Virginia Commonwealth University, Richmond VA (Jan. 2019–Aug. 2021)

- Developed a facile and fast method to decrease the curing time of alkyl ketene dimer from 6 days to only 10 min.
- Manufactured a nickel-tungsten thin film with a high hardness of ~ 22 GPa (20% higher than previous studies).
- Controlled and manipulated the impact dynamics of water droplets by addition of various surfactants.
- Developed a novel experimental setup to study droplet impact at freezing temperatures.
- Conducted high-speed imaging to investigate heat transfer of aqueous droplets on non-wettable materials.
- Mentored a group of 5 students on a research project aimed at investigating the effects of surfactants on the water droplets dynamic behavior.
- Experienced in technical writing and preparing professional presentations.
- Published 7 manuscripts in peer-reviewed journals and delivered several presentations.

Graduate Teaching Assistant
Virginia Commonwealth University, Richmond VA (Jan. 2019–Aug. 2021)

- Helped students with their problems/projects in Material Science for Engineers, and Dynamic and Kinematics.

Research/Teaching Assistant

University of Tehran, Tehran (Aug. 2015–Apr. 2018)

- Performed CFD simulation of the deposition and dispersion patterns of fibrous particles in the human nasal cavity using Ansys Fluent and CFX.
- Gave lectures and helped students with Numerical Methods, Fluid Mechanics and Thermodynamics.

Intern

Samandis Co, Tehran (May 2015–Jul. 2015)

- Designed the HVAC systems of an office building using Carrier HAP.

TECHNICAL SKILLS

Experimental Skills: SEM, EDS, XRD (Powder X-ray Diffraction), AFM, XPS, FTIR, PVD, CVD, Confocal microscopy, Optical microscopy, Magnetron Sputtering, High-speed imaging, Microhardness testing.

Modeling Skills: Fluent in computer programming with MATLAB. Comfortable with engineering packages such as ANSYS Fluent and CFX. Experienced in ImageJ image processing tools, AutoCAD, and Solidworks.

Verbal and Non-verbal Communication Skills: Demonstrated by several technical presentations and scientific publications.

- Surface Characterization
- Non-Wettable Polymers
- Metallic alloys
- Advanced Functional Coating
- Droplet impact
- Thermal and Fluid Science Research
- Material Science
- Design of Experiments
- Hands-on Experiences
- Image processing
- Statistical Analysis
- Numerical Modeling in Engineering
- Computational Fluid Dynamics (CFD)
- CAD Modelling
- Project Management
- Teamwork

PEER-REVIEWED PUBLICATIONS

- **Esmaeili, A. R.**, Mir, N., & Mohammadi, R. (2021). Influence of W content on microstructure and surface morphology of hard Ni-W films fabricated by magnetron co-sputtering. *Journal of Vacuum Science & Technology A: Vacuum, Surfaces, and Films, 39(3), 033405. https://doi.org/10.1116/6.0000915*

- **Esmaeili, A. R.**, Mir, N., and Mohammadi, R. (2021). Further Step toward a Comprehensive Understanding of the Effect of Surfactant Additions on Altering the Impact Dynamics of Water Droplets. *Langmuir 2021 37 (2), 841-851*. *DOI: 10.1021/acs.langmuir.0c03192r.*
- Mir, N., Castano, C. E., Rojas, J. V., Norouzi, N., **Esmaeili, A. R.**, & Mohammadi, R. (2021). Self-separation of the adsorbent after recovery of rare-earth metals: Designing a novel non-wettable polymer. *Separation and Purification Technology*, *259*, *118152.*
- Manniello, M. D., Hosseini, S., Alfaifi, A., **Esmaeili, A. R.**, Kolanjiyil, A. V., Walenga, R., ... & Golshahi, L. (2021). In vitro evaluation of regional nasal drug delivery using multiple anatomical nasal replicas of adult human subjects and two nasal sprays. *International Journal of Pharmaceutics*, *593*, *120103.*
- **Esmaeili, A. R.**, Mir, N., & Mohammadi, R. (2020). A facile, fast, and low-cost method for fabrication of micro/nano-textured superhydrophobic surfaces. *Journal of colloid and interface science*, *573*, *317-327.*
- **Esmaeili, A. R.**, Sajadi, B., and Akbarzadeh, M. (2020). Numerical simulation of ellipsoidal particles deposition in the human nasal cavity under cyclic inspiratory flow. *Journal of the Brazilian Society of Mechanical Sciences and Engineering*, 42(243), 243.
- **Esmaeili, A. R.**, Keshavarz, M., and Mojra, A. (2015). Optimization of hyperelastic model parameters of soft tissue based on genetic algorithm utilizing experimental mechanical dataset. *Modares Mechanical Engineering, 15(9), 134-140.*